

AFRL-VS-HA-TR-98-0006

**MINIATURIZED OPTICAL FIBER MAGNETIC
FIELD SENSORS FOR ON-BOARD
ENVIRONMENTAL DIAGNOSTICS**

**Anbo Wang
Richard O. Claus**

**Virginia Polytechnic Institute & State University
Bradley Department of Electrical Engineering
Fiber & Electro-Optics Research Center
Blacksburg, VA 24061**

30 December 1997

19980514 157

**Final Report
15 August 1995-30 December 1997**

approved for public release, distribution unlimited

DTIC QUALITY INSPECTED 4

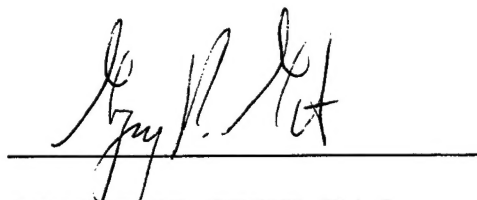


**AIR FORCE RESEARCH LABORATORY
Space Vehicles Directorate
29 Randolph Road
AIR FORCE MATERIEL COMMAND
HANSCOMB AFB, MA 01731-3010**

"This technical report has been reviewed and is approved for publication"



CHRISTOPHER P. CHAPLIN, Capt, USAF
Contract Manager



GREGORY P. GINET, Chief
Space Hazards Branch

This report has been reviewed by the ESC Public Affairs Office (PA) and is releasable to the National Technical Information Service (NTIS).

Qualified requestors may obtain additional copies from the Defense Technical Information Center (DTIC). All others should apply to the National Technical Information Service (NTIS).

If your address has changed, if you wish to be removed from the mailing list, or if the addressee is no longer employed by your organization, please notify AFRL/VSOS-IM, 29 Randolph Road, Hanscom AFB, MA 01731-3000. This will assist us in maintaining a current mailing list.

Do not return copies of this report unless contractual obligations or notices on a specific document require that it be returned.

REPORT DOCUMENTATION PAGE			Form Approved OMB No. 0704-0188	
Public reporting burden for this collection of information is estimated to average 1 hour per response, including the time for reviewing instructions, searching existing data sources, gathering and maintaining the data needed, and completing and reviewing the collection of information. Send comments regarding this burden estimate or any other aspect of this collection of information, including suggestions for reducing this burden, to Washington Headquarters Services, Directorate for Information Operations and Reports, 1215 Jefferson Davis Highway, Suite 1204, Arlington, VA 22202-4302, and to the Office of Management and Budget, Paperwork Reduction Project (0704-0188), Washington, DC 20503.				
1. AGENCY USE ONLY (Leave blank)		2. REPORT DATE 30 December 97		3. REPORT TYPE AND DATES COVERED Final (15 August 1995-30 December 1997)
4. TITLE AND SUBTITLE Miniaturized Optical Fiber Magnetic Field Sensors for On-Board Environmental Diagnostics			5. FUNDING NUMBERS PE 63410F PR 2822 TA GC WU VP	
6. AUTHOR(S) Anbo Wang Richard O. Claus			Contract F19628-95-C-0202	
7. PERFORMING ORGANIZATION NAME(S) AND ADDRESS(ES) Virginia Polytechnic Institute and State University Bradley Department of Electrical Engineering Fiber & Electro-Optics Research Center Blacksburg, VA 24061			8. PERFORMING ORGANIZATION REPORT NUMBER	
9. SPONSORING / MONITORING AGENCY NAME(S) AND ADDRESS(ES) Air Force Research Laboratory 29 Randolph Road Hanscom AFB, MA 01731-3010 Contract Manager: Lt. Chris Chaplin/VSBS			10. SPONSORING / MONITORING AGENCY REPORT NUMBER AFRL-VS-HA-TR-98-0006	
11. SUPPLEMENTARY NOTES				
12a. DISTRIBUTION / AVAILABILITY STATEMENT Approved for public release, distribution unlimited			12b. DISTRIBUTION CODE	
13. ABSTRACT (Maximum 200 words) A miniaturized optical fiber based sensor system has been developed for the measurement of vector magnetic fields. The operation of the sensor system is based on the detection of magnetostrictive dimensional changes in the sensor gage using a modified extrinsic Fabry-Perot Interferometer configuration. Because of the magnetostrictive reflector the gap length of the Fabry-Perot cavity formed by the two fiber ends depends on the magnetic fields applied to the sensor. Since the diameter of the magnetostrictive sensor gage is the same as that of the input/output fiber, the sensor is simply constructed by inserting the sensor gage and the input/output fiber into a small glass tube. The glass tube serves as both an aligner for the sensor gage and input/out fiber, and a passive temperature compensator. This sensor design shows 98% suppression of the thermally induced sensor output changes. A 5-times increase in sensor sensitivity is obtained with the transverse field annealing and the use of a new magnetostrictive material. A modified sensor gage endface demonstrates 92% of fringe visibility, which further improves the performance of the interferometer. The system has been shown to have a resolution better than 100 nT over a measurement range from 100 to 40,000 nT.				
14. SUBJECT TERMS optical fiber sensors, magnetic fields, extrinsic Fabry-Perot interferometers, temperature compensation, Metglas			15. NUMBER OF PAGES 154	
			16. PRICE CODE	
17. SECURITY CLASSIFICATION OF REPORT Unclassified	18. SECURITY CLASSIFICATION OF THIS PAGE Unclassified	19. SECURITY CLASSIFICATION OF ABSTRACT Unclassified	20. LIMITATION OF ABSTRACT SAR	

Contents

Summary	1
Chapter 1: Extrinsic Fabry-Perot Interferometer in Measuring Magnetic Field	4
1.1 Principle of the Sensor Operation	4
1.2 Magnetostriction of Ferromagnetic Materials	6
1.2.1 Magnetic Properties of Rare Earth-iron Compounds	6
1.2.2 Magnetic Properties of Metallic Glasses	7
1.3 Sensor Material Considerations	8
1.3.1 Survey of Candidate Magnetostrictive Materials	8
1.3.2 Experimental Investigation of Magnetostrictive Materials	8
1.4 Design of EFPI-based Optical Fiber Magnetic Field Sensors	12
1.4.1 Basic Sensor Design	12
1.4.2 Design of Field Annealing System	14
1.4.2 Novel Sensor Design	19
1.4.3 Enhancement of Performance of Transverse Field Annealed Metglas Wire	21
1.5 Signal Demodulation	23
1.5.1 Introduction to Signal Demodulation	23
1.5.2 Principles of Quadrature Signal Demodulation	23
1.5.3 Circuit Design for Quadrature Signal Demodulation	26
1.5.4 Evaluation of Quadrature Signal Demodulation Circuit	28
Chapter 2: Enhancing the Sensor Performance	35
2.1 High Field Transverse Annealing System	35
2.2 Determination of CTEs of Sensor Materials	36
2.2.1 Heat Capacity of Sensor Materials	36
2.2.2 Parameter Extraction Model	38
2.3 Designing Passive Temperature Stabilized Sensors	41
2.3.1 Evaluation of Passive Temperature Compensation Scheme	41
2.3.2 Two Magnetostriction Materials and One Compensator with NO Substrate Support	42
2.3.3 Quadrature Phase Shifted Sensor with One Magnetostrictive Element and Compensator	45

2.4 Modified EFPI Sensors	46
2.4.1 Sensor Design with Side-Wall Support	46
2.4.2 Vibration Insensitive Sensor Geometry	49
2.4.3 Adjustable Sensor Geometry	52
2.5 System Performance Analysis	58
2.5.1 Evaluation of Temperature Compensation Scheme	60
2.5.2 Calculation of Exact CTEs of Metglas wire and Compensator Tube	61
2.5.3 Signal Demodulation Circuitry	65
2.5.4 Factors Limiting System Performance	67
2.5.5 Improving System Performance	70
Chapter 3: Design of High Sensitivity Magnetic Field Sensors	72
3.1 Designing Passive Temperature Compensated Sensor	72
3.2 Enhancing the Sensor Gage Sensitivity	74
3.3 Mathematical Adjustment for Temperature Compensation	76
3.4 Improvement of Fringe Visibility	82
3.5 Optimal Biasing and Packaging Methods	84
3.5.1 Biasing the Sensor	84
3.5.2 Packaging the sensor	86
3.6 Low Magnetic Field Detectability	88
Chapter 4: Design of Three Dimensional Vector Field Measuring System	90
4.1 Three Dimensional Vector Field Representation	90
4.2 Design of Vector Field Measurement System	93
4.2.1 Sensor Head Design	93
4.2.2 System Design with Three Separate Laser Sources	94
4.2.3 System Design with Single Laser Source	94
4.3 Electronic Signal Processing	96
4.3.1 Opto-electronic Interface	97
4.3.2 Quadrature Phase Shifted EFPI Signal Demodulation Scheme	99
4.3.3 Analog Implementation	101
4.3.4 Microprocessor-based Signal Demodulation	103
4.4 Fabricated Magnetometer System	105

Chapter 5: System Calibration	107
5.1 Experimental Setup	107
5.2 Calibration Procedure	109
5.3 Experimental Results	110
Chapter 6: Conclusion	126
References	130
Appendix	131

SUMMARY

Objectives: The major objective of this program was to design, fabricate and implement optical fiber-based magnetometers for performing on-board environmental diagnostics, as part of an integrated SOBEDS package. Such an instrument is required by the Air Force and the DoD to be easily incorporated as a standard instrument complement or as a monitoring system on operational and scientific satellites. The approach followed at the Fiber & Electro-Optics Research Center (FEORC) of Virginia Tech for the fabrication of the proposed magnetometers is the modification of conventional extrinsic Fabry-Perot Interferometric (EFPI) - based sensors, with the incorporation of magnetostrictive transducer materials on the sensor elements. Although the specific near-term technical objective of the program was the implementation and evaluation of optical fiber-based magnetometers, the design and test results obtained are part of a larger vision of alternative methods for the characterization of magnetic fields.

This R&D Final Report details the accomplishments over the two year duration of the project (August 15, 1995 to December 30, 1997).

Project Progress: The major accomplishments during this project duration are summarized below;

- Various magnetostrictive materials were surveyed for selection of optimum transducer material and geometry.
- Extrinsic Fabry-Perot Interferometer (EFPI)-based and Split-Spectrum Intensity Based (SSIB) optical fiber sensors were studied for use in the magnetometer system.
- Candidate magnetostrictive materials were theoretically and experimentally evaluated.
- Various schemes of Metglas-bonded EFPI sensors were experimentally evaluated and characterized under different magnetic field intensities and frequencies.
- Temperature and other noise factor compensation concepts were tested for the sensor design.
- Investigation of appropriate signal demodulation schemes was conducted for the sensor system design.

- A novel EFPI-based configuration was designed and implemented using the magnetostrictive Metglas material as reflector in the Fabry-Perot cavity.
- A transverse field annealing system was successfully fabricated for increasing the sensitivity of the magnetostrictive material
- The Quadrature-Phase-Shift (QPS) signal demodulation scheme was finalized for the signal demodulation system.
- A robust passive temperature compensation technique was designed, implemented and tested for the new sensor geometry.
- Extensive evaluation of the sensors and the opto-electronics was conducted to enhance the system stability.
- A one-dimensional magnetic field measuring system was fabricated, with sensitivity, down to 700 nT, and demonstrated at the PDR meeting on 12th August 1996, at Hanscom AFB, Boston.
- System sensitivity was enhanced by increasing the sensor gage length.
- New sensor material with sensitivity five times that of the old one, was obtained.
- A scheme for increasing the fringe visibility of the sensor output was developed and implemented.
- Compact sensor packaging was achieved by using smaller permanent magnets for the DC magnetic bias.
- Accurate mathematical method for fabricating passively temperature compensated sensors was developed, tested and implemented.
- A vector magnetic field measuring system was designed.
- Microprocessor based signal demodulation scheme and instrumentation was developed.
- Complete system design, including sensor head, signal demodulation scheme and laser driver configuration, was finalized and presented at the CDR meeting on 9th April 1997, at FEORC, Blacksburg, Virginia.
- Fabrication and testing of the complete vector magnetic field measuring system as a single unit was completed.
- Operation manuals and other related documents for the entire system were prepared.

Technical Difficulites: There were several difficulties in fabrication of the vector magnetic field measuring system. The cut length accuracy of Metglas sensor gage and compenastor tube is limited by human eyes and ruler resolutions. Since one of the ends of the sensor is fixed by an epoxy, the spreading of epoxy inside of the compensator tube is hardly controlled with good accuracy. Since this system is an open-loop system which has no feedback to control except a passive temperature compensation, it is difficult to stabilize the sensor system for various noises. In summary, the open-loop system designed and fabricated for DC magnetic field measurement shows a fundamental limitation by law of physics and manufacturing difficulties in school lab environment. One effective way to overcome these problems would be to utilize hybrid active/passive temperature compensation and signal demodulation scheme described in the last quarterly reports. This method basically uses the active feedback and the nonlinearity of Metgals wire in very low magnetic field bias. Without elaborated supporting electronics, this method uses small coils, integrator and AC signal source to measure DC magnetic field. The following chapters of the report describe the research undertaken in each of the technical areas outlined above.

Chapter 1: Extrinsic Fabry-Perot Interferometer in Measuring Magnetic Field

1.1 Principle of the Sensor Operation

Optical fiber based Fabry-Perot (F-P) sensors have been shown to be highly sensitive to temperature, strain, vibration, acoustic waves, and magnetic fields. The Fabry-Perot cavity fabrication in these sensors has been typically achieved with the use of air-glass reflectors in fiber, Bragg gratings, or semi reflective splices at various locations along the fiber. The F-P sensors based on air-glass reflectors are referred to as the extrinsic F-P interferometers (EFPI). Because of its ease of construction, low fabrication cost, high reliability, and high resolution, this sensor has been shown to be attractive for many applications. As compared to the intrinsic Fabry-Perot interferometer, the other advantages of the extrinsic method over the intrinsic method include the avoidance of polarization problems, and the detection of only axial components. A typical EFPI sensor configuration is shown in Figure 1. The light from a laser source propagates along a lead-in single mode fiber to the Fabry-Perot cavity that is formed by the input/output and the target fibers. A fraction of this incident light, approximately 4 %, is reflected at the output endface of the input/output fiber back into the fiber. The light transmitted out of the input/output fiber projects onto the fiber endface of the target fiber. The reflected light from the target fiber is partially recoupled into the input/output fiber. The interference between the two reflections produces interfering fringes as the air-gap is changed.

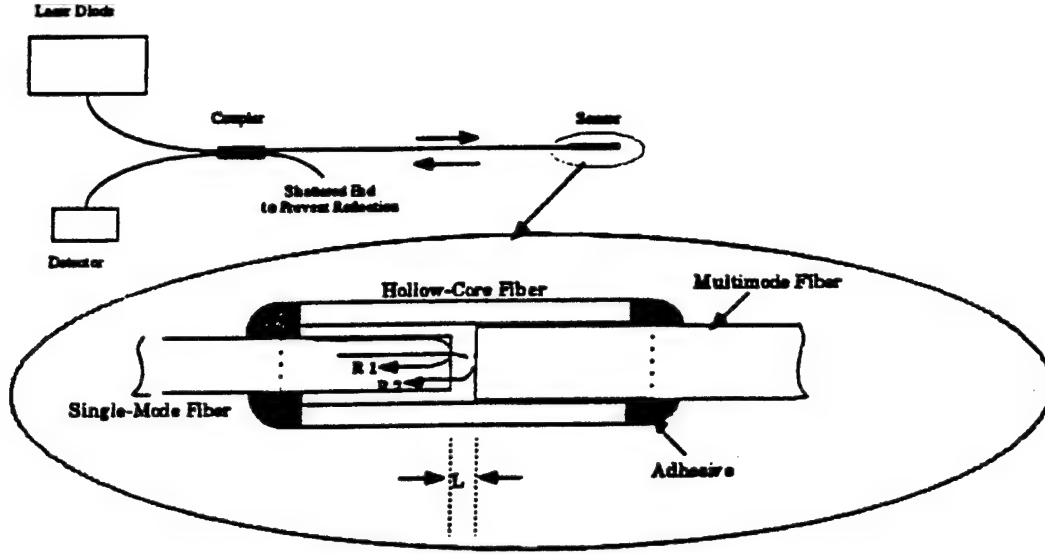


Figure 1 Typical EFPI sensor structure.

The optical wave fields of the two reflections could be represented in terms of its complex amplitude $U_i(x,z,t)$ given by

$$U_i(x,z,t) = A_i \exp(j\phi_i), \quad i=1,2 \quad (1.1)$$

where the variable A_i is a function of the transverse coordinate x and traveled distance z , and the subscripts $i=1,2$ stand for the reference and sensing reflections, respectively. Assuming that the reference reflection $A_1=A$, then the sensing reflection coefficient A_2 can be approximated by the simplified relation

$$A_2 = A \left[\frac{ta}{a + 2s \tan[\sin^{-1}(NA)]} \right] \quad (1.2)$$

where a is the fiber core radius, t is the transmission coefficient of the air-glass interface (≈ 0.98), s is the separation between the reflectors, and NA is the numerical aperture of the single mode fiber given as $NA = (n_1^2 - n_2^2)^{\frac{1}{2}}$, and n_1 and n_2 are the

refractive indices of the core and the cladding, respectively. The intensity detected at the photodiode is given as

$$I = |U_1 + U_2|^2 = A_1^2 + A_2^2 + 2A_1A_2\cos(\phi_1 - \phi_2) \quad (1.3)$$

which can be expanded as

$$I = A^2 \left[1 + \frac{2ta}{a + 2s \tan[\sin^{-1}(NA)]} \cos\left(\frac{4\pi s}{\lambda}\right) + \left(\frac{ta}{a + 2s \tan[\sin^{-1}(NA)]}\right)^2 \right] \quad (1.4)$$

we have assumed that $\phi_1 = 0$ and $\phi_2 = 2s(2\pi / \lambda)$, and λ is the wavelength in free space. The changes in the separation distance between the surfaces of the fibers aligned in the support tube produce a sinusoidal modulation of the output signal.

1.2 Magnetostriction of Ferromagnetic Materials

1.2.1 Magnetic Properties of Rare Earth-iron Compounds

The binary or pseudobinary compounds of the rare earth-Fe₂ (RFe₂) have large magnetostriction and magnetic anisotropies at 300K. Also, they have relatively high magnetic saturation and Curie temperature. These characteristics are useful in realizing magnetostrictive transducers, micro positioning devices, and permanent magnets. The magnetostriction for such materials can be expressed as [1.1]

$$\varepsilon = CH^2 \quad (1.5)$$

where C is $3\lambda_s/2H_A^2$, H is applied magnetic field intensity, λ_s is saturation magnetostriction, and H_A is anisotropy field. In order to be good fiber optic magnetostrictive sensors, the materials should have large magnetic saturation and smaller anisotropy field. There is a field in a ferromagnetic material which directs the magnetization along certain definite crystallographic axes called directions of easy

magnetization. This field is called anisotropy field. The rare earth compound TbFe_2 shows large magnetostriction, more than 2000 ppm with 25 kOe field strength, at room temperature but saturated above the field strength, whereas the compound DyFe_2 relatively shows small magnetostriction, about 700 ppm at the same field strength, but hardly be saturated [1.2]. Hence, the proper control of each element mole fraction gives maximum magnetostriction and high saturation magnetostriction value. The pseudobinary compound $\text{Tb}_x\text{Dy}_{1-x}\text{Fe}_2$ ($0 < x < 1$) exhibits a maximum magnetostriction / anisotropy ratio at $x \approx 0.3$ with 25 kOe [1.2].

1.2.2 Magnetic Properties of Metallic Glasses

Glasses are used and well-known to the world as with hardness, brittleness, and transparency of typical window materials which are made up mostly of silica and oxides of metals such as Al, Ca, K, Mg, and Na. The transition from the liquid to solid state is progressive and the viscosity of the melt increases with decreasing temperature. The eventual shear viscosity rises to be considered as solid for practical purposes. During this progressive transition from liquid to the solid state, the atoms do not form the regular crystalline structure but instead remain locally defined structure. Hence, the atomic arrangement of a glass is similar to that of liquid with the same composition. Metallic glasses, obtained by rapid quenching of metallic melts, are also non-crystalline or amorphous, like glasses, but also are different to the latter in several aspects. They are primarily composed of metallic elements and the bondings between the molecules are metallic in nature. They are usually opaque, not brittle but their physical, chemical, and mechanical properties are similar to those of traditional metallic materials, or even superior to those of their crystalline counterparts. Amorphous metals and alloys can be produced by several techniques such as the rapid solidification of metallic melts, vapor deposition, sputtering, electrodeposition, and irradiation. But the term used as metallic glass currently represents the material with reference to foils, powders, ribbons, tapes, wires, and strips which are obtained by rapid solidification process of alloy melts. The alloy melts are cooled through the specific temperature range, within which solidification or crystallization would normally occur at rates of between 10^5 and 10^8 K/s [1.3].

The metallic glasses show soft magnetic properties, which refers to the fact that the response of the magnetization to an applied field is large. For the magnetization to change in large value for a small applied magnetic field usually shows weakly coupled magnetization to the material. The material possesses a low magnetic anisotropy so that the magnetic moments are easily rotated by applied field at room temperature. The typical magnetic characteristics of the metallic glass for magnetic sensor application is discussed in the next section

1.3 Sensor Material Considerations

1.3.1 Survey of Candidate Magnetostrictive Materials

As we noted earlier, the magnetostrictions of TbFe_2 is greater than 2000 ppm at 25 kOe. The magnetostriction of ternary compound $\text{Tb}_x\text{Dy}_{1-x}\text{Fe}_2$ is high when the concentration of x is approximately 0.3. A metallic glass sample represents 30 ppm at saturation field strength of 30 Oe. By contrast, the saturation value of 1068 ppm is achieved by Terfenol ($\text{Tb}_{0.3}\text{Dy}_{0.7}\text{Fe}_2$) at near 25 kOe [1.2]. The magnetostriction for Terfenol is less than metallic glasses for low field of a few Oe. The metallic glass would be saturated at low field strength of near 30 Oe. It is observed that elongation of the Terfenol is about 500 ppm at 100 kA/m field intensity without pressure. The approximate flux density is 0.126 Tesla. In order to detect 100 nT flux density the Terfenol should respond to 0.076 A/m field intensity. At this intensity, Terfenol gives virtually no elongation. Hence, the low field detection can be done by using the other materials that responds to the weak field intensity, such as metallic glasses.

1.3.2 Experimental Investigation of Magnetostrictive Materials

Two candidate magnetostrictive materials were evaluated for the design and fabrication of the magnetic field sensors. According to the survey, Terfenol-D and Metglas are the two most commonly used magnetostrictive materials for magnetic field sensing applications. To test the sensitivity of the selected materials, an EFPI sensor based

testing system was constructed based on these materials. The experimental setup is shown in Figure 2. An EFPI sensor was attached to a Terfenol-D bar which was one inch long and 6 mm in diameter. A solenoid was used to generate magnetic field and the sensor was inserted inside the coil. The gage length of the EFPI sensor was 20 mm.

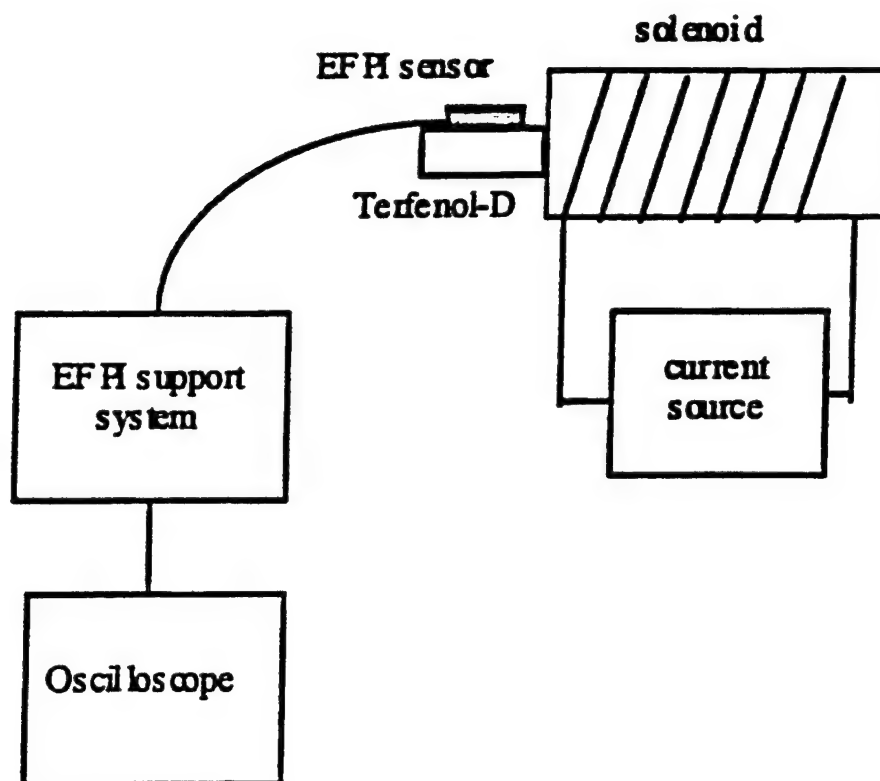


Figure 2 Schematic of the experimental setup used for the evaluation of candidate magnetostrictive materials.

A Gauss meter was used to monitor the magnetic field flux density and the field was increased from 0 to 600 Gauss. The dependence of the magnetic field induced strain to the applied field intensity shown in Figure 3. It is obvious from the figure that the Terfenol-D is insensitive to the low magnetic field (<450 Oe), but becomes very sensitive at high field level. Since the major objective of this research project is to design and fabricate magnetometers for weak magnetic fields (range 100 nT-40,000 nT), Terfenol-D was not found to be suitable for this application.

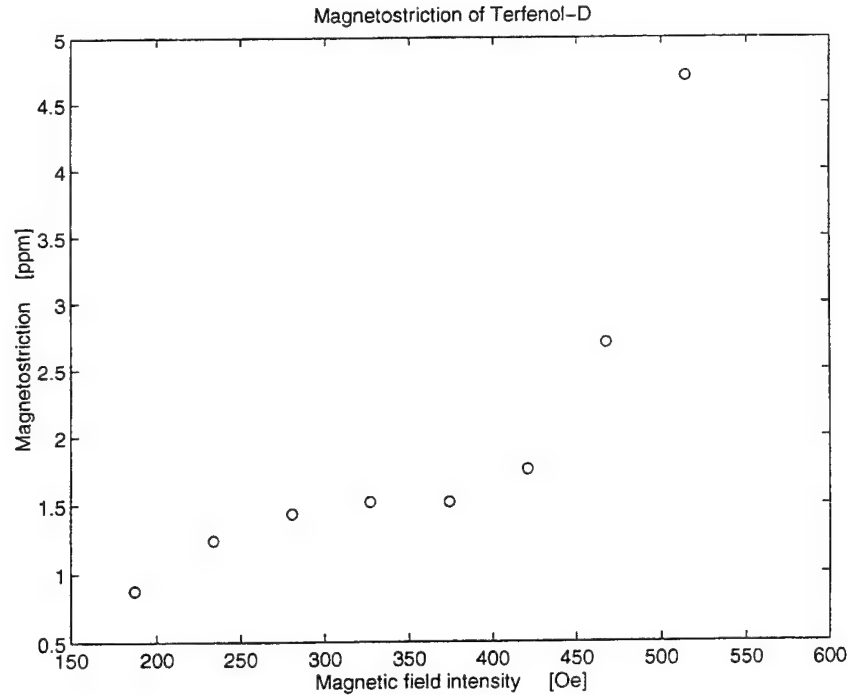


Figure 3 Magnetostriction as a function of magnetic field intensity for Terfenol-D.

In order to increase the magnetic field sensitivity at low fields, the other material such as Metglas 2605 ($\text{Fe}_{78}\text{B}_{13}\text{Si}_9$) was evaluated. A 25 mm long Metglas strip was used to bond with the fiber sensor to measure the magnetic field induced strain. The EFPI sensor used had a gage length of 20 mm. The sensor was attached on the Metglas strip with an epoxy based adhesive, and the applied field was increased from 0 to 50 Oe. The results are shown in Figure 4.

It was noted that Metgals-2605 had a small magnetostriction at both weak and strong fields but displayed high sensitivity mid intensity of applied fields. In order to measure the linear range of magnetostriction with a higher resolution, the current to the flux coil was controlled carefully. The field was increased from 4.5 to 9.5 Oe. The results are shown in Figure 5. It was observed that within 5-6 Oe, the field dependence was the most linear and sensitive. Hence,, the sensors biased at this field level can possess maximum sensitivity to the applied magnetic fields.

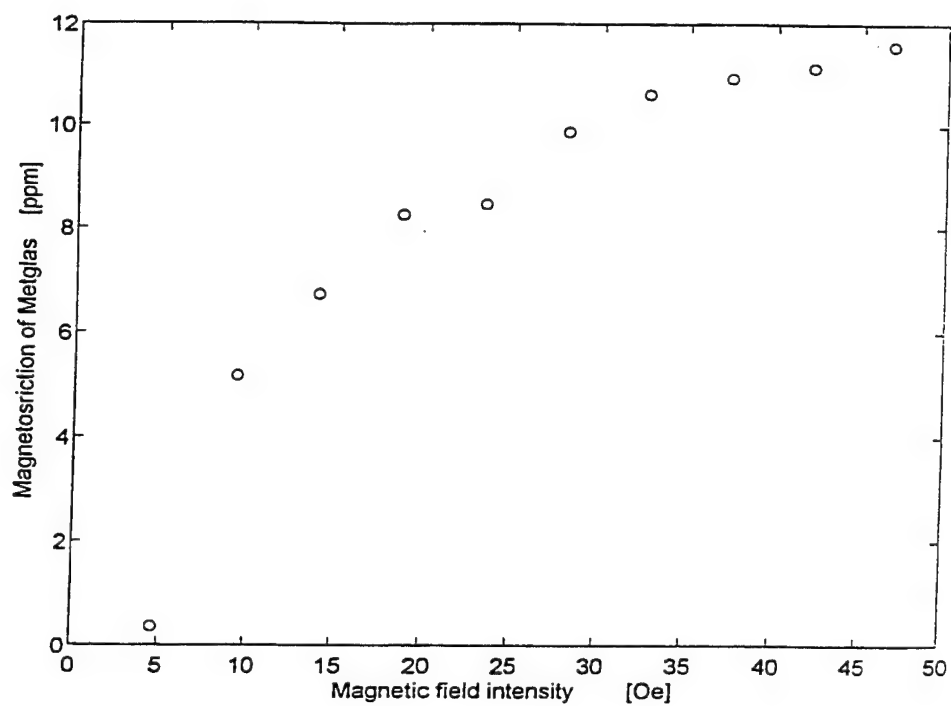


Figure 4 High field magnetostrictive characteristics of Metglas ($\text{Fe}_{78}\text{B}_{13}\text{Si}_9$) strip.

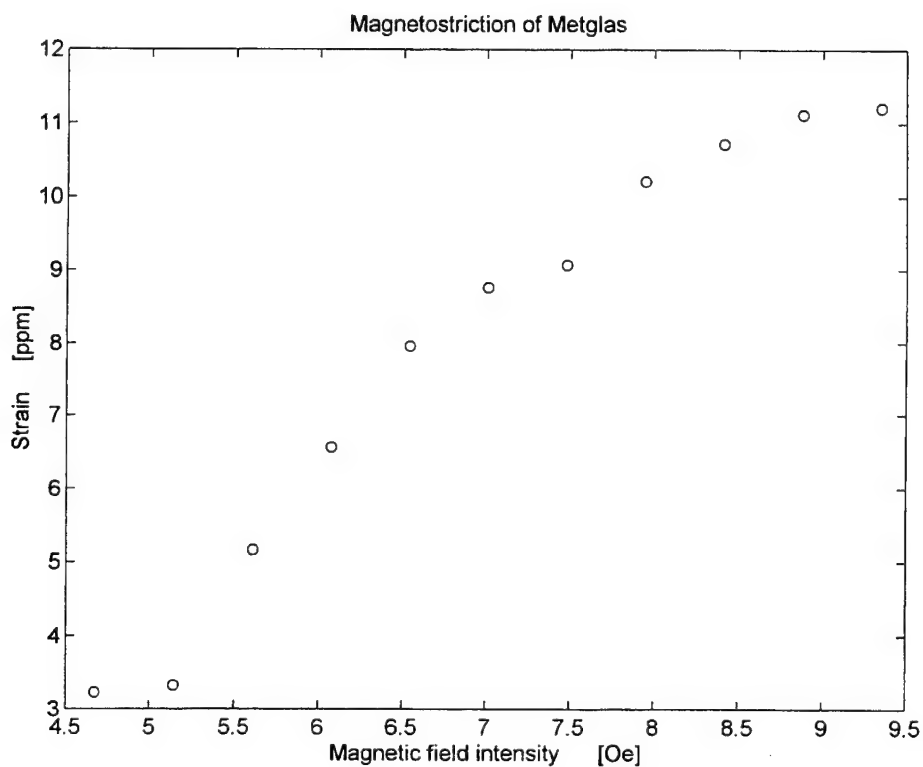


Figure 5 Low field magnetostrictive characteristics of Metglas ($\text{Fe}_{78}\text{B}_{13}\text{Si}_9$) strip.

1.4 Design of EFPI-based Optical Fiber Magnetic Field Sensors

1.4.1 Basic Sensor Design

The basic EFPI sensor was designed to evaluate candidate materials for magnetic sensor applications. A pure EFPI sensor with single mode fiber reflector was used and the same type fiber was used for lead in/output fiber. A 1300 nm single mode laser was used for light wave source. As we discussed earlier, the pure EFPI sensors was attached to Metglas strip or Terfenol-D rod by using epoxy, and magnetic field was applied to evaluate the magnetostrictive properties of each material. Since only strip-type Metglas strip was available at initial stage of the research, the basic sensor design at this stage for various material evaluation was based on simple EFPI configuration. The schematic of the EFPI sensor design is given in Figure 6.

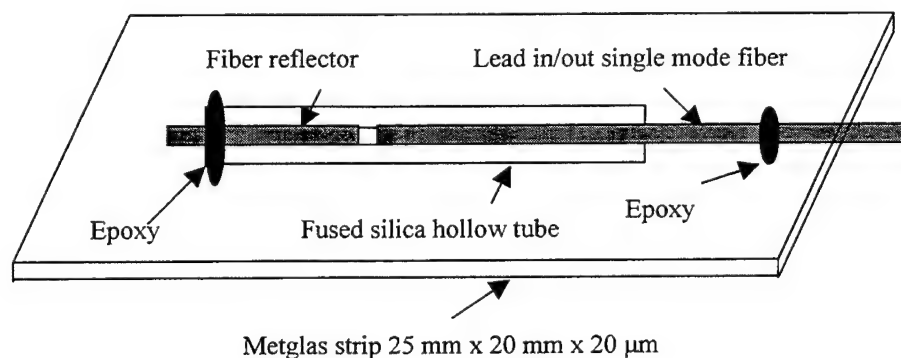


Figure 6 Basic sensor design used to evaluate magnetostrictive characteristics for the candidate material.

In order to test the minimum detectable magnetic field with fabricated EFPI sensors, a 5 Hz AC current source and a small coil were used to simulate the weak magnetic fields. The solenoid was used to provide the necessary field bias (5.5 G). The sensor used had a gage length of 20 mm. The data from the oscilloscope was signal processed using a digital signal processing techniques. Both low-pass and band-pass Butterworth filters

were designed to extract the applied 5 Hz signal from the noisy background. Figure show that the output signal without digital signal processing and after signal processing. The experimental results clearly demonstrate the feasibility of measuring magnetic fields with magnitude of 100 nT by the Metglas-bonded EFPI sensor elements.

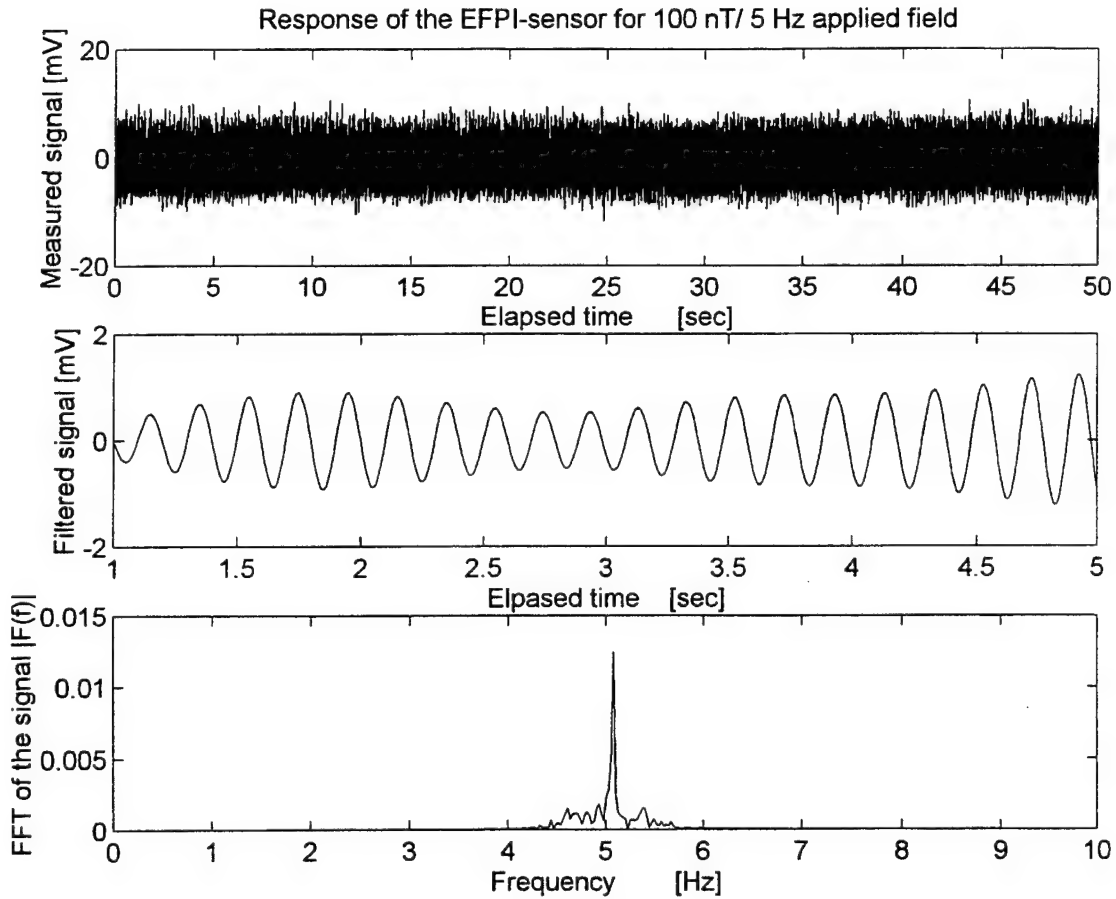


Figure 7 Noise reduction by a digital signal processing.

Although Metglas has been chosen as the primary magnetostrictive material for further investigation and sensor design, the temperature drift of the EFPI sensor is of major concern, especially when dealing with weak DC magnetic fields. The Q-point refers to the central point of the region where the sensor exhibits maximum linear sensitivity. The thermal expansion of Metglas has a dominant influence on signal stability since a 300 μm

change in the air gap between the reflectors makes sensor output change peak-to-peak value. The EFPI sensor gage used for the material evaluation had a temperature sensitivity of about $200 \mu\text{m}/^\circ\text{C}$. On the other hand, the maximum displacement of the sensor responding to 40,000 nT magnetic field was less than $100 \mu\text{m}$ which implies that the magnetostrictively induced displacement of the air gap is equivalent to that induced by one half a degree of temperature drift. Hence,, the temperature stabilization is crucial for obtaining the accurate and reliable long-term performance. An appropriate compensation scheme is thus necessary to account for the thermal drift of the sensor system. The theoretical model of temperature compensation can be utilized by a concept of the expansion of the different materials. If the proper materials and shapes are given, the compensation scheme is greatly simplified as compared to the conventional active temperature compensation schemes.

1.4.2 Design of Field Annealing System

A transverse field annealing technique is essential to induce a large magnetostriction. Here the annealing field and measurand field directions are orthogonal to each other to generate large magnetostriction in the EFPI sensor. The magnetostriction of Metglas wire can be strongly affected by the local domain structure. The easy axis at a location in the wire is dominantly influenced by the local stress. The macroscopic easy axis orientation is the weighted average value of the local vector directions. The field annealing relieves the local stress and produces uniaxial magnetic anisotropy. The change of magnetostriction [1.4] between before and after applied field is given by

$$\lambda(\theta) = 3/2 \lambda_s [\cos^2 \theta_2 - \cos^2 \theta_1] \quad (1.6)$$

where θ_1 and θ_2 are the angles before and after applied magnetic field respectively and λ_s is the saturation magnetostriction. The magnetostriction is proportional to the difference

of the initial and final angles. The transverse annealing and then applying longitudinal field give the reasonable magnetostriction. Figure 8 and Figure 9 show the domain structure of transverse annealed Metglas material before and after applied magnetic field, where \bar{M} is the domain magnetization per unit volume.

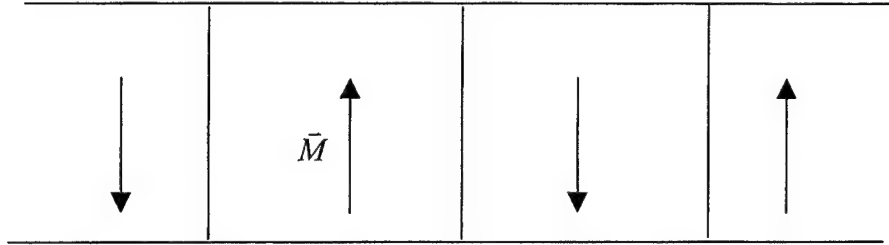


Figure 8 Domain structure of transverse annealed material.

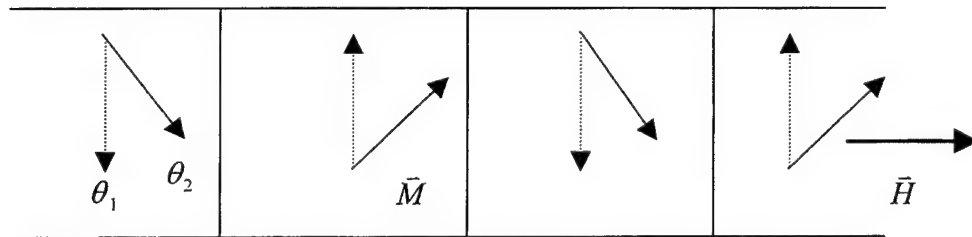


Figure 9 The domain structure of the material after applying longitudinal field \bar{H} .

It can be assumed that the direction of the magnetization is transverse to the axis and the local magnetostrictions are directed along easy axis before applying the longitudinal magnetic field. A field annealing system was constructed to enhance the performance of the Metglas wire based EFPI sensor system. The resistance wire was used to heat the ceramic tube which produces the temperature range of 382 ~ 400 °C. In order to avoid the generation of the 60 Hz magnetic field from the heating system, a DC power supply was designed to supply the current to the heating coil. The annealing temperature was

controlled by a microprocessor-controlled temperature controller. A solenoid was made on the 6 cm diameter ceramic tube which is suitable for insulating the heat from the heating coil. The flux density generated by this coil was 52-82 G. The preliminary system fabricated is shown in Figure 10.

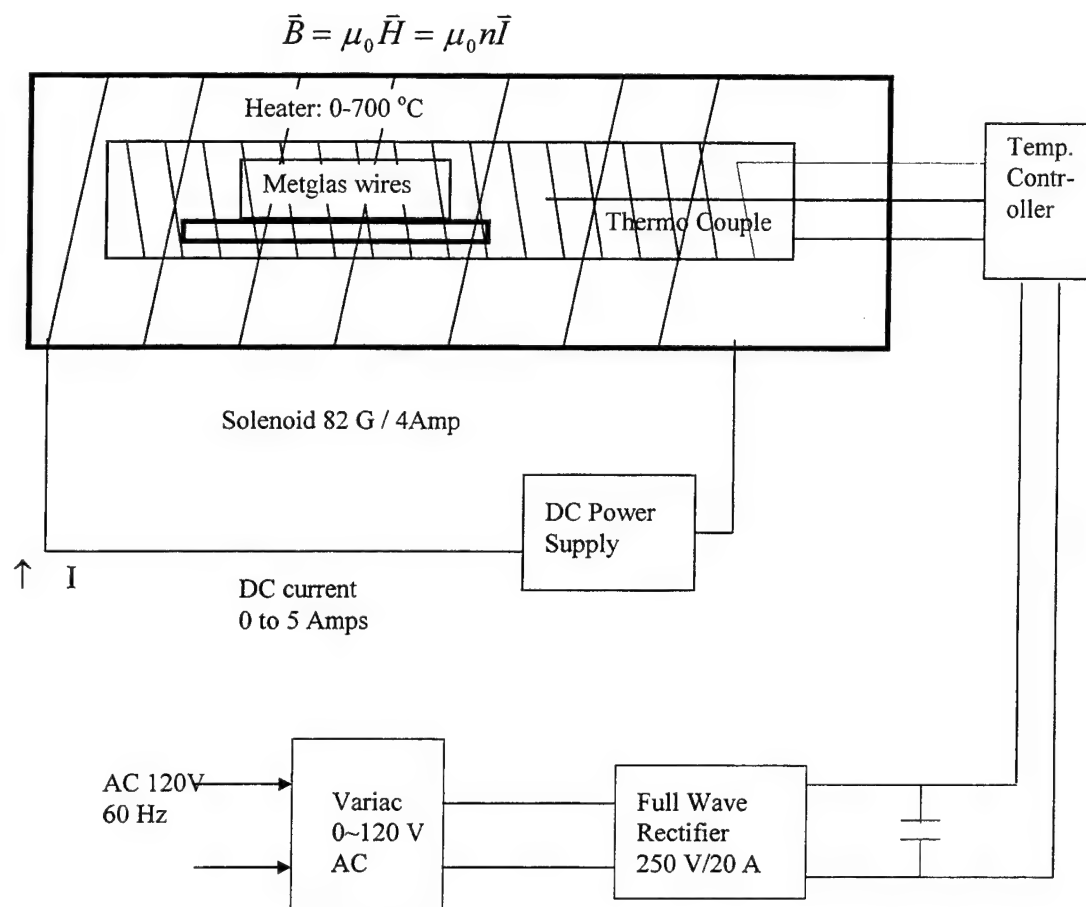


Figure 10 Preliminary field annealing system.

The annealing was prepared by cutting the Metglas wires into several lengths such as 1.25 cm , 2.54 cm and 3 cm. The wires were inserted into the hollow core tubes with an inner diameter of 150 μ m. The inserted wires were relatively straight after the annealing. The time for applying heat from 22 °C to 382 °C was 10 minutes and the annealing temperature, 382 °C, was sustained about 1 hour, then the system was cool

down to 22 °C for 45 minutes. The gradient of the temperature rising and cooling down times can be controlled by changing the applying DC voltage which is governed by the input variac power source. The annealed Metglas wires were straight but gave some friction in movement in the hollow core tube because of the oxidation. The field annealing curve is given in Figure 11.

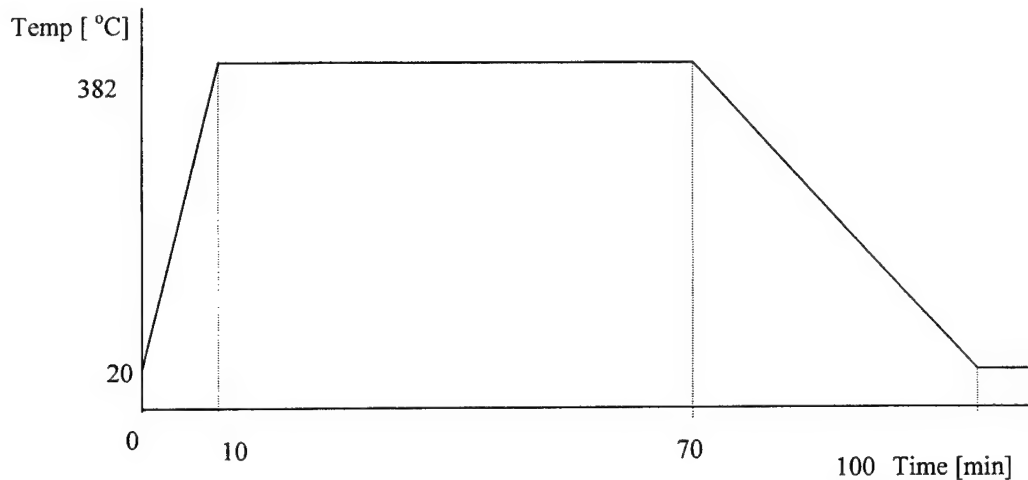


Figure 11 Annealing temperature curve.

The magnetostriction of the unannealed Metglas wire was observed to be only one half as that of Metglas sheet material. The sensor length was 2.54 cm long and had a saturation magnetostriction of about 6 ppm. The annealed Metglas wire of 1.25 cm showed a similar saturation magnetostriction. Figure 12 shows the experimentally measured response of the EFPI-based sensor based on unannealed Metglas wire.

The magnetostriction of the Metglas wire is seen to be saturated at about 50 G of flux density. The magnetic field sensitivity of Metglas wire can be enhanced by increasing the wire length. This geometry also displays vibration insensitivity. The annealing gives a straight wire which prevents the low magnetic field sensitivity loss due to friction between the hollow core tube and the sensing material. If the proper annealing and the biasing are given, this Metglas wire-based technique looks promising for the low magnetic field sensor applications. The typical magnetostrictive characteristics after the field annealing for Metglas wire is shown in Figure 13.

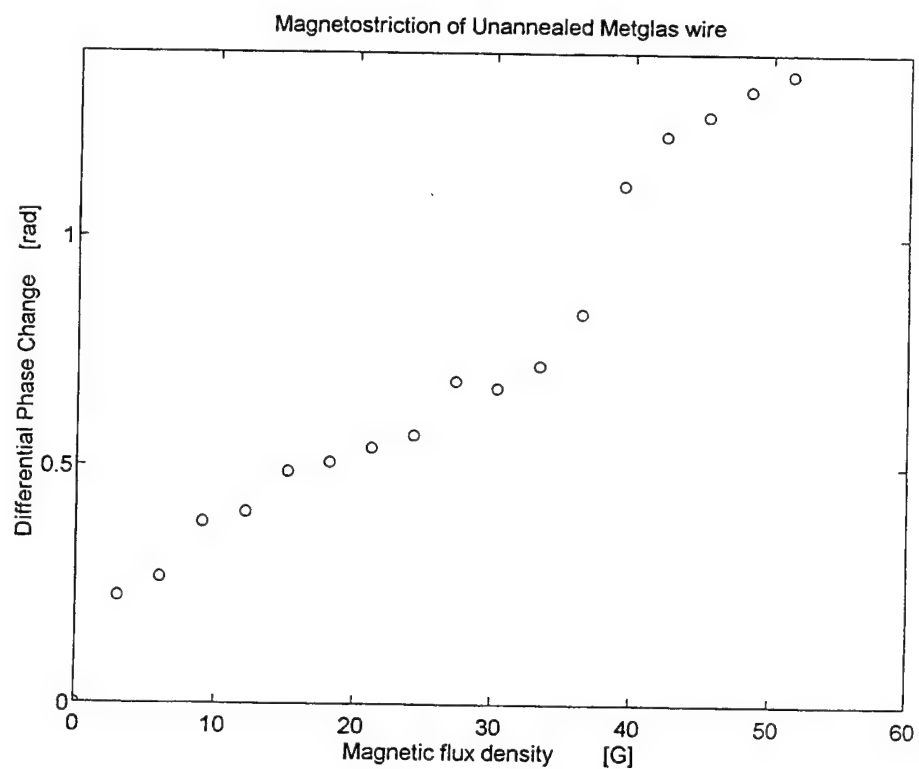


Figure 12 Unannealed sensor material response to the applied external field.

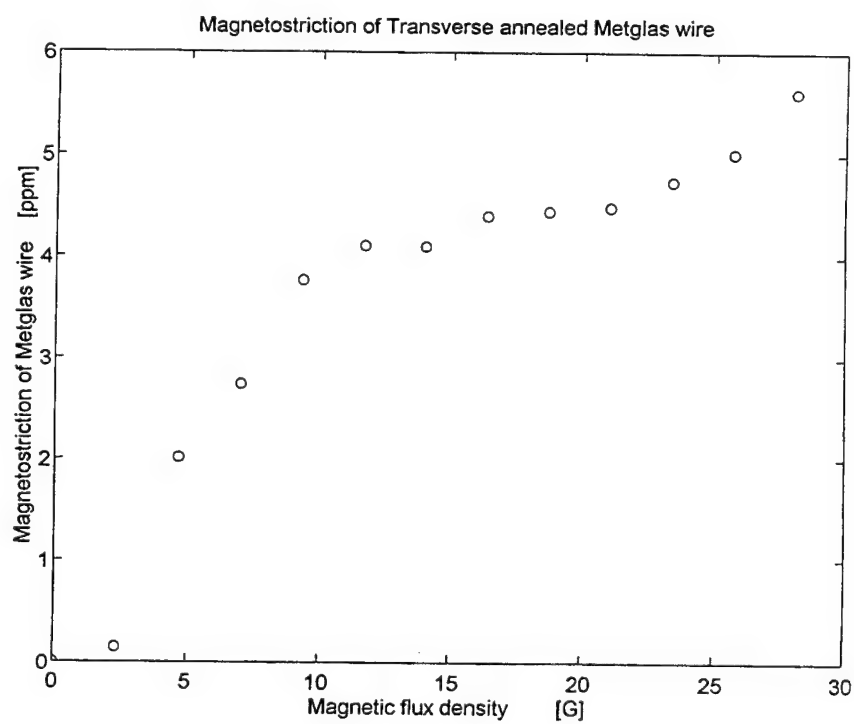


Figure 13 DC-magnetic field response of Metglas wire ($\text{Fe}_{77.5}\text{B}_{15}\text{Si}_{7.5}$).

1.4.2 Novel Sensor Design

The detection of magnetic field is achieved by measuring the change in optical path length due to external perturbations. The fiber gage length of an intrinsic sensor is around 30m long for low magnetic field detection, when it employs magnetostrictive materials in various geometries as the transduction mechanism. The conventional intrinsic and extrinsic Fabry-Perot sensors select one of the schemes to detect a low magnetic field. The disadvantage of these schemes is their vibration sensitivity when the measurands are very weak. The optical fibers in those cases usually are wrapped around a cylinder type magnetostrictive material, or bonded onto a flat ribbon directly, to produce the optical path length change caused by the measurand. The EFPI sensor suffers from the bending of magnetostrictive ribbon, which implies low sensitivity, unpredictable operating position and large vibration sensitivity. Hence,, the disadvantages of the existing sensor designs limit the low magnetic field detection using optical fibers.

One of the major objectives of modifying the original metal sheet shape to the other type was to reduce the vibration sensitivity of the EFPI based sensor. The Metglas strip is too flexible to make it a small diameter cylindrical shape. It was experimentally observed that the cylindrical walls of the Metglas strip were partially broken when the radius of curvature was reduced to the diameter of 3 mm. This means that the radial stress is very high. The disadvantages mentioned above can be avoided by introducing a novel sensor scheme. The basic concept of the design is to use a magnetostrictive material as a reflector/gage in an EFPI based sensor. The EFPI-sensor uses a hollow core tube for alignment and guide to both fiber sensing arm and reflector/gage. Hence,, a wire shape magnetostrictive material is chosen for this purpose. The diameter of the Metglas wire is 125 μ m and that of the glass hollow core is 128 μ m. Hence,, the insertion into the glass tube is difficult. The Metglas wire also has the diameter fluctuations and is severely bent. Therefore it is almost impossible to insert the wire into the relatively straight hollow core glass tube. The other way to realize the EFPI with the wire is to insert the wire into a stainless steel hollow core tube with the diameter of 130~135 μ m and then perform the

field annealing. This annealing gives relatively straight wire to prevent the magnetostrictive sensitivity loss due to the friction between the bent wire and the hollow core tube wall and increases the low magnetic field sensitivity. The one of the endfaces of annealed wire then will be polished which is to be used as a reflector. The reference arm is a single mode fiber and the sensing arm is the Metglas wire. The hollow core tube can be either a glass or stainless tube with the diameter of 130~135 μ m. This design provides an inherent advantage on the vibration insensitivity. Since both the reference fiber and Metglas wire (sensing material) are inserted into the thin hollow core tube, the transverse movements of the arms are relatively small compared to the longitudinal movements induced by the magnetic field which is to be detected by this movement that gives airgap change between the arms. Hence, the sensor configuration and the temperature compensation scheme are well simplified. This design of the sensor gage is given in the Figure 14. If the CTE of fiber, Metglas wire and hollow core tube are C_f , C_m and C_t , respectively, the balance equation is given by

$$(C_m - C_t) L_1 = (C_t - C_f) L_2 + dlC_t \quad (1.7)$$

and $C_m > C_t > C_f$ should be satisfied, and dl is the air gap between the fiber and Metglas wire. The temperature compensation can be done by the scheme. Hence,, this novel sensor design is robust and stable for the detection of weak magnetic fields.

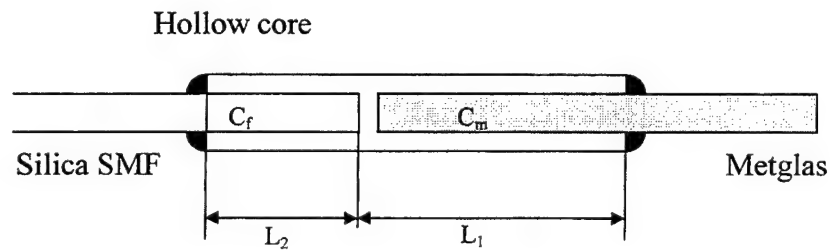


Figure 14 A novel EFPI based sensor design for low magnetic field measurements.

1.4.3 Enhancement of Performance of Transverse Field Annealed Metglas Wire

The increase of applied transverse magnetic field ensures the uniaxial magnetic anisotropy in the Metglas materials. The anisotropy gives a magnetostriction to the material. In order to rotate the magnetizations in the material, a high field may be required when the magnetic properties of the material are unknown. The rotation of magnetization is easily achieved when the material is heated up to the Curie temperature with the simultaneous application of transverse magnetic field. A Metglas wire was prepared to be evaluated for low magnetic field detection. A slightly increased transverse magnetic field was applied to the materials by using a ceramic foam insulating block upon the heating element. This insulating block allows the decrease in the air gap between the two transverse field annealing air core solenoids. The generated transverse field was 82 Oe which is 30 Oe greater than that of the previous one. The annealing temperature was 392 °C and the duration of 120 min as before. Figure 15 shows the high field magnetostrictive characteristics of the Metglas wire. The saturation magnetostriction is about 8 ppm which is 3.5 ppm greater than that of 52 Oe transverse field annealed material. The low field response is also given in Figure 16. The response of the material is linear in the range of 2 to 6 Oe. The sensitivity of the sensor system is 1.25 ppm/Oe in the linear range. Hence, a bias of 4 Oe can be used for sensitive response and for determination of field direction. The sensor was adjusted to avoid the saturation of laser diode by the reflected waves in the EFPI sensor system by controlling the distance between the fiber and Metglas reflector. The reflectance of the glass-air interface is about 4 % and that of the Metglas reflector-air interface may be as high as 50 %. If I_1 and I_2 are the intensities of each interface, the fringe visibility is about 0.54 with short distance between the interfaces. The intensity I_2 is about 11.52 times higher than I_1 for very small air gap. The large reflectance causes instability in lasing system. A large portion of originating intensity returns back to the system, which is about 50 %. In order to avoid the instability of source laser output and to increase the fringe visibility which has a maximum value when the two intensities are same, the air gap between the interfaces was controlled to get maximum fringe visibility by using micropositioner. The controlled air gap was 3.5 mm for a laser diode current of 22.3 mA.

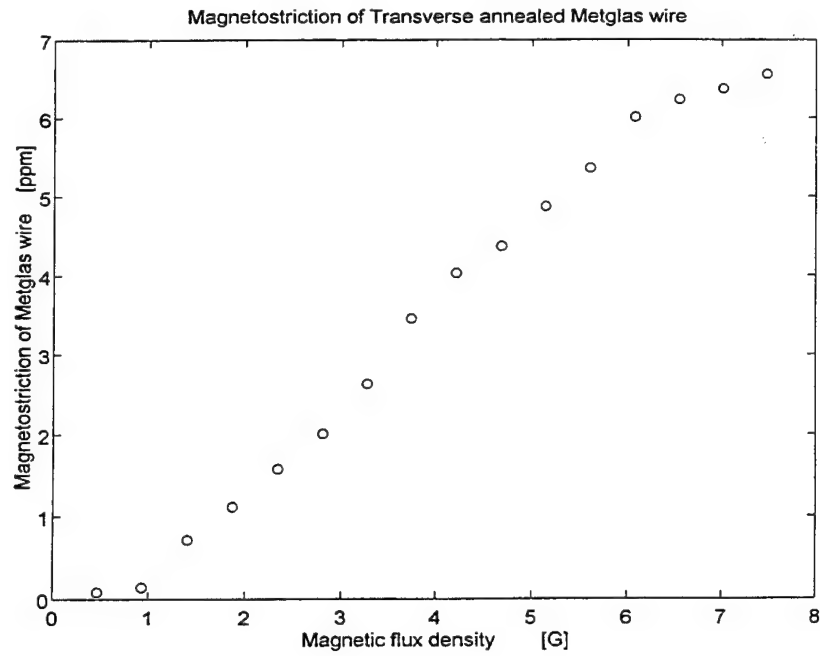


Figure 15 Enhancement of magnetostriction, low magnetic field, with increasing annealing field.

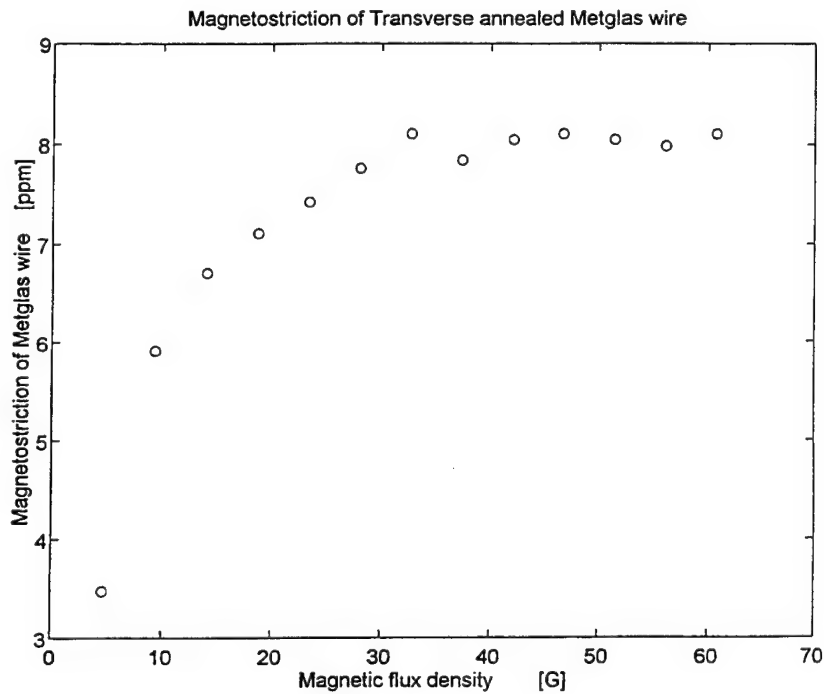


Figure 16 Enhancement of magnetostriction, high magnetic field, with increasing annealing field.

The hollow core tube for this sensor was 150 μm that was 10 μm smaller than that of preliminary design. The gage length was 2.5 cm and the diameter was 125 μm . Further enhancement has been accomplished so as to use 140 μm hollow core tube that reduces the vibration sensitivity a lot. Hence, the sensor system is more stable.

1.5 Signal Demodulation

1.5.1 Introduction to Signal Demodulation

Since the EFPI sensor is an interferometric sensor, it suffers from certain inherent limitations common to the majority of interferometric fiber sensors. First of all, sensitivity of the sensor is sensitive to the operating point of the sensor. Since the fringe variation for the lowest measurement value, 100 nT, is 1/400 of quarter fringe, the accurate control of the point is Hence, essential for reliable performance. Since the wavelength of the light source used is on the order of microns, the accurate adjustment of the operating point is difficult. The second limitation is observed from the fact that the relationship between the optical path difference and output intensity is periodic. Unique determination of the optical path difference is thus hard to achieve with the conventional signal detection schemes. If the operating point of the sensor is driven near the sensitivity minima, the peak or bottom of the fringe, there is no way to determine the direction of applied strain. To overcome these limitations, the quadrature phase detection scheme is employed.

1.5.2 Principles of Quadrature Signal Demodulation

The quadrature demodulation ensures the signal phase detection regardless of the initial phase point of an EFPI sensor. Using two 90° phase shifted sensors gives optimal phase

signal at any optical path difference in the interferometer. The sensor for one-dimensional magnetic field detection is given in Figure 17.

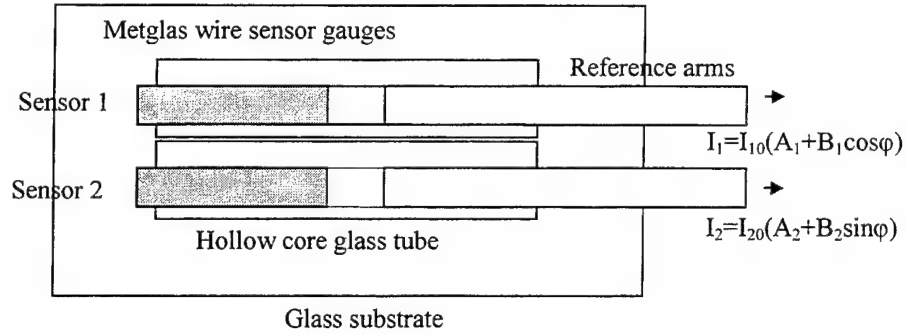


Figure 17 90° phase shifted sensor system for quadrature signal demodulation.

The output intensity in a two-beam interferometer may be written as

$$I = I_0(A + B \cos \phi) \quad (1.8)$$

Where ϕ is the phase difference between the two beams, and A and B are constants. If there are two interferometers with their output signals 90° out of phase, then the output intensities of the two interferometers are

$$I_1 = I_{10}(A_1 + B_1 \cos \phi) \quad (1.9a)$$

and

$$I_2 = I_{20}(A_2 + B_2 \sin \phi) \quad (1.9b)$$

where the coefficients are defined similarly as in Eq. (1.8). In order to recover the phase signal ϕ , the quadrature demodulation algorithm is applied as follows. The change in phase signal $\Delta\phi$ is of interest instead of the absolute value of ϕ in measurement. When the change in phase signal is small, the following approximations hold

$$\Delta I_1 = -I_{10}B_1 \sin \varphi \Delta \varphi \quad (1.10a)$$

and

$$\Delta I_2 = I_{20}B_2 \cos \varphi \Delta \varphi \quad (1.10b)$$

Defining a signal S in the following way

$$S = \sqrt{(\Delta I_1)^2 + (\Delta I_2)^2} \quad (1.11)$$

It can be easily proved that if the coefficients of the two signals in Eq. (1.10) are adjusted to be equal, i.e., $I_{10}B_1 = I_{20}B_2 = K$, the signal defined in Eq. (1.11) will be

$$S = K \Delta \varphi \quad (2.12)$$

In short, by taking the two steps described in the Eq. (1.10) and Eq. (1.11), the output signal S will be linearly proportional to the change of phase signal and independent of the initial value of the phase signal φ . Each sensor can be either adjusted to the output of $I + \cos \varphi$ by adjusting the air gap to have the intensity at the peak or bottom position of peak to peak interference fringe, or to $I \pm \sin \varphi$ by bringing the intensity middle of the fringe. Figure 1.18 shows 90° phase shifted sensor outputs that are produced from the expansion of Metglas sensor gages of 2 cm long with applying heat to the tip of it. Hence, small changes in phase can be readily detected at any position in each sensors. When the output of one of the sensors starts to fade, the other sensor output becomes larger.

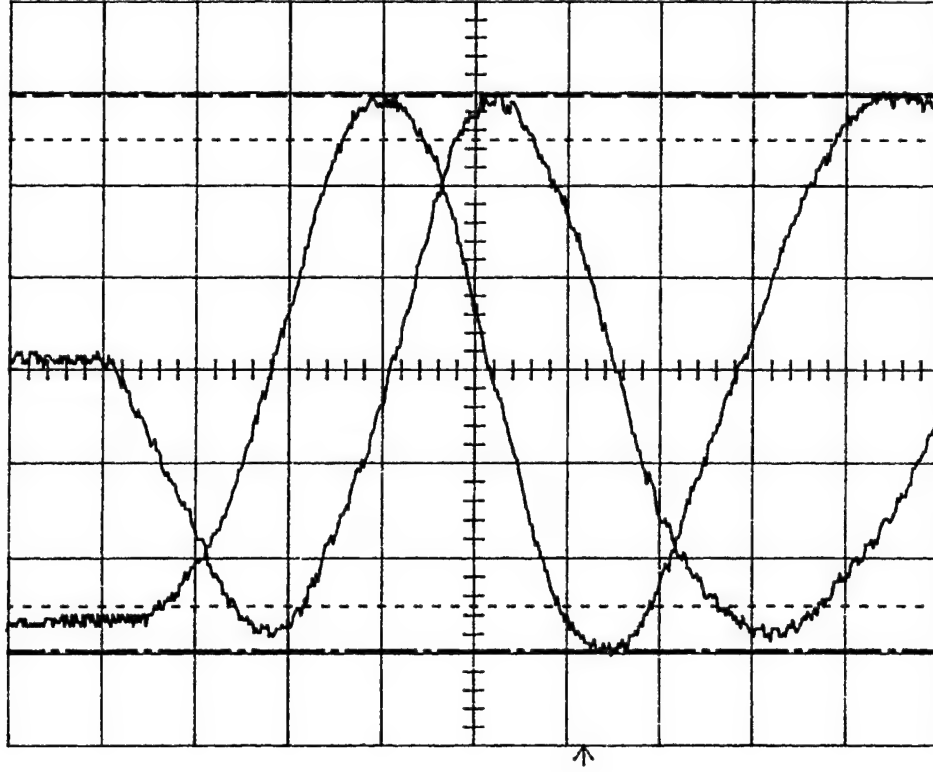


Figure 18 Quadrature (90°) phase shifted sensors.

1.5.3 Circuit Design for Quadrature Signal Demodulation

Once the distance between the Metglas wire and the fiber is adjusted, such that the two sensors are about 90 degrees out of phase, the next stage is to get an electrical output from these sensors and condition them in a way as to get the phase information from them. The laser source used for the sensor system also has a photo detector inside and gives an electrical output proportional to the reflected signal. The electrical output from the sensors is given as follows for general cases

$$V_1 = V_{dc1} + V_{max1}(1 + \cos \varphi) \quad (1.13a)$$

$$V_2 = V_{dc2} + V_{max2}(1 + \sin \varphi) \quad (1.13b)$$

where the V_{dc} term is due to the intensities of the primary and secondary reflections and is dependent on the source output, gain of the amplifier, cleave angles of the fiber and wire,

and actual gap length. The V_{max} term is due to the interference of the primary and secondary reflections. In order to get the phase information from this signal, it is necessary to eliminate the V_{max} and V_{dc} terms. The resulting signal is differentiated to get the following output,

$$V_1' = -\sin \varphi \Delta \varphi \quad (1.14a)$$

$$V_2' = \cos \varphi \Delta \varphi \quad (1.14b)$$

These outputs are then squared and added to remove the sine and cosine terms, and finally the square root of the resulting signal is obtained, which is only $\Delta \varphi$. The main advantage of this kind of a signal demodulation scheme is that the output is independent of the initial phase φ , and is dependent only on the change in phase, which is really of interest. Moreover, maintaining the initial phase constant is difficult as source fluctuations, thermal variations and other minor changes affect the initial operating point. But it may be safely assumed that these will affect both the sensor arms to the same extent and the phase difference between them will be maintained. The block diagram of this scheme is shown in Figure 19. The gain, A, between the differentiator and the squaring circuitry is added to match the output and input of these circuits. The output of the demodulation circuit on the whole is not just $\Delta \varphi$ in this case but is A times $\Delta \varphi$.

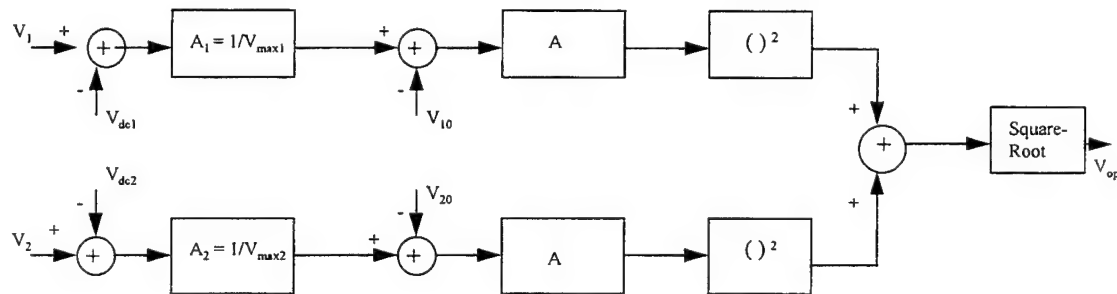


Figure 19 Block diagram of the analog quadrature demodulation circuit.

The block diagram shown in Figure 19 is implemented by using simple Op-Amps and IC AD 734 which is an Analog Multiplier-Divider. The circuit diagram for the demodulation scheme is shown in Figure 20.

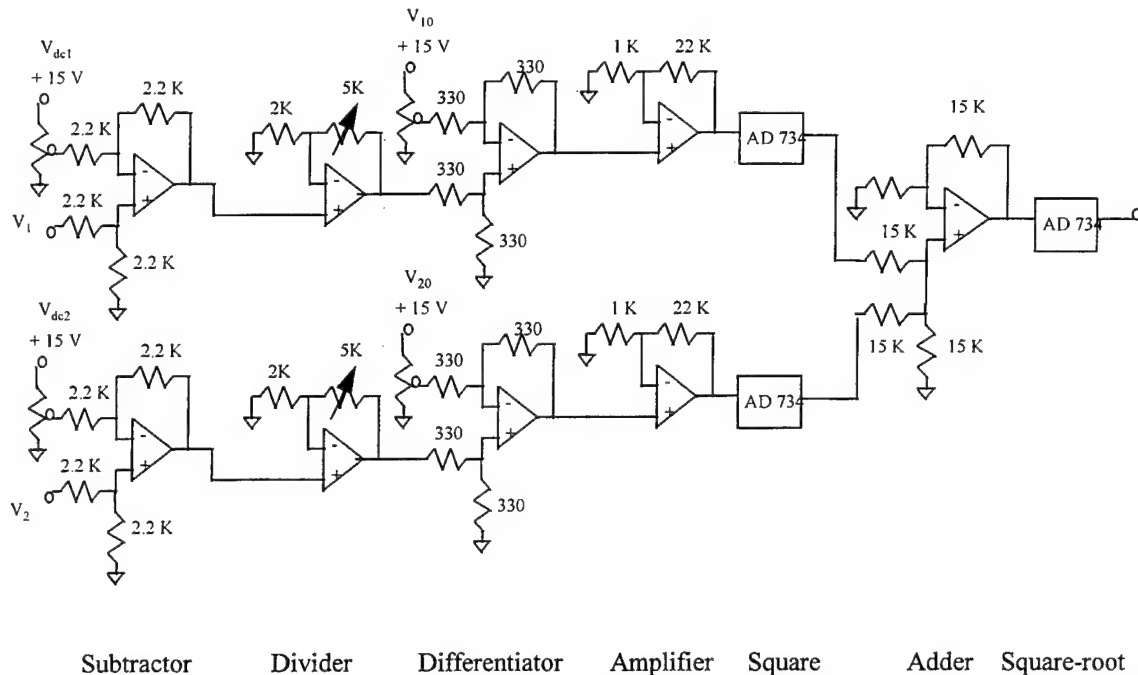


Figure 20 Circuit diagram for the analog demodulator.

1.5.4 Evaluation of Quadrature Signal Demodulation Circuit

In order to evaluate the performance of the demodulation circuit, measurements for various initial and transition points were taken. The inputs were externally generated and applied to the circuit. The observations and results are shown in Tables 1 through 4. The normalized output are given as

$$V_1 = 1 + \cos \varphi \quad (1.15a)$$

$$V_2 = 1 + \sin \varphi \quad (1.15b)$$

The values of V_1 and V_2 were initially calculated and then applied externally to the circuit. The range of this demodulation scheme is valid when the optical phase change is smaller

than unity. A large change in phase generates nonlinear distortion. The operating range specified in this project is of 1 mG to 0.4G which does not cause such a problem.

Table 1 Initial phase = 0 deg

Initial Phase (deg)	Change in Phase (deg)	V_1 (v)	V_2 (v)	Output (v)
0.0	0.0	2.0	1.0	0.196
0.1	0.1	1.999	1.002	0.54
0.2	0.2	1.999	1.004	0.69
0.3	0.3	1.999	1.005	1.02
0.4	0.4	1.999	1.007	1.26
0.5	0.5	1.999	1.009	1.6
0.6	0.6	1.999	1.011	1.8
0.7	0.7	1.999	1.012	2.11
0.8	0.8	1.999	1.014	2.48
0.9	0.9	1.999	1.016	2.74
1.0	1.0	1.999	1.017	3.04
1.1	1.1	1.999	1.019	3.35
1.2	1.2	1.999	1.021	3.5
1.3	1.3	1.999	1.023	3.73
1.4	1.4	1.999	1.024	3.83
1.5	1.5	1.999	1.026	4.28
1.6	1.6	1.999	1.028	4.39
1.7	1.7	1.999	1.03	4.78
1.8	1.8	1.999	1.031	4.95
1.9	1.9	1.999	1.033	5.08
2.0	2.0	1.999	1.035	5.5

The gradient of this curve is $5.304/2$. Hence, the calibration factor for the phase signal is 0.377. If the output voltage is 3.83 V, then the measured phase signal is $3.83 \times 0.377 = 1.444$ degrees. From the table, the actual value of this signal is 1.4 degrees. Hence, the relative error of this circuit is $|1.444 - 1.4|/1.444 = 3.05\%$. This is shown Figure 21.

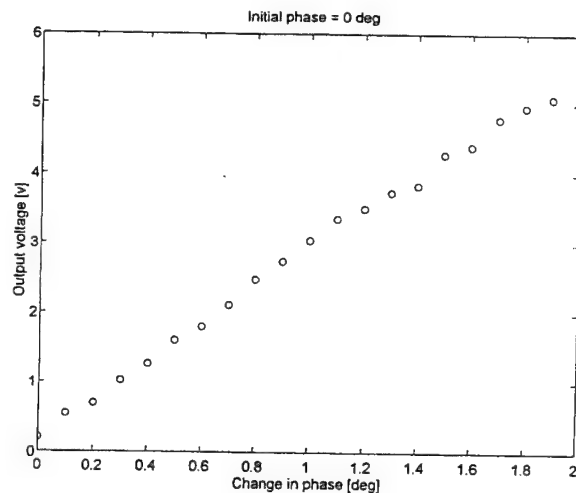


Figure 21 Output voltage vs change in phase.

Table 2 Initial phase = 90 deg

Initial Phase (deg)	Change in Phase (deg)	V_1 (v)	V_2 (v)	Output (v)
90.0	0.0	1.0	2.0	0.385
90.1	0.1	0.998	1.999	0.612
90.2	0.2	0.997	1.999	0.82
90.3	0.3	0.995	1.999	0.946
90.4	0.4	0.993	1.999	1.165
90.5	0.5	0.991	1.999	1.425
90.6	0.6	0.99	1.999	1.75
90.7	0.7	0.988	1.999	2.01
90.8	0.8	0.986	1.999	2.23
90.9	0.9	0.984	1.999	2.65
91.0	1.0	0.983	1.999	2.81
91.1	1.1	0.981	1.999	3.02
91.2	1.2	0.979	1.999	3.3
91.3	1.3	0.977	1.999	3.63
91.4	1.4	0.976	1.999	3.78
91.5	1.5	0.974	1.999	4.09
91.6	1.6	0.972	1.999	4.39
91.7	1.7	0.97	1.999	4.65
91.8	1.8	0.969	1.999	4.85
91.9	1.9	0.967	1.999	5.12
92.0	2.0	0.965	1.999	5.22

The gradient of this curve is $4.735/1.9$. Hence, the calibration factor for the phase signal is 0.401. If the output voltage is 3.02 V, then the measured phase signal is $3.02 \times 0.401 = 1.211$ degrees. From the table, the actual value of this signal is 1.1 degrees. Hence, the relative error of this circuit is $|1.211 - 1.1|/1.211 = 9.17\%$. This is shown Figure 22.

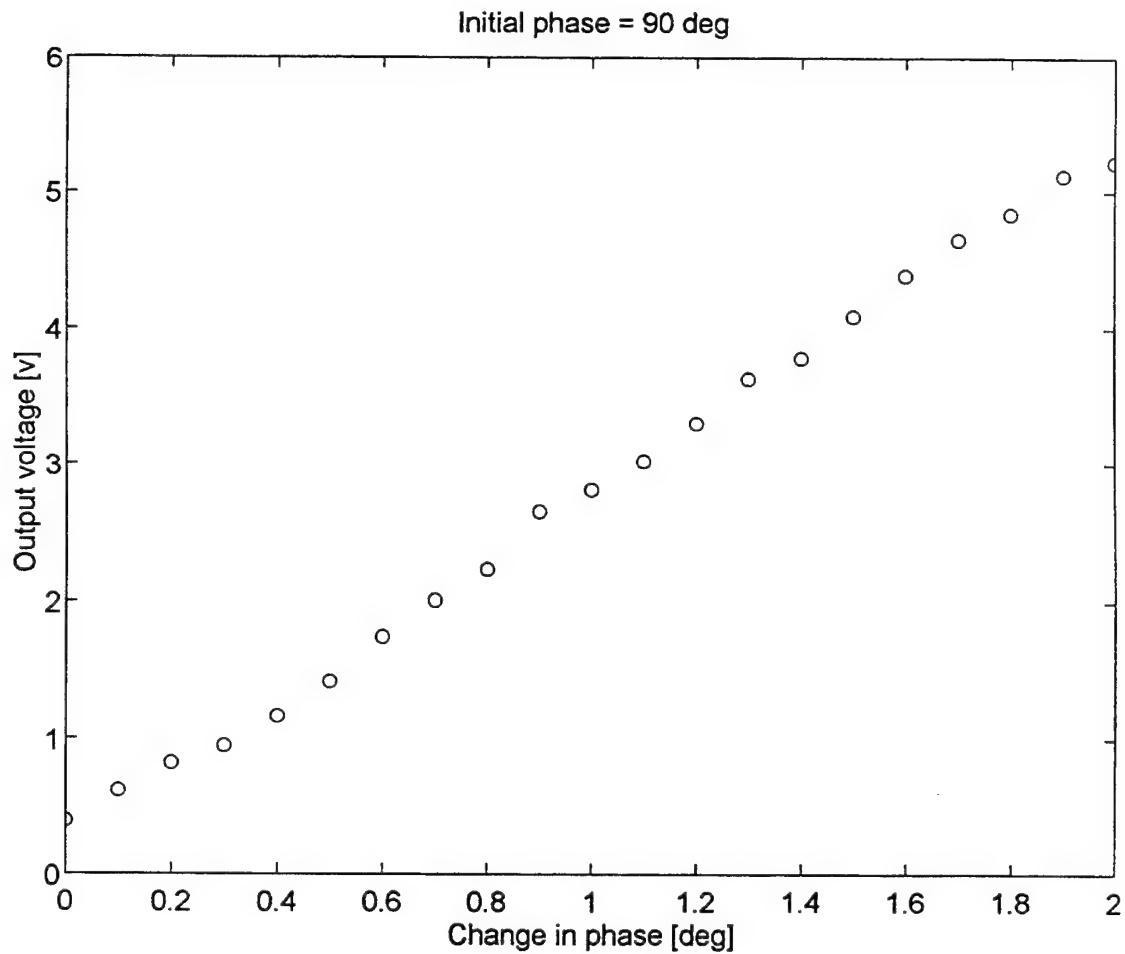


Figure 22 Output voltage vs change in phase.

Table 3 Initial phase = 180 deg

Initial Phase (deg)	Change in Phase (deg)	V_1 (v)	V_2 (v)	Output (v)
180.0	0.0	1.0	0.0	0.09
180.1	0.1	0.998	0.0	0.55
180.2	0.2	0.997	0.0	0.8
180.3	0.3	0.995	0.0	1.07
180.4	0.4	0.993	0.0	1.28
180.5	0.5	0.991	0.0	1.64
180.6	0.6	0.99	0.0	1.7
180.7	0.7	0.988	0.0	2.16
180.8	0.8	0.986	0.0	2.32
180.9	0.9	0.984	0.0	2.64
181.0	1.0	0.983	0.0	2.97
181.1	1.1	0.981	0.0	3.05
181.2	1.2	0.979	0.0	3.45
181.3	1.3	0.977	0.0	3.72
181.4	1.4	0.976	0.0	4.1
181.5	1.5	0.974	0.0	4.19
181.6	1.6	0.972	0.0	4.57
181.7	1.7	0.97	0.0	4.8
181.8	1.8	0.969	0.0	5.03
181.9	1.9	0.967	0.0	5.25
182.0	2.0	0.965	0.0	5.67

The gradient of this curve is $5.58/2$. Hence, the calibration factor for the phase signal is 0.358. If the output voltage is 3.05 V, then the measured phase signal is $3.05 \times 0.358 = 1.092$ degrees. From the table, the actual value of this signal is 1.1 degrees. Hence, the relative error of this circuit is $|1.092 - 1.1|/1.092 = 0.73\%$. This is shown in Figure 23.

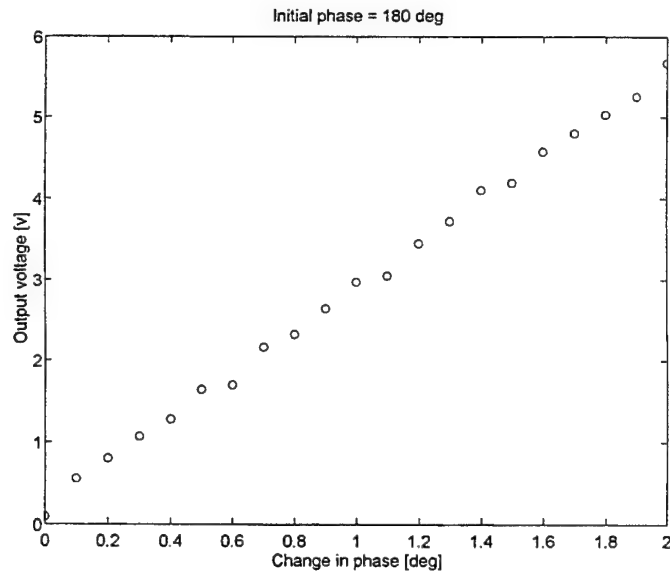


Figure 23 Output voltage vs change in phase.

Table 4 Initial phase = 0 deg

Initial Phase (deg)	Change in Phase (deg)	V_1 (v)	V_2 (v)	Output (v)
0	0	2.0	1.0	0.001
10	10	1.985	1.174	0.778
20	20	1.94	1.342	1.646
30	30	1.866	1.5	2.46
40	40	1.766	1.643	3.27
50	50	1.643	1.766	4.05
60	60	1.5	1.866	4.81
70	70	1.342	1.94	5.52
80	80	1.174	1.985	6.2
90	90	1.0	2.0	6.83
100	100	0.826	1.985	7.41
110	110	0.658	1.94	7.93
120	120	0.5	1.866	8.38
130	130	0.357	1.766	8.79
140	140	0.234	1.643	9.12
150	150	0.134	1.5	9.38
160	160	0.06	1.342	9.44
170	170	0.015	1.174	9.67
180	180	0.0	1.0	9.71

This curve is very non-linear, Hence, there is no way the phase signal can be exactly determined even if the output voltage is known. This is shown in Figure 24.

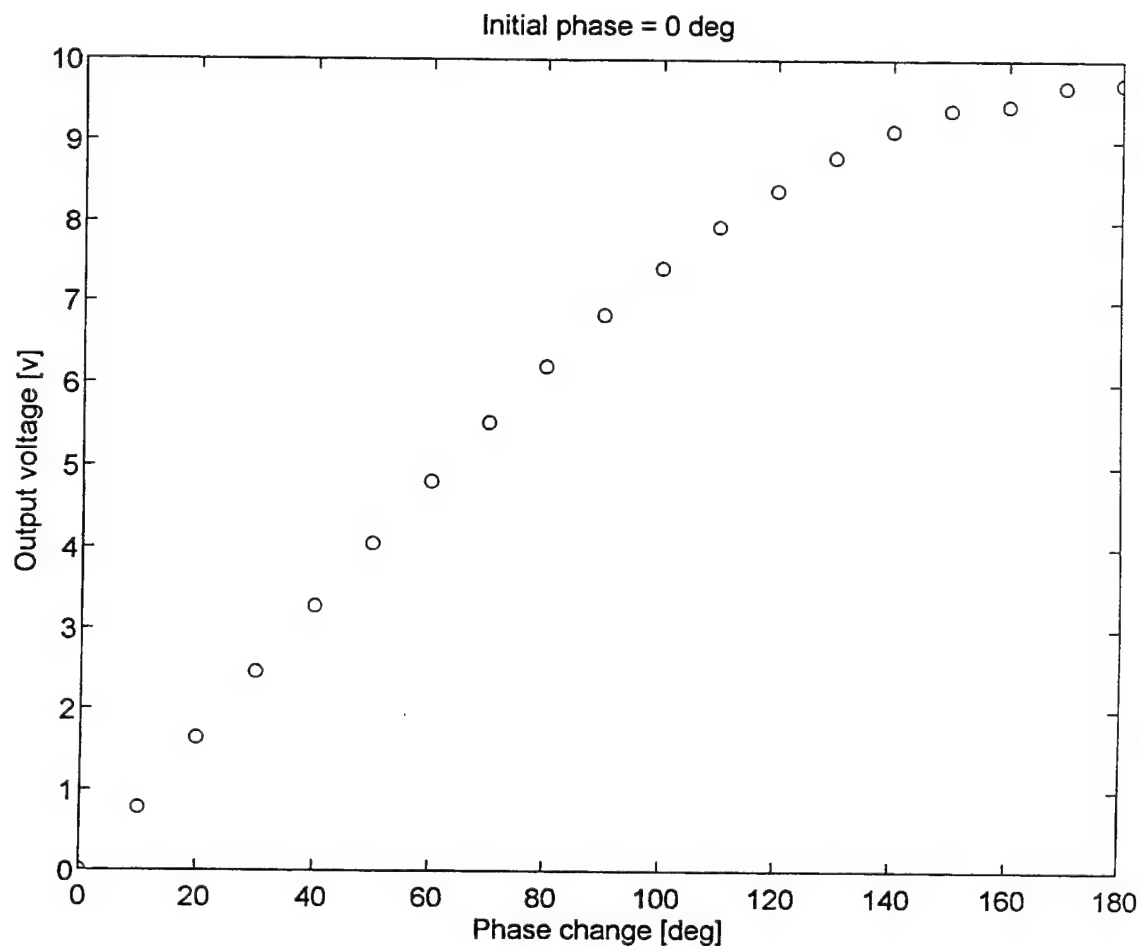


Figure 24 Output voltage vs change in phase.

Chapter 2: Enhancing the Sensor Performance

2.1 High Field Transverse Annealing System

A high field transverse annealing system was designed to improve the performance of Metglas wire based magnetic field sensors. The wire is straightened by applying heat at 392°C for relieving local stress, which enables the insertion of the wire (diameter of $125\text{ }\mu\text{m}$) into the fused silica hollow core tube (diameter of $140\text{ }\mu\text{m}$). Initially, the annealing field was applied to the wire gage transversely to rotate the magnetic momentum to its easy axis. After annealing, the Metglas wire was located in longitudinal direction to get the maximum magnetostriction. The schematic of the high field transverse system is given in Figure 25. The magnetic induction of $420\text{G}/3.1\text{A}$ can be generated by the flux generator. This magnitude is enough to rotate the direction of local magnetization. Any flux above 100G virtually gives the same magnetostriction for annealed Metglas wires. The annealing is done for 7200 sec at 392°C , which is slightly lower than the Curie temperature of Metglas wire (422°C) in order not to break or crystallize the material for each gage. The sensors fabricated in this quarter used transversely annealed Metglas wire.

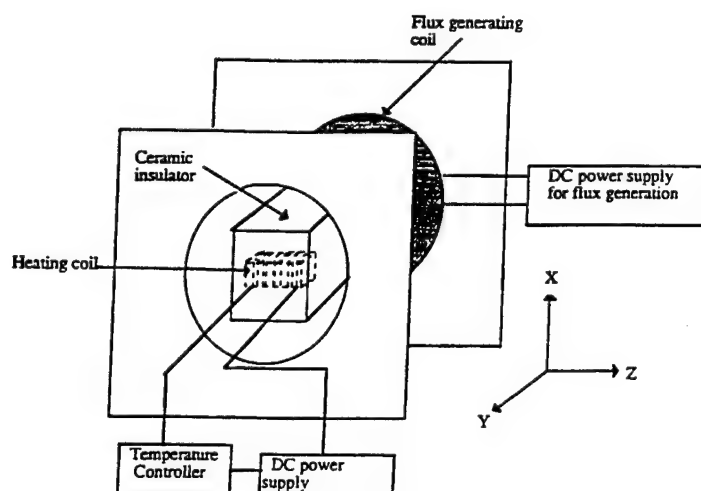


Figure 25 High field transverse annealing system for enhancing sensor performance.

2.2 Determination of CTEs of Sensor Materials

2.2.1 Heat Capacity of Sensor Materials

Temperature compensation is a crucial requirement in order to reduce the drift of Q-point in an EFPI sensor due to thermal fluctuation. There are several ways to do this using either active or passive compensation techniques. Active compensation requires complex electronic feedback circuit and another transducer for the compensation. The characteristics of the transducer itself is a function of temperature. Hence, the stable control of the Q-point in the sensor is complex and the resulting system is cumbersome. On the contrary, passive compensation is compact and stable in a certain temperature range. The range limitation is primarily due to the material property in both compensator and magnetostriction materials, and this limitation also exists in active compensation method. Hence, the passive compensation method is used for reduction of Q-point fluctuation of the sensor. The linear thermal expansion coefficient (CTE) and heat capacity (or specific heat) are parameters considered in design of temperature compensated sensor system. Hence, the heat capacity of each material has to be known at a given pressure for passive temperature compensation. Aluminum is used as a temperature compensation material. The specific heat of different materials considered for this task is shown in Table 5.

Table 5 Specific heat of candidate materials [2.1]

Materials	Atomic weight (g/g.mole)	Specific heat (cal/g.K)
Fe	55.847	0.106
B	10.1	0.245
Si	28.08	0.168
Al	26.981	0.215
Cr	51.996	0.115
Ni	58.69	0.106

The CTE of Metglas wire ($\text{Fe}_{77.5}\text{B}_{15}\text{Si}_{7.5}$) and Al are $8.7 \times 10^{-6}/\text{K}$ and $23.5 \times 10^{-6}/\text{K}$ respectively. At high temperatures, the heat capacity for a given volume of material becomes [2.1]

$$C_p = 3R = 6\text{cal/K.mole} \quad (2.1)$$

The heat capacity of metals approaches 6cal/K.mole around room temperature (300K). The specific heat is the amount of energy required to increase the temperature of a particular mass of material by one degree. The relationship between heat capacity and specific heat is given as

$$\text{Specific heat} = \text{Heat capacity} / \text{Atomic weight} \quad (2.2)$$

Hence, the calculated specific heat of Metglas wire based on mole fraction of each material component is 0.135 cal/g.K. The temperature compensation is passive; active schemes may not be needed to compensate the Q-point change due to ambient temperature drift. The heat capacity at a constant volume V is defined as

$$C_v = \frac{1}{N} \left(\frac{dQ}{dT} \right)_{V=\text{const}} \quad (2.3)$$

If N moles absorb a heat dQ when the temperature increases by dT , the heat capacity is given as above. The unit is $\text{J K}^{-1} \text{mole}^{-1}$ MKSC system of units or $\text{cal K}^{-1} \text{mole}^{-1}$ in traditional way. The heat capacity is also defined at constant pressure (C_p). All heat absorbed is as internal energy at constant volume. The heat capacity may be considered to be constant over a range of temperature. Heat is absorbed or rejected when the temperature changes from T_1 to T_2 using Eq. (2.3).

$$Q = NC(T_1 - T_2) \quad (2.4)$$

Hence, the heat capacity of each material has to be known, at a given pressure, for passive temperature compensation. The heat capacity of aluminum is $5.664 \text{ cal K}^{-1} \text{ mole}^{-1}$ at constant pressure. In order to achieve the same temperature change in Metglas and Al compensator, weight times specific heat for each material needs to be the same. Thus, the heat absorbed by each material is given as

$$Q_1 = M_1 C_{p1} \Delta T \quad (2.5)$$

$$Q_2 = M_2 C_{p2} \Delta T \quad (2.6)$$

If $M_1 C_{p1} = M_2 C_{p2}$, the temperature change will be same. Hence, the balance equation can be applied. The CTE of each material in an EFPI-sensor can be evaluated by the following model. After the CTE and heat capacity of each constituent of the sensor are established, the proper compensation scheme is developed as follows.

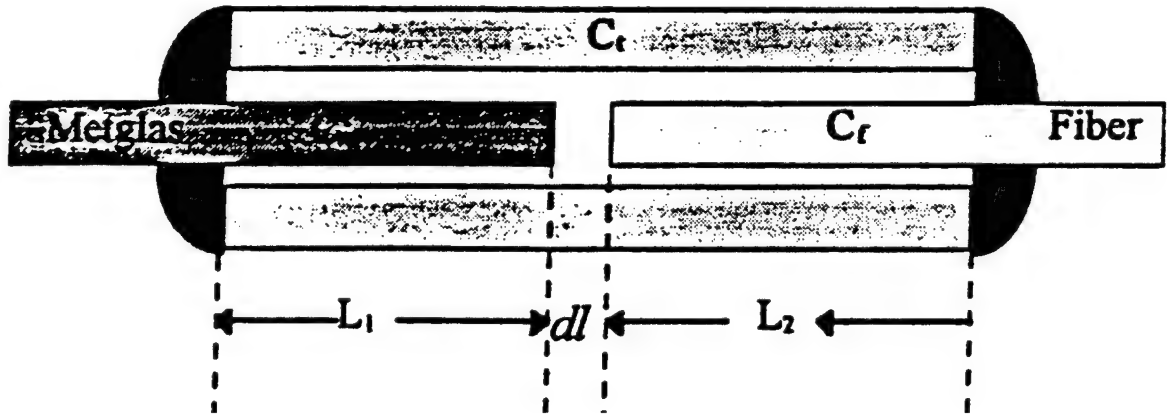


Figure 26 Temperature compensated weak magnetic field sensor.

2.2.2 Parameter Extraction Model

The air-gap change Δdl for the sensor geometry below is given as

$$\Delta dl / \Delta T = C_m L_1 + C_f L_2 - (L_1 + dl + L_2) C_t \quad (2.7)$$

C_m , C_f and C_t are the CTEs of Meglas wire, fiber and hollow core tube, respectively and ΔT is the temperature variation. The temperature compensation is achieved when Δdl is zero. Calculation of Δdl in an EFPI-based sensor is described below.

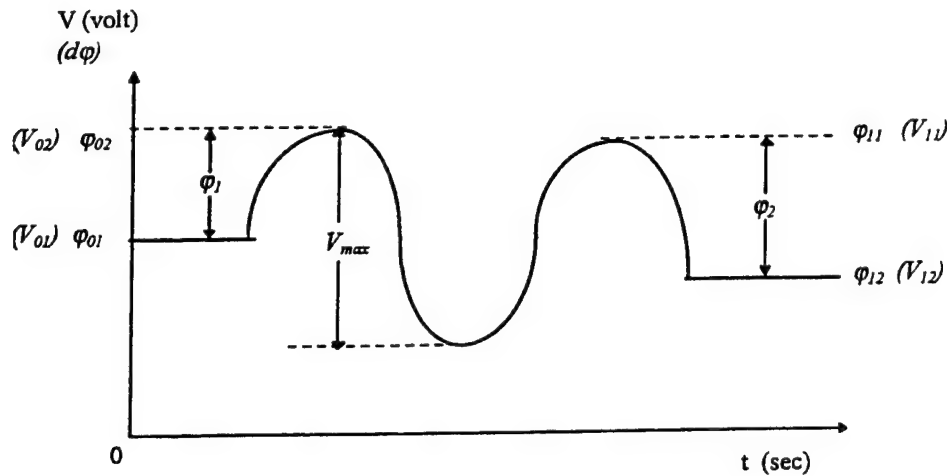


Figure 27 Calculation of air-gap change due to large measurand, using an EFPI-based sensor.

The phase extraction from the interferometric fringes involves not only counting the number of fringes, but also taking into account the leading and trailing incomplete fringes. Since $V = V_{max}(1 + \cos \varphi)/2$ as shown in Figure 2.7, the phase changes may be expressed as

$$\varphi_{0l} = \cos^{-1}(2V_{0l}/V_{max} - 1) \quad (2.8)$$

$$\varphi_{02} = \cos^{-1}(2V_{02}/V_{max} - 1) \quad (2.9)$$

and

$$\varphi_{II} = \cos^{-1}(2V_{II}/V_{max} - 1) \quad (2.10)$$

$$\varphi_{12} = \cos^{-1}(2V_{12}/V_{max} - 1) \quad (2.11)$$

Hence, $\varphi_1 = \varphi_{02} \cdot \varphi_{01}$ and $\varphi_2 = \varphi_{12} \cdot \varphi_{11}$. The air-gap change is given as $l = \varphi \lambda / 4\pi$. Thus, total air-gap change using Eqs. (2.8) through (2.11) is given as

$$\Delta dl = (\varphi_1 + \varphi_2 + 2\pi n) \lambda / 4\pi \quad (2.12)$$

where n is the number of full wavelength change in fringe. Hence, the change in measurand, ΔT , is calculated as

$$\Delta T = [(\varphi_1 + \varphi_2 + 2\pi n) \lambda / 4\pi] / [C_m L_1 + C_f L_2 - (L_1 + dl + L_2) C_t] \quad (2.13)$$

Each parameter such as CTE, gage or hollow core tube compensator/guider length can be determined by Eq. (2.13). The following is a comparison of measured and calculated value which is using Eq. (2.13). The measured values correlate well with theory.

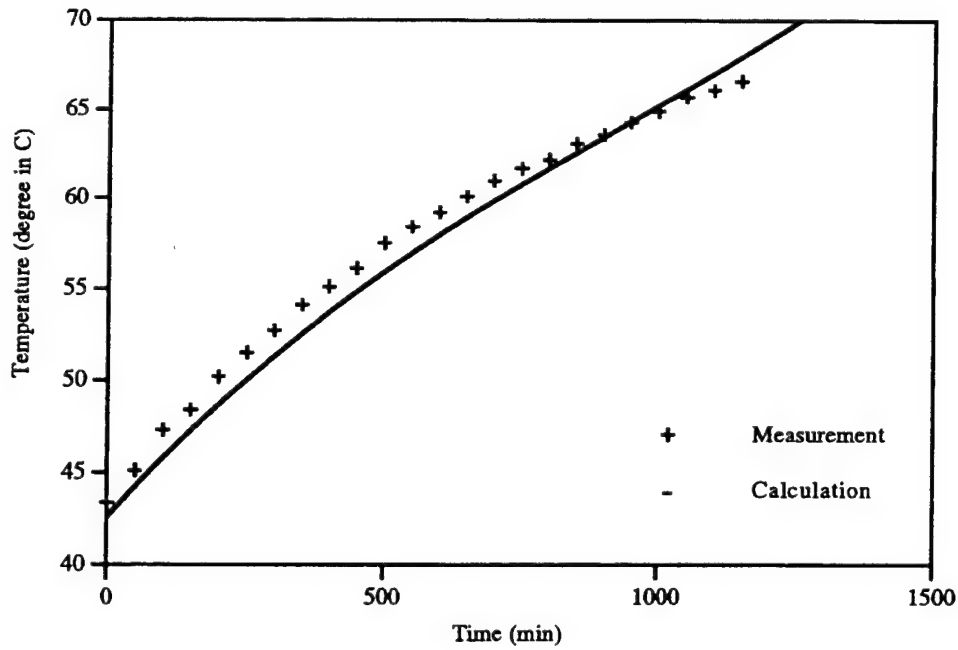


Figure 28 A model for extracting parameters.

The analysis uses the values of 2×10^{-2} m, $8.7 \times 10^{-6}/K$, $2 \times 10^{-6}/K$, 1300×10^{-9} m for sensor gage length, CTE of Metglas wire and hollow core tube, and wavelength respectively. Hence, at a given temperature, material parameters can be obtained by changing the gage length or hollow core tube length in each equation.

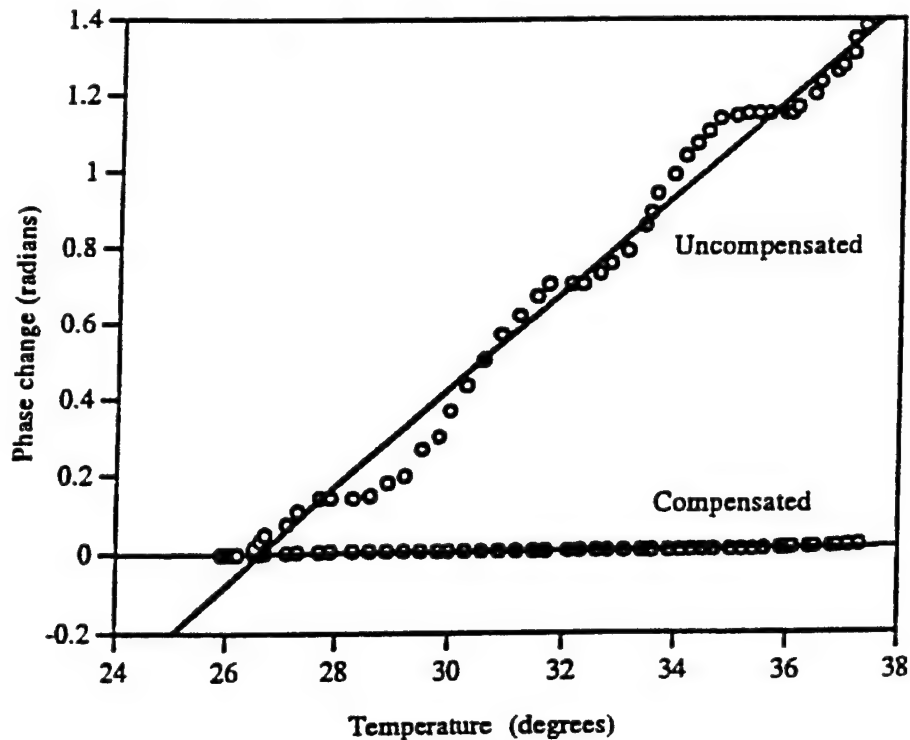


Figure 30. Effective passive temperature compensation in EFPI based weak magnetic field sensor.

2.3.2 Two Magnetostriction Materials and One Compensator with No Substrate Support

Sensor design that employs Metglas wire as the reflector is the best when the mechanical tolerance of each component is very tight. Moreover, in this scheme the specific heat is easily controllable in laboratory conditions by controlling the weight of temperature compensator/guider hollow core tube. The controlling mass depends on the density of the material and linear coefficient of thermal expansion of each material. Hence, passive temperature compensation is designed to increase the robustness in sensor operation using the facilities and materials that are available at the FEORC labs. The following design is used to reduce the asynchronous movement of compensators in quadrature phase shifted sensors. This is done by using one compensator for each quadrature sensor. A detailed construction is given in Figure 31.

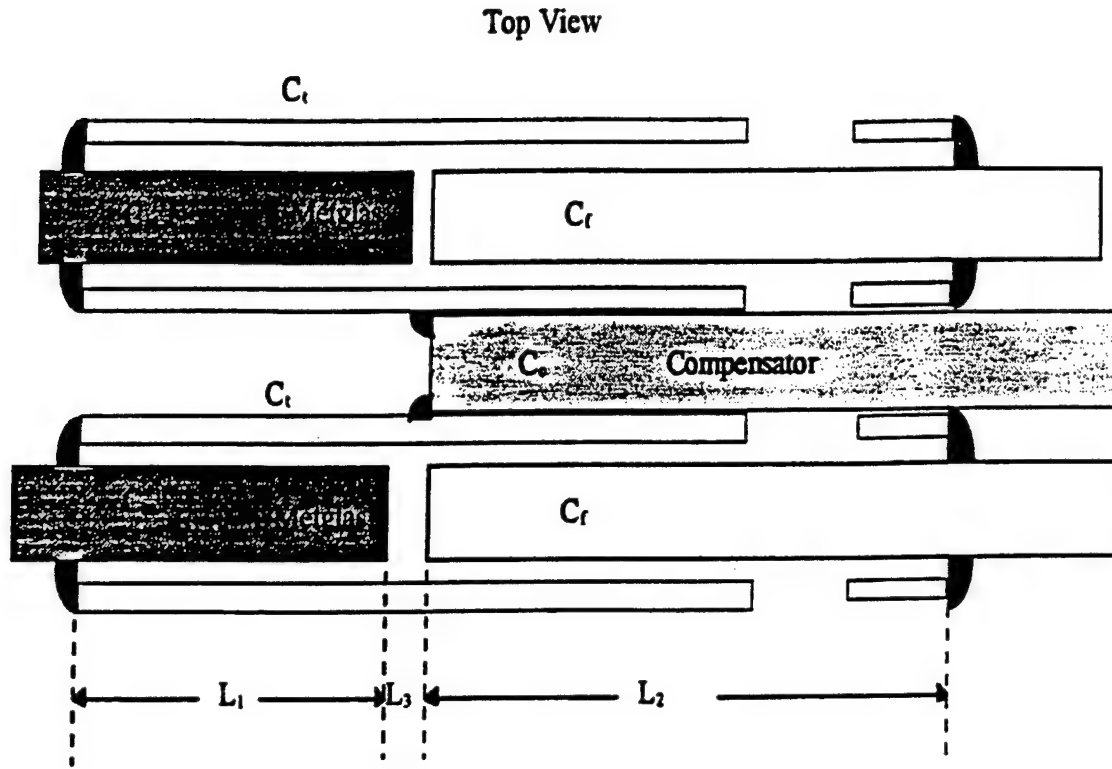


Figure 31 Passive temperature compensated EFPI magnetic field sensor with one compensator.

If the linear coefficient of thermal expansion of Metglas wire, fused silica hollow core tube, single mode fiber and the compensator are C_m , C_t , C_f and C_c , then the balancing equation for temperature compensation is given as follows

$$(C_m - C_t)L_1 = (C_c - C_f)L_2 + C_f L_3 \quad (2.14)$$

Since silica fused hollow core tube is used as the guide, $C_t = C_f$ and the last term of the right-hand side is negligible. Hence, a compact balance equation is obtainable. A stainless steel tube is used as a temperature compensator to increase the robustness of sensor operation. The calculated specific heat for each sensor construction material is given in Table 5.

The specific heat of austenitic (304 type) stainless steel ($\text{FeCr}_{18}\text{Ni}_8$) is calculated as 0.1084 cal/g.K and that of Metglas is 0.135 cal/g.K. Temperature rise in both materials is the same as the specific heat times mass of materials is set to be the same. The precise temperature compensation can thus be done based on this scheme. The quadrature phase shifted sensors are constructed based on this scheme. The magnetostriction calibration curve is given in Figure 32. The linear range of both sensors shows synchronous operation even when two magnetostrictive wires are used. The range of output voltage of these quadrature sensors are 0.1~40 mV for 100 ~ 40,000 nT with interference peak-to-peak voltage of 1 V. One of the advantages of this scheme is that there is no need to have a substrate to support the compensator.

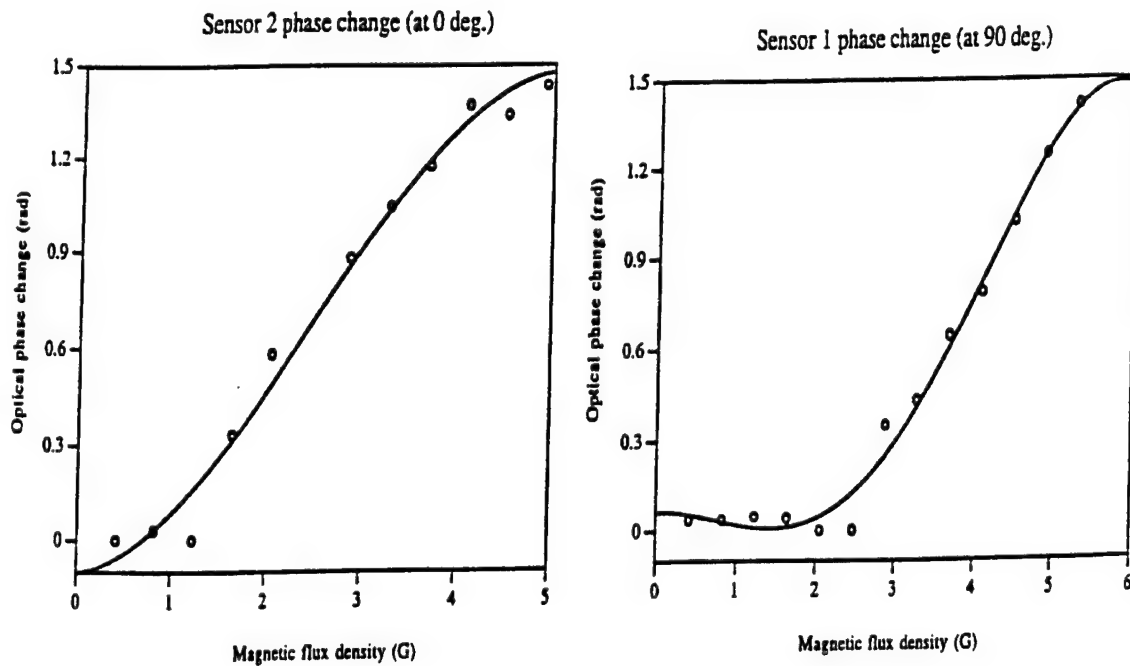


Figure 32 Response of dual sensor with one temperature compensator.

2.3.3 Quadrature Phase Shifted Sensor with One Magnetostrictive Element and Compensator

Even though the sensor with one compensator shows a good response, the mechanical tolerance requirements are very stringent. The diameters of Metglas and silica fiber, and hollow core tube are $125\ \mu\text{m}$ and $140\ \mu\text{m}$ respectively. Hence, the geometry is susceptible to misalignments. To reduce measurement inaccuracies due to misalignment, a novel sensor-compensator structure was designed and tested. This structure, shown in Figure 33, uses a single compensator for the two, quadrature phase-shifted, Metglas wire based EFPI sensors.

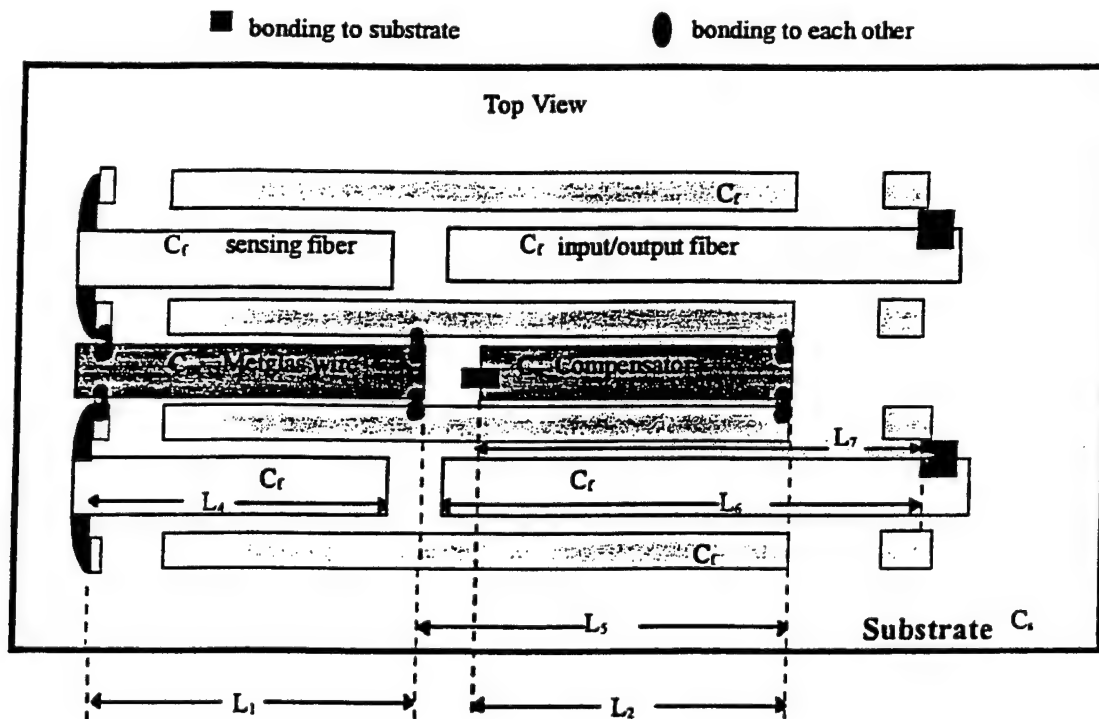


Figure 33 A quadrature phase shifted sensor design using pure EFPI sensors, one magnetostrictive element and one passive temperature compensator.

The temperature balancing equation for this sensor scheme is given as

$$C_m L_1 - C_f L_4 + C_f L_5 - C_c L_2 + C_s L_7 - C_f L_6 = 0 \quad (2.15)$$

The diameter of the fiber is 125 μm and that of the silica hollow core tube is 130 μm . The straightness of fiber arms and tight tolerance greatly enhances stable operation. The synchronous movements of EFPI reflector and sensing arms are ensured by single magnetostrictive element and temperature compensator. Since the Metglas wire extends beyond the hollow core tube, its absolute straightness is not required for linear response and the strong reflection from the Metglas reflector is avoidable by using low reflectance glass fiber reflector. The end face of the reflector fiber and input/output fiber can be easily maintained to be parallel using a fiber splicer. The response of the sensor was comparable to the single compensator sensor scheme.

2.4 Modified EFPI Sensors

2.4.1 Sensor Design with Side Wall Support

The sensor schemes discussed in previous sections are complex and hard to fabricate for practical applications. The design and manufacturing take a long time because of the required precision in dealing with extremely low disturbances such as 100 nT. Since the sensor operates within one half wavelength of the laser source (650 nm), small change of ambient temperature, laser source fluctuation, and external vibration cause instability of sensor output. It is crucial to minimize sensor dependence on mechanical tolerances for field conditions. This modified design is focused on reducing vibration sensitivity and improving minimum detectable flux density. The modified EFPI based sensor design is shown in Figure 34.

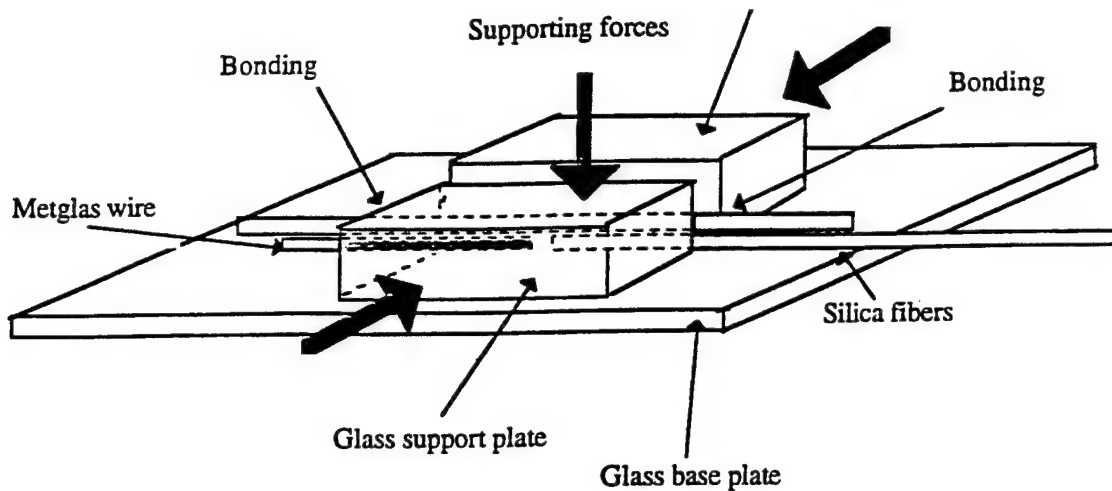


Figure 34 A modified EFPI based magnetic field sensor with side wall support.

Conventional EFPI sensors use the hollow core tube as a guide. Hence, tight mechanical tolerances are required for measuring axial strain. In an EFPI based sensor with $130\text{ }\mu\text{m}$ diameter hollow core tube guide and $125\text{ }\mu\text{m}$ diameter fiber/reflector, the tolerance is $5\text{ }\mu\text{m}$ which is very susceptible to external vibration so that the sensor only can be used as a vibration sensor which is not the intended application. For the magnetic field sensors being developed here, the straightness of the Metglas wire is not as perfect as a single mode fiber is, which makes it hard to insert in a more mechanically tight (smaller) hollow core silica tube, in spite of field annealing. The minimum diameter of the silica tube which can accept the $125\text{ }\mu\text{m}$ diameter of Metglas wire is $140\text{ }\mu\text{m}$ because of that reason. The stable operation is ensured, by placing the Metglas wire on a flat laboratory glass, to detect DC weak magnetic field. The fiber sensing arm is aligned to the Metglas wire by pushing the side glass plates. A fiber for preventing transverse movement in z-direction is inserted onto the Metglas wire and sensing fiber after both side walls are closed. The side wall also enhances the straightness of Metglas wire by forcing it not to bend in a random direction. Although forcing the gage produces some friction in its movement, prevention of bending in the gage well compensates the friction loss. Hence, the response in the linear operating range is actually enhanced. The maximum voltage output of the

interference term was 3.12 V and the corresponding phase change of 1 rad/G in the linear range (with gage length of 2.7 cm) as shown in Figure 35.

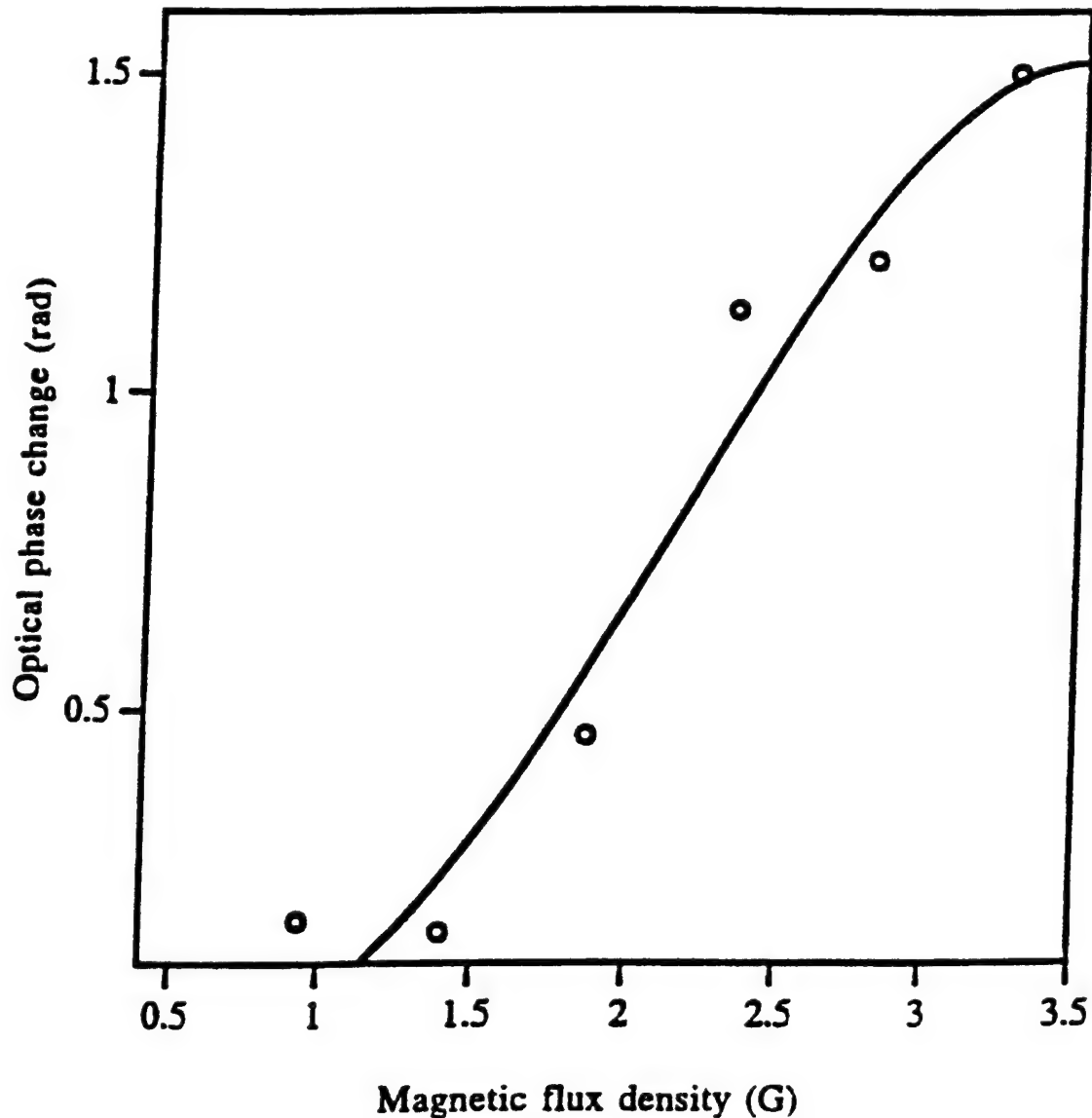


Figure 35 DC magnetic field response of a side wall supported magnetic field sensor.

The other sensor of the same scheme with gage length of 3.01 cm and DC bias at 1.5G shows 60 mV change when 100nT flux was exerted, (shown in Figure 36). This sensor scheme shows very low vibration sensitivity, as required for stable operation.

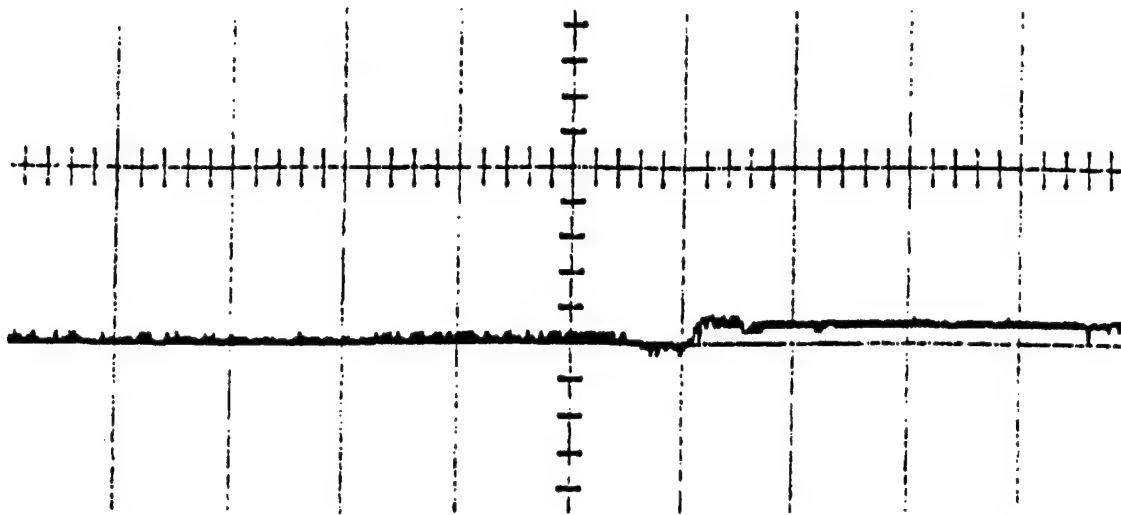


Figure 36. 100 nT DC magnetic field detection by the side-wall supported sensor without signal processing.

2.4.2 Vibration Insensitive Sensor Geometry

Although the side wall supported sensor has shown to be capable of detecting 100 nT without any signal processing, the sensor was not designed to do temperature compensation. Since the glass plate used has CTE of $0.5 \times 10^{-6}/\text{K}$, the base material is not suitable for temperature compensation. If the base material and side supporter with CTE value between that of Metglas and the silica fiber is used, the temperature compensation scheme is the same as the basic sensor discussed earlier and this scheme will show the best performance and stability. On the other hand, a sensor that can be easily made by using materials such as stainless steel tubes is designed to yield field detectability, low vibration sensitivity and reasonable temperature compensation. A sensor bearing the latter concept is shown in Figure 37.

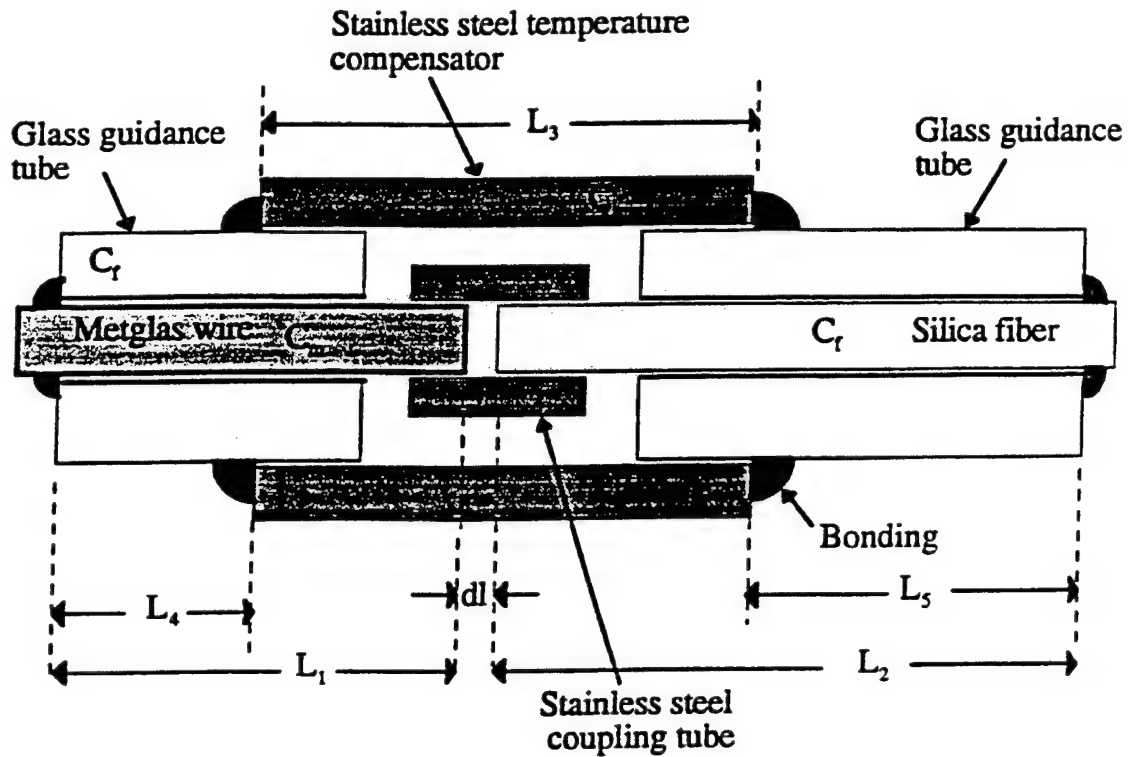


Figure 37 Weak magnetic field EFPI based sensor for stable operation.

The Metglas wire is gently inserted into the stainless steel tube. Since the stainless steel tube has diameter of 127 μm and the Metglas wire has 125 in diameter, there is only 2 μm gap between them. The sensing fiber is free to move inside of the guide because the fiber is almost perfectly straight. Thus, when an external magnetic field is applied to the sensor, the Metglas wire with guide expands freely and produces an optical path length change. A 130 μm hollow core fused silica tube is used for sensing fiber support, and a 140/250 μm hollow core fused silica tubes is used for supporting the Metglas wire. The temperature compensation equation is given as

$$(C_m - C_f)L_4 - (C_s - C_m)(L_1 - L_4) - (C_s - C_f)(L_2 - L_5) = 0 \quad (2.16)$$

and

$$L_3 + L_4 + L_5 = L_1 + L_2 \quad (2.17)$$

where C_m , C_f and C_s are CTE of Metglas wire, fiber and stainless steel compensator respectively. The output change due to temperature change of 10 °C results in one and quarter fringe in time domain which is equivalent of 0.8125 μm expansion for 3.5 cm sensor gage. The calculated expansion of uncompensated sensor is 3.045 μm in axial direction. The temperature compensation is 73.3 % which is relatively low compared to the prior result since heat capacity is not considered due to extreme difficulty in controlling individual masses. The output of sensor is shown in Figure 38.

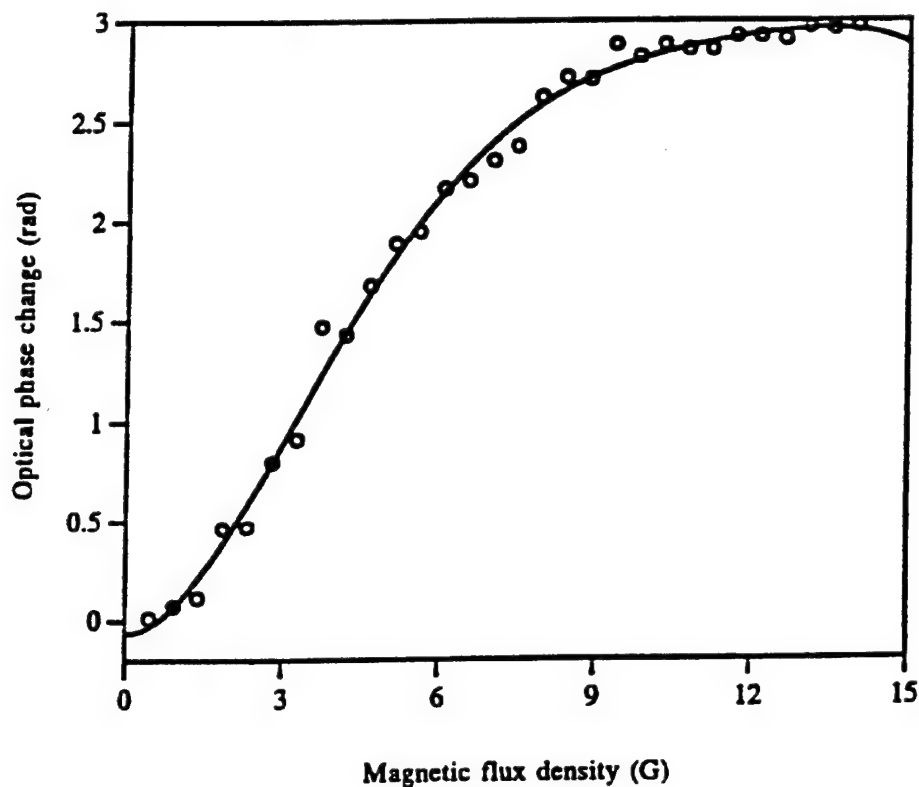


Figure 38 Response of the robust sensor for weak DC magnetic field detection.

The sensor shows 0.4 rad/1 G in the linear range which corresponds to 1.184 mV for V_{max} of 5.92 V. The response to DC 100 nT flux is shown in Figure 39. This signal shows 20 mV change by the flux density change. In order to increase the response the gain was increased in the detector output. The sensor is as insensitive to vibration as the side wall supported geometry.

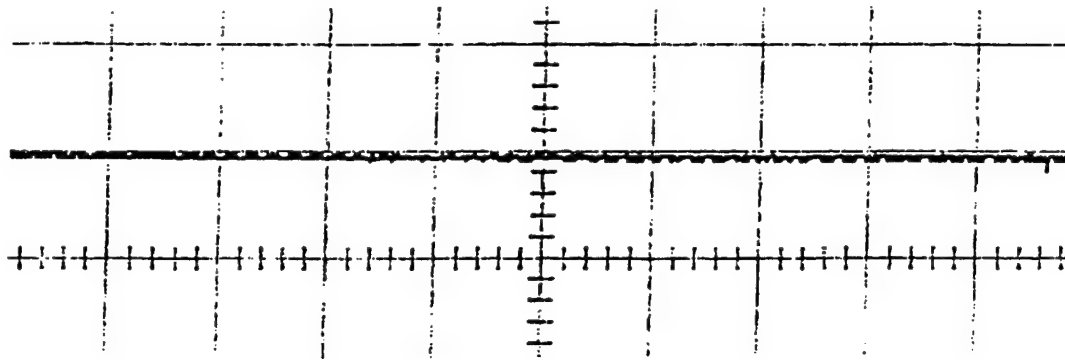


Figure 39 DC magnetic field (100 nT) detection by a robust EFPI based sensor.

2.4.3 Adjustable Sensor Geometry

Since the desired sensitivity of magnetic field measurement is 100 nT, system stability is essential to ensure low field measurement. The sensor system consists of the sensor gages, laser source box and signal demodulation box. The stability of the system is affected by different optical and electronic components of the boxes. System performance is mainly determined by the sensitivity of the sensor gage itself. If the sensitivity of the sensor gage to a 100 nT magnetic field is high enough to produce a signal output above system noise level, then the measuring capability is enhanced. The Metglas wire used for sensor gage has a saturation magnetostriction of 6~8 ppm and linear response of 0.8~1 ppm/G after the transverse field annealing. The optical phase change due to the imposed magnetic field is proportional to the length and linear response of sensor gage. Thus, there are two ways to increase the sensitivity. The first method is to increase the length of the gage, the other is to change the material composition of the Metglas wire such that it gives larger saturation magnetostriction and linear response. During this reporting period, increasing the length of the gage is used for enhancing the sensitivity. The length was increased from 2~3 cm to 4~6 cm (roughness of the wire ends and the straightness of the wire limit the use of longer lengths). Hence, the sensitivity was doubled with this method. Another way to increase the system sensitivity is to increase the fringe visibility of the sensors. The unnecessary large DC term in the

sensor output will be reduced by increasing the fringe visibility. The increase in fringe visibility is done by reducing the second reflection which is 11 times higher than first reflection, assuming the reflectance of the highly polished Metglas wire to be 0.5. This can be done by either increasing the air gap between the reflectors or coating the polished Metglas wire reflector with low reflectance material. The first method was avoided since the increase of air gap causes a misalignment of the in/output fibers and induces vibration sensitivity. For the electronics, the sensitivity is limited by the noise level of each component and the maximum allowable input level. The system uses linear ICs for the signal demodulation circuitry. The maximum allowable input value is 12V DC. Hence, the gain in the photo detector circuitry was adjusted to satisfy this requirement. A highly regulated power supply is used for the electronic parts. Temperature induced system output fluctuation are caused by air gap change and laser output variation. These sources of fluctuations should be well controlled in order to measure a low magnetic field. One of the major reasons for spurious outputs from the system was the temperature induced air gap change. A one half fringe change in the output of the sensor (a phase change of π rad.) is equivalent to $0.33 \mu\text{m}$ change in air gap, as given by

$$\varphi = nkL = nk2l = 1. \frac{2\pi}{\lambda} 2l \quad (2.18)$$

where λ is the operating wavelength which is $1.32\mu\text{m}$, L is the total optical path length change, l is the airgap change and n is the refractive index of the FP cavity (air=1). The expansion of Metglas due to temperature, for a 4 cm long wire is $0.348 \mu\text{m}/^\circ\text{C}$ as given by,

$$\Delta l_{0l} / \Delta T = CTE_{met} \times l_0 = 8.7 \times 10^{-6} \times 4 \times 10^{-2} \text{m} / ^\circ\text{C} = 0.348 \mu\text{m} / ^\circ\text{C} \quad (2.19)$$

For a 100 nT magnetic field, the Metglas wire expands $0.00004 \mu\text{m}$ as given by

$$\Delta l_{om} = \text{Magnetostrictivecoeff} \times |\vec{B}| \times l_0 = 1 \text{ ppm} / G \times 1 \text{ mG} \times 4 \times 10^{-2} \text{ m} = 0.00004 \mu\text{m} \quad (2.20)$$

This is 0.0115% of the length change induced by 1 °C change in temperature. Hence,, temperature compensation is crucial to achieve low magnetic field measurement. A suitable passive temperature compensation scheme was implemented using the fact that different materials have different coefficients of linear thermal expansion and different heat capacities. The goal is to achieve 99.99% temperature compensation for a certain range of temperature variation rate. These calculations are based on the assumption that the CTE of Metglas wire is 8.7 ppm/°C, linear expansion of the wire by magnetic field is 1ppm/G and sensor gage length is 4 cm long. Hence, in order to achieve 99.99% temperature compensation, the rate of length change due to temperature should be below 0.00004 μm/°C. The following sections describe the attempts to achieve the temperature compensation. In order to get good temperature compensation, fine adjustment of each parameter is essential. The geometry of an adjustable-compensator-length sensor is given in Figure 40.

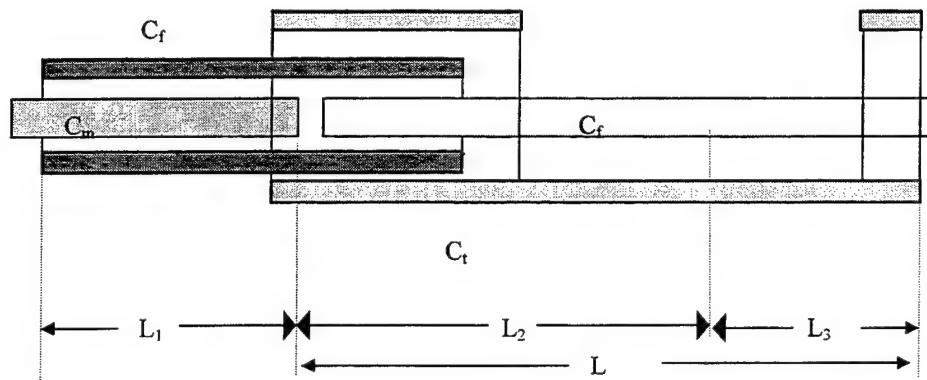


Figure 40 Adjustable sensor geometry for fine tuning the compensator length.

The balance equation for this configuration is given as

$$(C_m - C_f)L_1 - (L_2 + L_3)(C_t - C_f) = \Delta L / \Delta T \quad (2.21)$$

where ΔL is the number of fringes times one half wave length and L_2 is the exact length calculated to give 100% compensation. If the right-hand term is zero, 100% temperature compensation is achieved. This is simple in theory but in practice, a coefficient ($\Delta L / \Delta T$) of $0.00004 \mu\text{m}/^\circ\text{C}$ is extremely hard to achieve. Since the CTEs of the wire/tube like materials are slightly different from those of bulk materials, the adjustable geometry is necessary to provide flexibility in temperature compensation. After measuring the coefficient of the sensor experimentally, the adjustment for exact compensation length L_3 is done as

$$L_3 = \frac{(C_m - C_f)L_1 - \Delta L / \Delta T}{C_t - C_f} - L_2. \quad (2.22)$$

The aforementioned procedure is repeated till the optimal point is obtained. In order to enhance the sensor stability, a soldering method was used. The input fiber was partially coated with silver and the compensator used was brass. Hence, the input fiber and compensator could be soldered with each other. This gives a continuous adjustment of compensator length for optimal positioning. The major problem with this method is that, desoldering causes disturbance in the already fine tuned sensor such as shifting the operating point of the sensor from the quadrature point and also the maximum fringe visibility point. A DC bias field using Alnico magnet was used during the sensor fine tuning. Because of this problem with solder, epoxy was chosen for the same purpose. Since the exact point is already calculated, the first epoxying point is a little longer than the exact point. After evaluating the temperature compensation performance, the optimal point is recalculated using Eqs. (2.21) and (2.22). Then a small drop of epoxy is applied at a point bit closer to the newly calculated optimal point. The exact optimal point can Thus, be obtained without disturbing the fine tuning of the sensor. Stainless steel tube

was also used as the compensator for this type of sensor. Another scheme for temperature compensation involved the idea of using the same material as the compensator. A Metglas wire, which was longitudinally annealed, was used for compensation. The Metglas expansion in longitudinal direction of this wire is negligible as compared to the expansion of transverse annealed sensor gage since the rotation of magnetic domains of longitudinally annealed Metglas wire is minimized by the annealing. The sensor is positioned in the longitudinal direction and measures only the longitudinal component of the vector magnetic field. This concept gives some basic advantage over other schemes. The CTE and heat capacity are the same for both sensor gage and compensator. This gives instant temperature compensation and the compensation always works regardless of the variation of rate change of temperature. Other schemes do not provide exact compensation due to the variation of rate change of temperature. This is because the heat capacity and heat transfer ratio cannot be the same for both compensator and sensor gage. All the schemes discussed above showed good temperature compensation but the sensitivity to magnetic fields was not satisfactory as one end of the 140 μm guide hollow-core tube end was open. The expansion of a 4 cm long Metglas gage by 100 nT magnetic flux is only 0.00004 μm which is equivalent to an optical path length change of 0.00008 μm . A slight misalignment of fiber tips produces very low sensitivity. A macro scale bending due to one open end is also a significant factor in the reduction of the sensitivity. Hence, it was necessary to return to the original simple design with proper materials.

The best design should show both good magnetic field sensitivity and temperature compensation. By closing both ends of the sensor, a good sensitivity can be obtained. In order to do that, the CTE of compensator should be greater than CTE of fused silica fiber and smaller than that of Metglas wire as the length of the compensator will always be greater than that of Metglas gage. A borosilicate tube with CTE of 5.15 ppm/ $^{\circ}\text{C}$ was found and drawn to the dimension needed to fabricate the EFPI sensor gages using the FEORC fiber fabrication draw tower. The basic geometry is given in Figure 41.

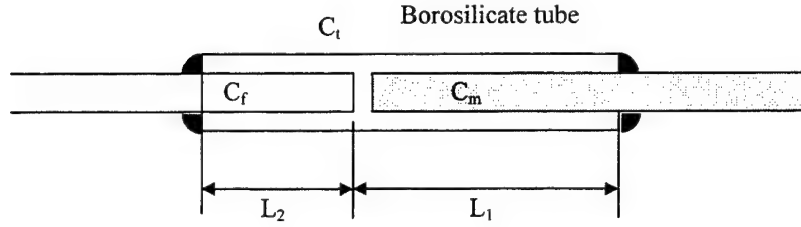


Figure 41 Simple sensor design with a borosilicate compensator.

The balance equation for this sensor geometry is given as

$$(C_m - C_f)L_1 - (C_t - C_f)L_2 - dl.C_t = \Delta L / \Delta T, \quad (2.23)$$

where $C_m > C_t > C_f$ and dl is the air gap between the fiber and Metglas wire. The compensator length is $L_1 + L_2$. For a given length of Metglas wire L_1 , L_2 is obtained by equating the left-hand side of Eq. (3.23) to zero. The exact value of CTE of each material that is C_f , C_m and C_t at a given temperature rate change is obtained by solving two simultaneous first order equations with two different lengths of Metglas wire or borosilicate compensator. The values obtained by this method were slightly different than the values given by the manufacturers. The CTE of Metglas was found to be 9.2 ppm/°C instead of 8.7 ppm/°C provided by the manufacturer and that of borosilicate was 6.24 ppm/°C instead of 5.15 ppm/°C. The slight change in the value can be explained as the effect of the field annealing and the fact that the geometry is different from that of bulk material. The newly evaluated value gives 96% compensation. By using old values of CTE provided by the manufacturer, the temperature compensation obtained is 83.75%. Hence, the proper evaluation of CTE of each component of sensor insures good temperature compensation.

2.5 System Performance Analysis

The effect of air gap change on the EFPI sensor due to external disturbance is very important, particularly in this case, because of the extreme sensitivity of the sensor. A simple analysis of this effect is presented so as to get an idea about the possible change in output due to large, external, physical disturbance.

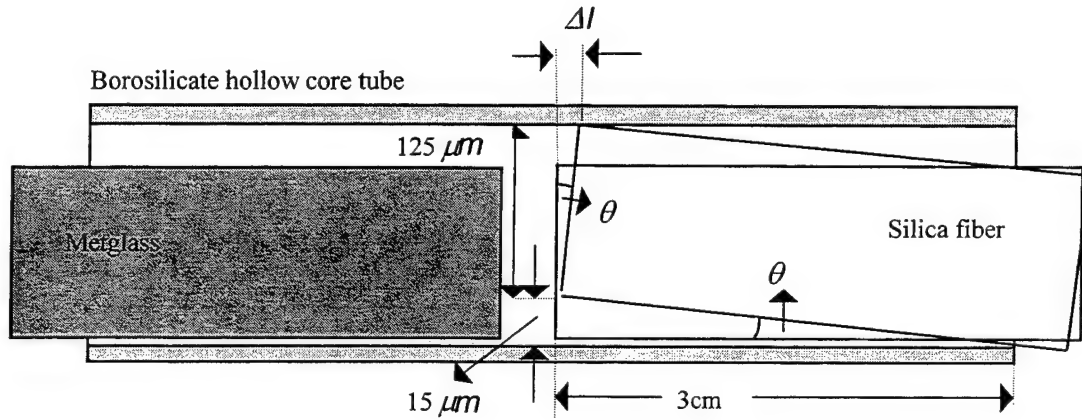


Figure 42 Effect of external disturbance.

For a hollow core guide tube of ID 140 μm and a silica glass fiber of OD 125 μm, the maximum possible shift is 15 μm as shown in Figure 42. Assuming a length of 3 cm, the maximum possible angular change, θ is

$$\theta = \tan^{-1}(15/30,000) = 0.0005 \text{ rad} \quad (2.24)$$

The change in the air gap, Δl , due to this angular change is

$$\Delta l = 125 \times 0.0005 = 0.0625 \mu\text{m} \quad (2.25)$$

The phase change of the output due to this air gap change is given as

$$\Delta\varphi = \frac{4\pi}{\lambda} \Delta l = 0.6 \text{ rad} \quad (2.26)$$

A similar phase change can be observed for the Metglas side. Thus, the total change in the output of the sensor is given by

$$\Delta V = -\frac{V_{max}}{2} \sin \varphi \cdot \Delta\varphi \cong -\frac{V_{max}}{2} \cdot \Delta\varphi = -\frac{V_{max}}{2} \cdot 2 \cdot 0.6 = -0.6 V_{max} \quad (2.27)$$

As can be seen from the analysis, the change in output is nearly 60% of the maximum fringe value, which is not desirable. Thus, reducing the tolerance between the fiber and the hollow core tube is not only desired but also imperative. A blue, optical adhesive was used for the sensors fabricated during this period. Since the adhesive cures to an extremely hard, glass-like consistency, the sensors made were very stable and the operating point returned to the original position after the external disturbance was removed. In order to provide a good support to the quadrature phase shifted sensors, the following design was developed. As shown in Figure 43, an aluminum block with two parallel V-grooves is used as the base on which the sensors are placed. The bases of the both sensors are attached to one end of the block. In order to prevent the movement of the free end of the sensors, the V-grooves are covered by a thin Aluminum sheet. The DC magnetic field required to bias the sensors is provided by the permanent magnet attached under the block.

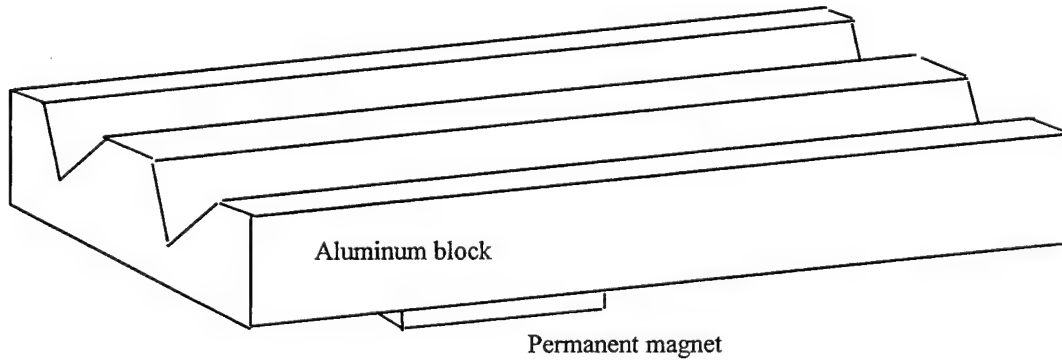


Figure 43 Design of mechanical support for the sensors.

2.5.1 Evaluation of Temperature Compensation Scheme

The temperature compensation scheme discussed earlier was implemented in all the sensors prepared so far. One of these sensors was used to extensively evaluate the compensation scheme. The output of this sensor is as shown in Figure 44. The temperature was increased from 22.9°C to 55.8°C and then reduced to 27.7°C. The length of the Metglas wire used was 3.7 cm.

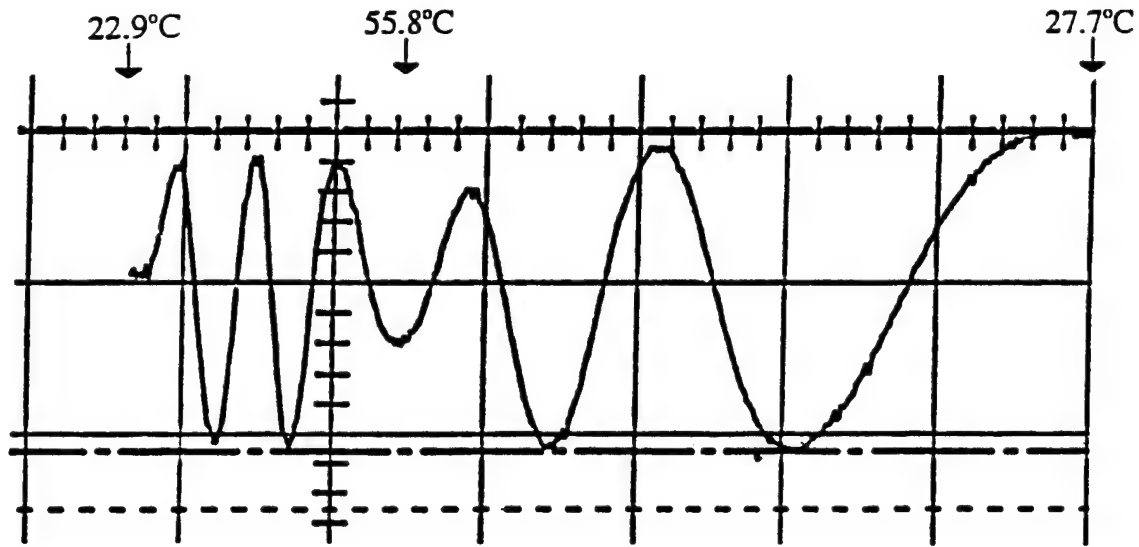


Figure 44 Evaluation of temperature compensation.

As can be seen from the Figure, 2.625 fringes were observed as the temperature increased to 55.8°C and 2.25 fringes were observed as the temperature decreased to 27.7°C. Thus, for a total temperature change of 61°C, the total number of fringes observed was 4.875. For a sensor with no temperature compensation, the change in air gap is

$$\Delta l_{wo} = CTE(\text{Metglas}) \times l_0 \times \Delta T = 8.7 \text{ ppm}/^\circ\text{C} \times 0.037\text{m} \times 61 = 19.636 \mu\text{m} \quad (2.28)$$

Where l_0 , is the length of the Metglas wire used. For the above sensor, with compensation, the change in air gap length is,

$$\Delta l_w = \# \text{ of fringes} \times \frac{\lambda}{2} = 3.19 \mu m. \quad (2.29)$$

Thus, the sensor is 83.75% thermally compensated.

2.5.2 Calculation of Exact CTEs of Metglas Wire and Compensator Tube

Due to the importance of a temperature compensated sensor, it's crucial to obtain the correct values of CTE for Metglas wire and Borosilicate tube, particularly after it is observed that the values provided by the manufacturer are not very accurate. Assuming the values provided by the manufacturer to be correct, it was calculated that with no compensation, a change in temperature of 0.046°C would cause a change in length of the Metglas wire comparable to that by a magnetic field of 40,000 nT. This is obtained as follows. The change in length of the Metglas wire due to an applied magnetic field of 40,000 nT (0.4 G) is given by

$$\Delta l_m = \text{magnetostrictive_sensitivity} \times |\vec{B}| \times l_0 = 1 \text{ ppm} / G \times 0.4 G \times l_0 \quad (2.30)$$

The change in length of the wire due to temperature change is given as

$$\Delta l_t = \text{CTE}_{\text{met}} \times \Delta T \times l_0 = 8.7 \text{ ppm} / ^\circ\text{C} \times \Delta T \times l_0 \quad (2.31)$$

where l_0 is the length of the Metglas wire. Equating the above equations, gives the temperature change which causes a length change equivalent to that by 40,000 nT magnetic flux. Thus, in order to overcome this problem, it is necessary to obtain a sensor with 99.98% thermal compensation. Hence,, obtaining exact CTEs is very critical for the proper operation of the sensor. The experimental setup for calculating CTEs, the observations and conclusions follow. As discussed earlier, for the sensor geometry shown in Figure 45, the length of the compensating element (borosilicate tube) depends on the length of the Metglas wire and the thermal compensation required.

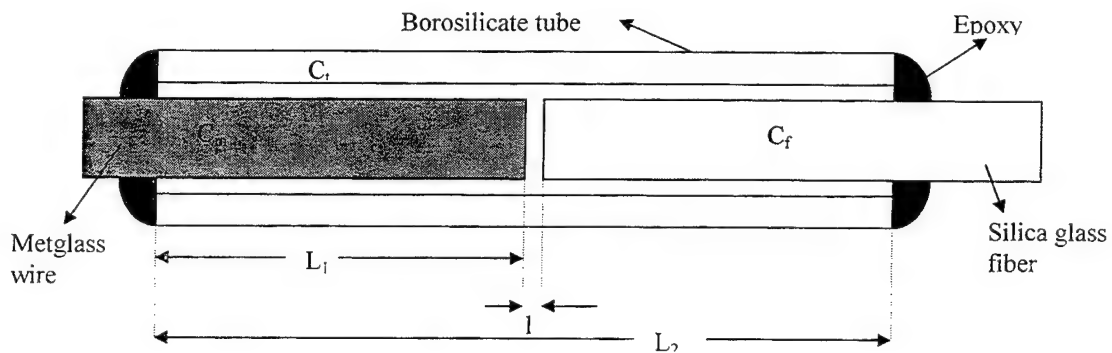


Figure 45 Simple sensor geometry with borosilicate tube as compensator.

The change in the air gap, Δl is given by the following equation

$$\Delta l / \Delta T = L_2(C_t - C_f) - L_1(C_m - C_f) \quad (2.32)$$

where L_1 is the length of the Metglas wire, L_2 is the length of the borosilicate tube, C_t , C_m and C_f are the CTEs of borosilicate, Metglas and silica respectively and ΔT is the change in temperature. For the experimental evaluation of the CTEs, two sensors were made each with similar Metglas wire lengths, but different lengths of borosilicate tubes. The length of Metglas wire used for both sensors was 4.3 cm but the lengths of the borosilicate tubes used were 7.6cm and 10.1cm respectively. Both the sensors were heated to about 55 °C and then cooled to room temperature. The output of both the sensors was recorded as the temperature dropped from 54.7 °C to 34.0 °C. Figures. 46 and 47 show the typical outputs of sensors for various degrees of thermal compensation.

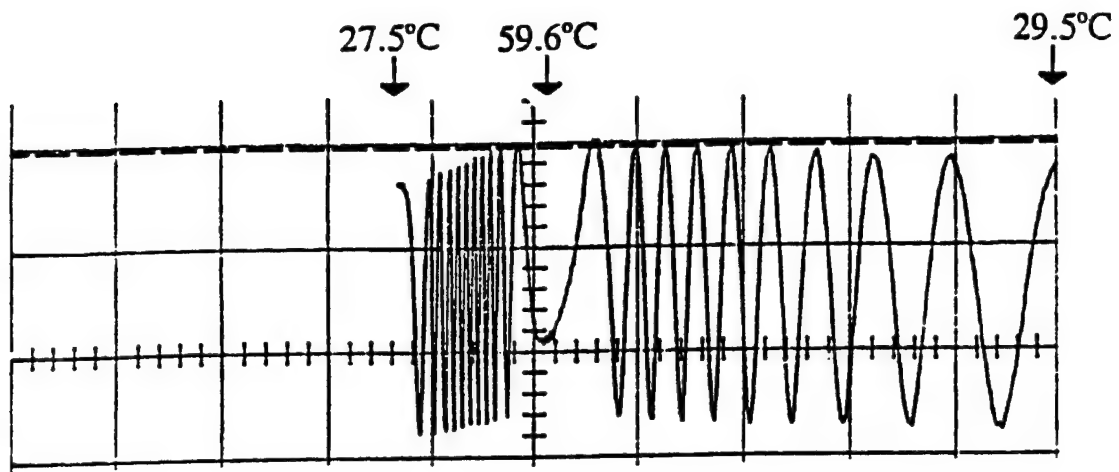


Figure 46 The output of the uncompensated sensor.

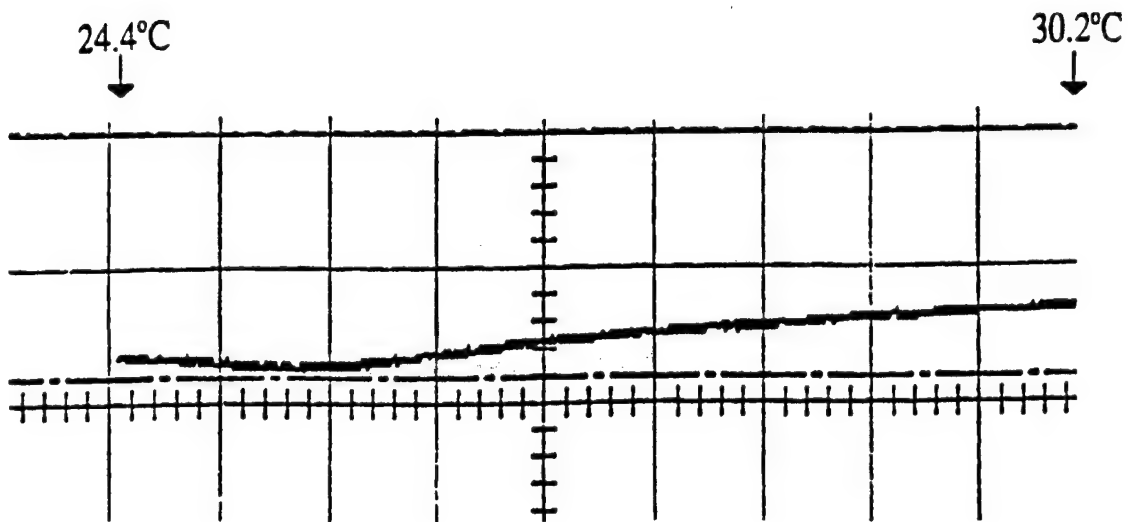


Figure 47 The output of the well compensated sensor.

The number of fringes in the output of each sensor can be used to calculate the change in the air gap length for that sensor. A single fringe corresponds to a one half wavelength

change in the air gap. Since the wavelength of the laser source used in the experiment is 1320 nm, one fringe corresponds to $0.66 \mu\text{m}$ change in the air gap. For the sensor with longer L_2 , 6.4 fringes were obtained and 1.9 fringes were obtained with the smaller sensor. Using this information the overall CTE $\times (\Delta l / \Delta T)$ of each sensor was calculated. Using Eq. (2.32) and the CTEs for the two sensors, two equations are obtained with two variables C_t and C_m . Solving these two gives the values of C_t and C_m . The CTE values for borosilicate and Metglas obtained from this experiment were $6.24 \times 10^{-6} / ^\circ\text{C}$ and $9.2 \times 10^{-6} / ^\circ\text{C}$ as compared to the values $5.15 \times 10^{-6} / ^\circ\text{C}$ and $8.7 \times 10^{-6} / ^\circ\text{C}$ provided by the manufacturers. A sensor was made using the new CTE values to obtain 100% thermal compensation. Figure 48 shows the output of the sensor for a temperature change from 25.5°C to 45.6°C . The thermal compensation of the sensor is 96%. The inaccuracies in the measurement of the exact lengths of the Metglas wire and borosilicate tube result in the compensation not being 100%.

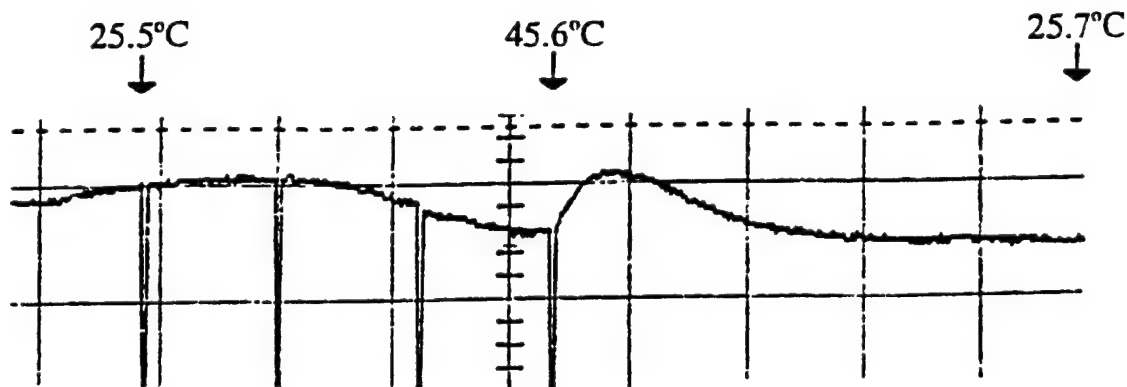


Figure 48 Output of the sensor compensated with new CTE values.

2.5.3 Signal Demodulation Circuitry

In order to measure the magnetic field accurately, the signal processing on the output of the two sensors has to be stable and with as low additional noise as possible. The block diagram of the signal demodulation circuitry for one-dimensional measurement of magnetic fields is as shown in Figure 49.

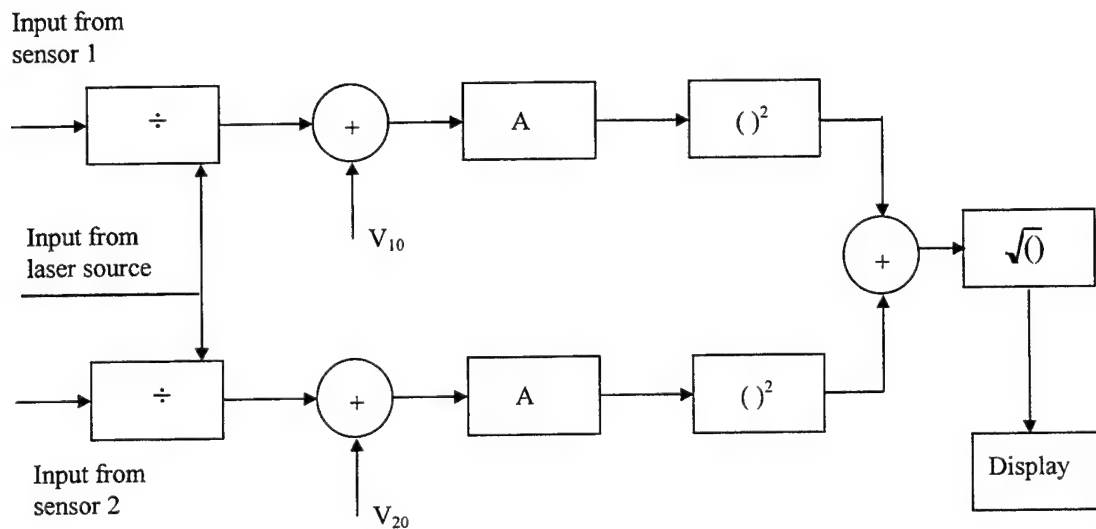


Figure 49 Block diagram of one-dimensional signal demodulation circuitry.

The output of each sensor and the output of the laser source form the three inputs to the demodulation box. At the first stage, the sensor outputs are normalized to account for the fluctuations in the laser output due to driver current and temperature. Then the initial values of each sensor output are subtracted from this normalized output to get a differentiated signal. The output of the differentiator only depends on the applied magnetic field. This value being small, it is amplified and squared. The outputs of the two quadrature phase shifted channels are then added. The square root of this signal is directly proportional to the applied magnetic field and is displayed as the output of the

demodulation box. Figure 50 shows the circuit diagram of the one-dimensional quadrature signal demodulation scheme.

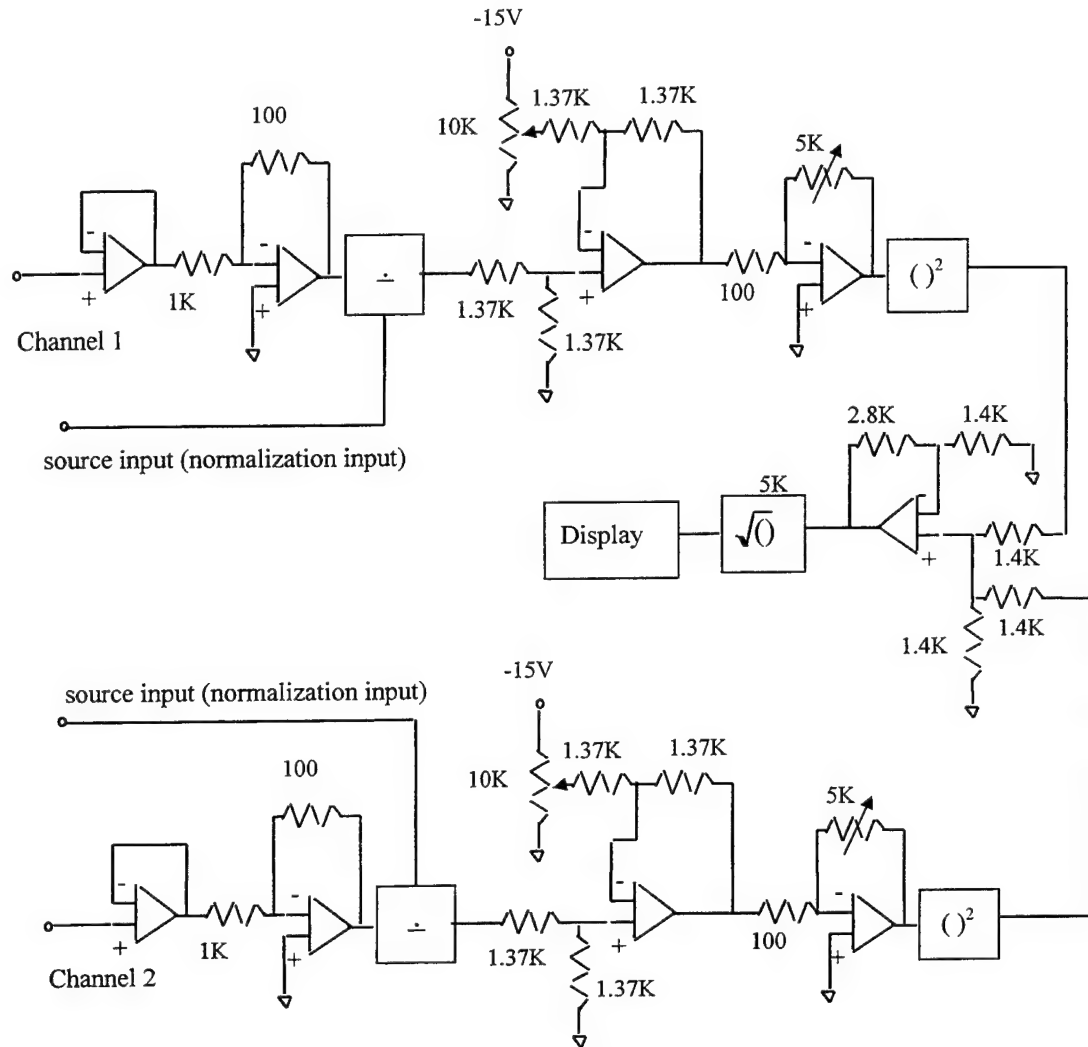


Figure 50 Circuit diagram of demodulation system.

The system response will be linear if the sensor is biased at the linear range of operating point. The system calibration curve gives the total response that includes original sensor output, gain term in photo detector, normalization circuitry gain and quadrature demodulation circuitry gain terms, and biasing. The optical phase change is a linear

function of air gap change. The air gap change is a linear function of expansion of Metglas sensor gage length. But the expansion of Metglas wire is a quadrature function of the applied magnetic field intensity, the magnetostriction ϵ can then be given as Eq. (1.5). Hence, for the gage biased at linear range and operating narrow measuring range the response is almost linear, but not linear. For this project the range of magnetic field to be measured is 1 mG to 0.4 G. This is a very small range. The response is almost linear with proper bias. This is shown in Figure 51.

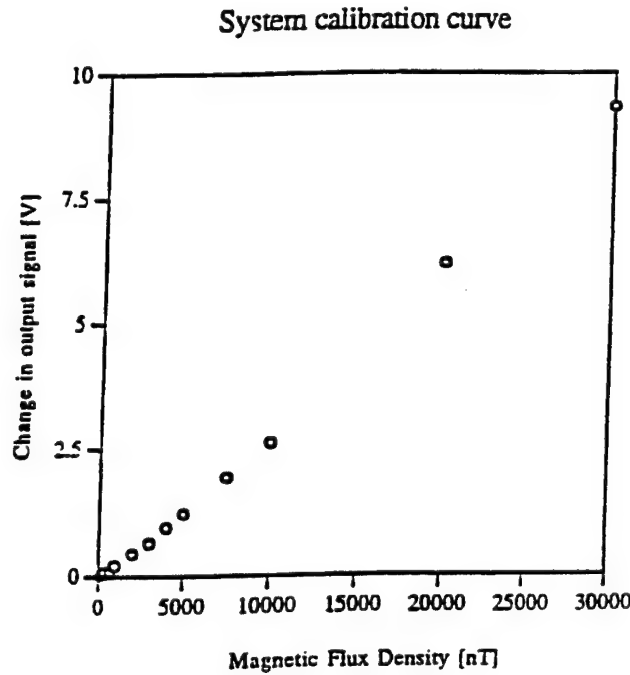


Figure 51 System calibration curve.

2.5.4 Factors Limiting System Performance

There are several factors that limit the lowest value of magnetic field detectable by the system. The output of an EFPI sensor is given by

$$I = I_1 + I_2 + 2\sqrt{I_1 I_2} \cos \varphi = I_1 + I_2 - 2\sqrt{I_1 I_2} + 2\sqrt{I_1 I_2} (1 + \cos \varphi), \quad (2.33)$$

where I_1 and I_2 are the intensities of the first and second reflections at the glass-air interface and φ is the phase difference between the two reflected waves. The first three terms represent the DC signal in the output while the last term represents the fringe signal. In order to get 100% fringe visibility, the two intensities are adjusted to be equal. Thus, Eq. (2.33) becomes

$$I = 2I_1(1 + \cos \varphi) \quad (2.34)$$

In terms of voltage, the sensor output is given as,

$$V = \frac{V_{pp}}{2}(1 + \cos \varphi), \quad (2.35)$$

where V_{pp} is the peak-to-peak value of the sensor output. From Eqs. (2.34) and (2.35) it can be seen that the output can be increased either by increasing the laser source power or by increasing the optical phase difference φ . The phase difference can be increased by decreasing the source wavelength or increasing the sensor gage length. Differentiating Eq. (2.35) gives

$$dV = -\frac{V_{pp}}{2} \sin \varphi . d\varphi = -\frac{V_{pp}}{2} d\varphi \quad (2.36)$$

since for quadrature point of operation $\varphi = 90^\circ$. The change in the optical phase difference between the two reflections is given as

$$d\varphi = 2nk \times e \times l_0, \quad (2.37)$$

where $k = 2\pi/\lambda$ and ε is the strain caused by the magnetic field on the sensor gage (given by Eq. (1.5)). Theoretically, the strain caused in the sensor gage is a quadrature function of the applied magnetic field. Using Eqs. (2.36), (2.37) and (1.5) we get,

$$\Delta V = -\frac{2\pi}{\lambda} V_{pp} \times C |\vec{H}|^2 \times l_0. \quad (2.38)$$

If the sensor gage is operated at a point on the linear range of the magnetostriction curve, by applying a biasing magnetic field H_b , the small voltage change in the output is proportional to the small change in the magnetic field. That is

$$d(\Delta V) = -\frac{4\pi}{\lambda} V_{pp} \times CH_b \times l_0 \times dH \quad (2.39)$$

The range of interest for this project is 1 mG to 0.4 G. This range is extremely small, so that Eq. (2.39) can be used with enough accuracy. The system performance can be evaluated in terms of signal-to-noise ratio (SNR), which is given as

$$SNR = 10 \log \frac{\text{signal_power}}{\text{noise_power}} = 20 \log \frac{\text{sensor_output}}{\text{thermal_fluctuation} + \text{laser_intensity_change} + \text{electronic_noise}} \text{ (dB)} \quad (2.40)$$

The following analysis shows how each factor affects the system sensitivity and how the sensitivity can be improved by improving each factor. For a 40,000 nT magnetic flux density, the system signal output was 9.49 V. The long term thermal fluctuation of the sensor was observed to be 4% of this value, 379 mV (as the sensor was 96% thermally compensated). Thus, the minimum measurable magnetic field, limited by thermal fluctuation of the sensor, is 1600 nT. For the system to detect 100 nT magnetic field, the thermal drift has to be less than 23.7 mV. That is, the thermal compensation of the sensor has to be more than 99.75%. The short-term variation in the laser output was observed to be about 65 mV/hr for an initial signal level of 0.52 V (12.46%). This corresponds to a magnetic field of 4984 nT. This fluctuation is due to the absence of an isolator at the output of the laser source. Thus, the dominant factor, after 96% thermal compensation, in the limitation of system sensitivity is laser source instability due to back reflection and thermal drift. The electronic short-term noise in the demodulation box for a fixed gain of 10, was observed to be 42 mV which is 0.44% of the signal output for 40,000 nT and corresponds to a magnetic field of 176 nT. This noise can be further reduced to a level

where the corresponding minimum detectable field limited by it is far below 100 nT. Thus, the SNR for the current system, for a 40,000 nT magnetic field is

$$SNR = 20 \log \frac{9.49}{0.379+1.18+0.042} = 15.44 \text{ dB} \quad (2.41)$$

The dominant factor is thus long-term and short-term laser output change. Therefore, reduction in the temperature drift and laser source fluctuations are essential to increase the SNR above 0 dB for a 100 nT magnetic field.

2.5.5 Improving System Performance

The system developed up to this point is limited by laser source fluctuation and thermal drift of sensor. For measuring magnetic flux density of 100 nT, the sensor output signal should be greater than the electronic noise, which is about 42 mV. Each noise component that limits the lowest measurable value of magnetic field is

$$\begin{aligned} V_{noise} &= V_{temp} + V_{laser} + V_{electronic} \\ &= (0.04 + 0.1246) V_{signal} + 0.042 \text{ volts} \\ &= 0.1646 V_{signal} + 0.042 \text{ volts} \end{aligned} \quad (2.42)$$

This value is equivalent to a magnetic field of 6760 nT. This is the lowest measurable magnetic field in an hour. If the measurement duration is reduced to 6 minutes, the V_{laser} term is reduced to $0.01246 V_{signal}$ and V_{noise} becomes $(0.05246 V_{signal} + 0.042)$ volts. The lowest measurable value is now 2275 nT. Thus, for very short duration, a magnetic field as low as 700 nT was measured using the current system. In order to measure a 100 nT field, the total noise signal in the output should be less than $0.0025 V_{signal}$. Thus, it is necessary to reduce all the noise components substantially in order to get the required resolution. In order to get an SNR of at least 6 dB at 100 nT magnetic field, the output of the sensor should be above 124 mV. Thus, the sensor output has to be increased 5.25 times from the current 23.7 mV. Increasing the gage length using a material with a higher

magnetostrictive coefficient, or a combination of both can do this. The other method would be to increase the laser output power 4~6 times. This increases the SNR (at 100 nT) to 4.33~6.75 dB. The combination of both gives a 10.33 to 12.75 dB increase in SNR. A DC bias above 1.5 G is enough to assure a linear response of the system. By using very small magnets to obtain this bias, the field outside the sensors can be reduced and using very small magnets to obtain this bias will minimize the ambient magnetic field distortion.

Chapter 3: Design of High Sensitivity Magnetic Field Sensors

3.1 Designing Passive Temperature Compensated Sensor

The accurate evaluation of CTE of each material in the sensor gage is essential to achieve proper temperature compensation. A systematic way is to introduce and solve simultaneous equations based on temperature balance equation given by the specific sensor geometry. Figure 52 shows the sensor geometry.

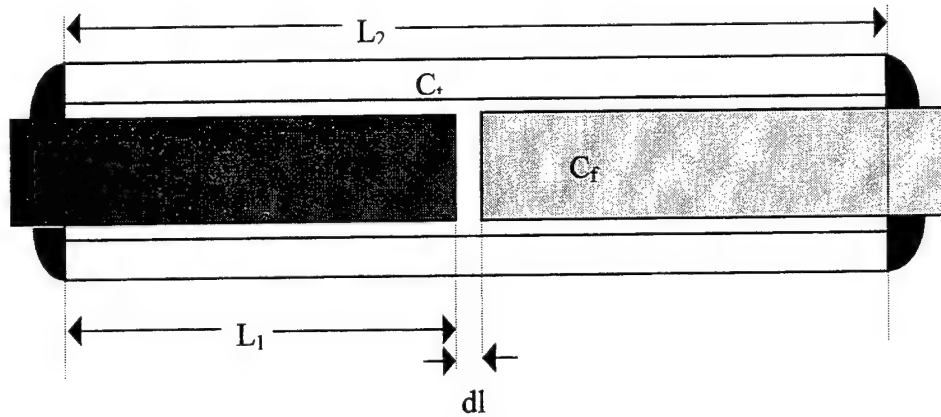


Figure 52 A robust temperature compensated sensor.

The small air gap dl is about $6.6 \mu\text{m}$ (adjusted by moving the fiber ends apart, till 10 fringes are obtained). This is negligible as compared to the gage and compensator lengths. C_m , C_t and C_f are the CTEs of Metglas, compensator tube and fiber respectively. The temperature balance equation for the above sensor geometry is given by,

$$(C_m - C_t)L_1 - (C_t - C_f)L_2 = \Delta L / \Delta T \quad (3.1)$$

Where ΔL is the air gap change induced by temperature variation and ΔT is the temperature change that induces the air gap change. These parameters are measured using an oscilloscope

and a temperature controller. When the term $\Delta L / \Delta T = 0$, the temperature compensation is 100 %. If materials with known CTEs and exact lengths are chosen, then 100 % temperature compensation can be easily achieved. Let $C_m = x$ and $C_t = y$. Two sensors are fabricated with the geometry as shown in Figure 52 and with different gage ($L_1 \rightarrow a$) and compensator ($L_2 \rightarrow b$) lengths. Hence, Eq. (3.1) can be rewritten as

$$(x - C_f)a - (y - C_f)b = \Delta L / \Delta T \quad (3.2)$$

Hence, for the two different sensors, the equations become

$$a_1x - b_1y = \Delta L_1 / \Delta T_1 - (b_1 - a_1)C_f \quad (3.3)$$

$$a_2x - b_2y = \Delta L_2 / \Delta T_2 - (b_2 - a_2)C_f \quad (3.4)$$

These can be written in matrix form as follows,

$$\begin{bmatrix} a_1 & -b_1 \\ a_2 & -b_2 \end{bmatrix} \begin{bmatrix} C_m \\ C_t \end{bmatrix} = \begin{bmatrix} \Delta L_1 / \Delta T_1 - (b_1 - a_1)C_f \\ \Delta L_2 / \Delta T_2 - (b_2 - a_2)C_f \end{bmatrix} \quad (3.5)$$

Eq. (3.5) is a linear equation of the form $AX = B$. Since the matrix A is non-singular (all the components have different lengths), the equation has a unique solution when solved for C_m and C_t . Here it is assumed that C_f is $0.5 \times 10^{-6} / \text{K}$. The CTE values of each material were evaluated using this method. $\Delta L / \Delta T$ is measured as,

$$\frac{\Delta L}{\Delta T} = \frac{\lambda}{2} \cdot \frac{\text{Number_of_Fringes_in_time_domain}}{\text{Temperature_variation}} \quad (3.6)$$

The method described above can be used for any linear system.

3.2 Enhancing the Sensor Gage Sensitivity

In order to measure fields of the order of 100 nT, the sensor material has to have a high sensitivity. A new material from UNITIKA Co. in Japan was a good candidate. Table 6 shows the properties of the new material after transverse field annealing and measurement of the CTE value using the method described above.

Table 6 Properties of new Metglas material

Parameter	Evaluated*	Nominal**
Saturation Magnetostriction	27×10^{-6}	35×10^{-6}
CTE	$6.305 \times 10^{-6} / \text{K}$	$8.7 \times 10^{-6} / \text{K}$
Curie temperature	-	437 °C
Crystallization temperature	-	530 °C
Composition	$\text{Fe}_{77.5}\text{Si}_{7.5}\text{B}_{15}$	
Commercial name	UNITIKA AF-10	
Geometry	125 μm diameter wire	

* Measured and evaluated for specific sensor geometry.

** Nominal values provided by the manufacturer.

Another method to increase sensitivity is to use longer sensor gage length. The gage length could be made as large as 12 cm by using a two-stage annealing process. But for the stable operation of the sensor and accurate temperature compensation, a sensor gage length of 4~5 cm is optimal. Hence, a gage length of 4~5 cm is used for fabricating sensors using the new material. Thus, the total sensor length including the compensator tube is about 6~7.5 cm. The magnetostrictive material, previously used for measuring weak magnetic fields ($\text{Fe}_{77.5}\text{B}_{15}\text{Si}_{7.5}$) shows a saturation magnetostriction of 6~8 ppm and a linear response of 0.8~1 ppm/G after transverse field annealing. The expansion of Metglas due to temperature, for a 4 cm long wire is $0.348 \mu\text{m}/^\circ\text{C}$ as calculated from the given nominal CTE of 8.7×10^{-6} ppm/K. For a field of 100 nT, the expansion of Metglas wire is $0.00004 \mu\text{m}$ as calculated from the magnetostrictive coefficient of

1 ppm/G. This is 0.00115 % of the length change induced by 1⁰C change in temperature. Hence, temperature compensation is very critical to be able to measure very low magnetic fields.

The phase change in the output, for a 100 nT magnetic field is 0.38 mrad as calculated from the expansion of wire for that field. The voltage output corresponding to this change is,

$$\Delta V = \frac{d}{d\phi} \left[\frac{V_{max}}{2} (1 + \cos \phi) \right] = -\frac{V_{max}}{2} \sin \phi \cdot d\phi = -\frac{V_{max}}{2} d\phi \quad (3.7)$$

where it is assumed that the sensor operates at the Q-point ($\sin \phi = 1$). With a V_{max} of 10V and demodulation circuitry gain of 20, the output voltage corresponding to 100 nT is 38 mV. The temperature fluctuation and electronic noise should be minimized below this level.

One way to increase system performance is to increase the sensitivity. A new sensor material was acquired and investigated as follows. The material is an amorphous form of Iron-Boron-Silicon. The composition of the glassy metal is $\text{Fe}_{77.5}\text{B}_{7.5}\text{Si}_{15}$. The saturation magnetostriction is 27 ppm after transverse field annealing. Figure 53 shows the magnetostrictive characteristics of the new material.

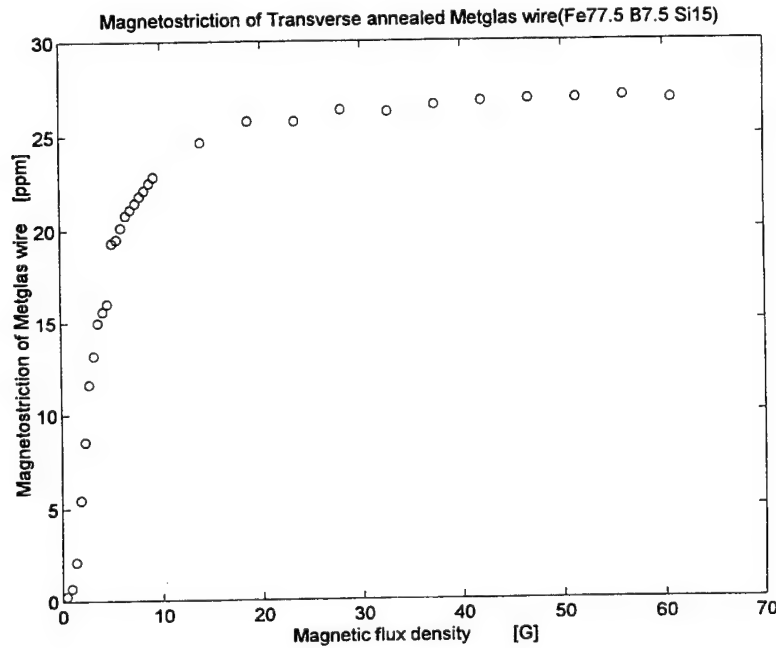


Figure 53 Magnetostriction of new material.

The linear response was 5 ppm/G. This is 5 times that of the old material. The phase change of the output for the saturation magnetic field of 10 G was 14.1 rad (or 2.25 fringes), for a 4 cm long wire. Hence, a 100 nT magnetic field is calculated to produce a 3.5 mrad phase change, which is 9 times the old material. For the same gains, the output voltage is now 342 mV for a 100 nT field.

3.3 Mathematical Adjustment for Temperature Compensation

The sensors currently being used have a temperature compensation of 96%. For 100 nT field detection, 99.99% compensation is required. The sensor geometry shown in Figure 54.

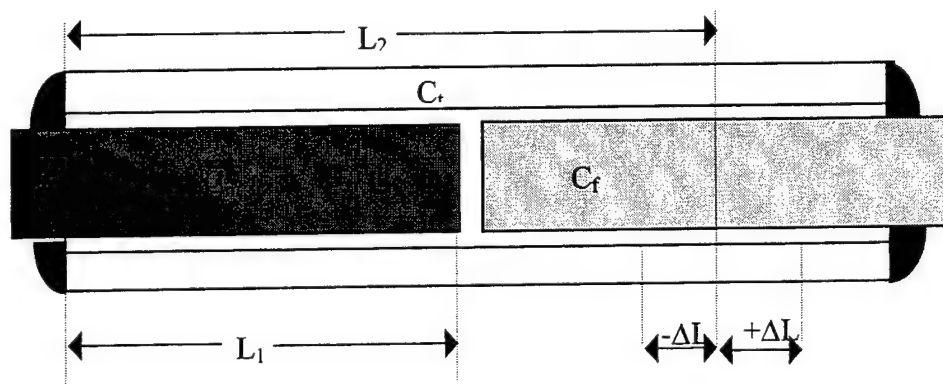


Figure 54 Sensor geometry to obtain exact temperature compensation by calculating ΔL .

The balance equation is given as,

$$(C_m - C_p)L_1 - (C_r - C_p)L_2 = \pm (\Delta L / \Delta T), \quad (3.8)$$

where C_m , C_f and C_t are the CTEs of Metglas, silica fiber and compensator tube (Borosilicate glass) respectively. Let

$$L_{exact} = L_2 \pm \Delta L \quad (3.9)$$

When the compensator length is L_{exact} , the RHS term of Eq. (3.8) is zero. Combining Eq. (3.8) and (3.9), we get,

$$(C_m - C_f)L_1 - (C_t - C_f)(L_2 \pm \Delta L) = 0 \quad (3.10)$$

Using Eq. (3.8) and (3.10),

$$\pm \Delta L / \Delta T = \pm (C_t - C_f) \Delta L \quad (3.11)$$

Thus, the adjustment ΔL for exact temperature compensation is given as

$$\Delta L = (\Delta L / \Delta T) / (C_t - C_f) \quad (3.12)$$

where the sign of ΔL follows that of Eq. (3.8). Eq. (3.8) can also be used to evaluate the CTE values systematically as follows. Let the compensator length, $L_2 = b_i$, Metglas wire length, $L_1 = a_i$, $C_m = x$ and $C_t = y$. Let $i = 1, 2$ for two different sensors. From Eq. (3.8),

$$a_1x - b_1y = \Delta L / \Delta T|_1 - (b_1 - a_1)C_f \quad (3.13)$$

$$a_2x - b_2y = \Delta L / \Delta T|_2 - (b_2 - a_2)C_f \quad (3.14)$$

These equations are of the matrix form, $AX=B$. If A is non-singular, then the above matrix equation has a unique solution. Thus, C_m and C_t can be obtained simultaneously. Here, C_f is assumed to be $0.5 \times 10^{-6} / K$. The CTE evaluation was repeated 6 times and then the statistical

average of the values was obtained as, $C_m = 6.17 \times 10^{-6}/K$ and $C_t = 4.83 \times 10^{-6}/K$. Evaluation of $\Delta l/\Delta T$ was done for various combinations of Metglas/ Borosilicate tubes.

Table 7 CTE values from various combinations.

Sensor/Compensator gage/tube	C_m ($\times 10^{-6}/K$)	C_t ($\times 10^{-6}/K$)	Reference
Metglas/Borosilicate	6.17	4.83	Average of 4 exps., eqs. (7), (8)
Metglas/Fused silica	11.04	0.5	Tube: ID:150 μm , OD:290 μm
Fiber/Borosilicate	-	4.59	Tube: ID:150 μm , OD:290 μm

As can be seen from the table, the CTE value of Metglas varies by nearly 100%. This is due to the heat capacity difference between the two compensator tubes. The heat capacity of each material above depends on the weight and specific heat. Hence, the heavier and longer tube takes more time to absorb heat and so more time to expand. Thus, the CTEs evaluated above can be regarded as “effective CTE” for that particular case. The CTE value of Borosilicate shows consistency because it is exposed to ambient temperature directly. Temperature compensation using these CTE values was 83.07%. Figure 55 shows the output of a sensor compensated using these values.

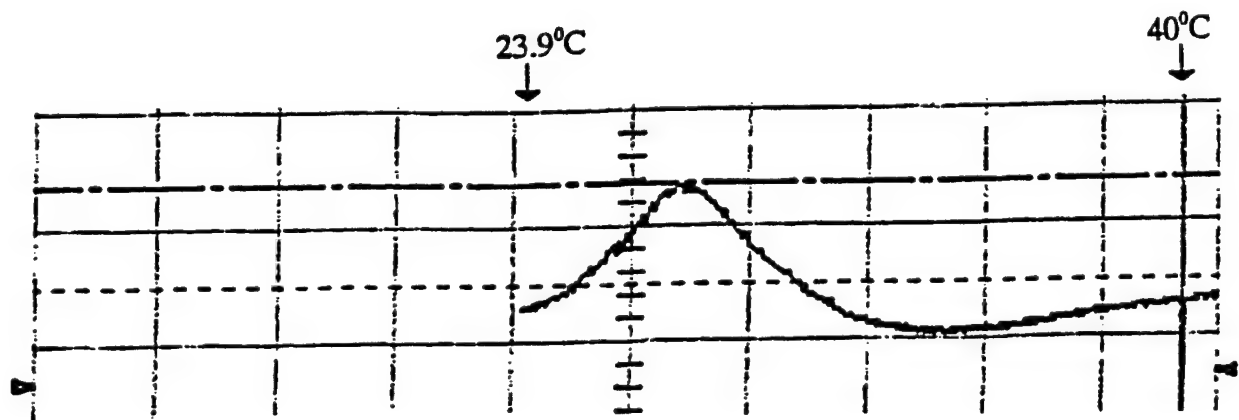


Figure 55 Uncalibrated sensor output (83.07% compensation).

Using Eq. (3.12), new compensator length was calculated from the observed $\Delta l/\Delta T$. The temperature compensation obtained with the new sensor was 94.96% as can be seen in Figure 56.

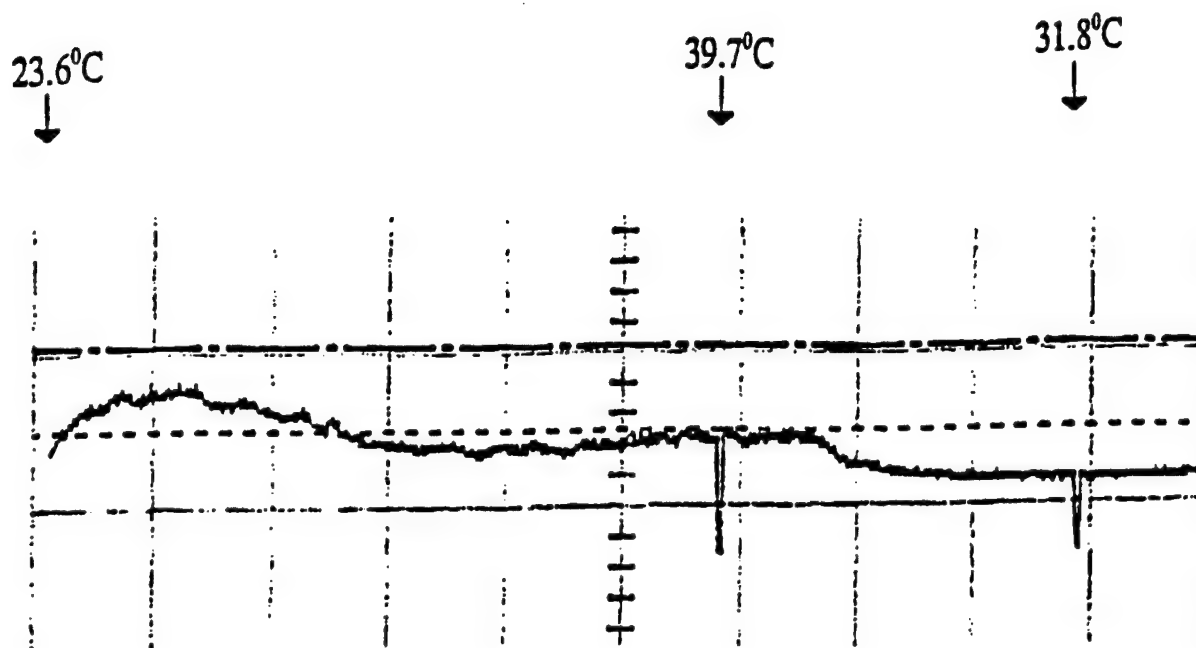


Figure 56 Calibrated sensor output (94.96% compensation).

Thus, an improvement of 11.89% was observed. To obtain exact compensation, 10 sensors were fabricated with compensator lengths varying between -4mm to +5mm of the current compensator length. The evaluation results are presented in Table 8.

Table 8 Evaluation of sensors for exact temperature compensation.

#	L_m (cm)	L_t (cm)	$\Delta l/\Delta T$ $\mu m/^{\circ}C$ comp.	Temp. Comp. %	Long term Var. %	$\Delta l/\Delta T$ $\mu m/^{\circ}C$ uncomp.	Tube length, L_{exact} cm	$L_t -$ L_{exact} (cm)
1	3.9	5.625	0.0508	78.89	100	0.2406	6.057	-0.432
2	3.85	5.6	0.0305	87.16	100	0.2375	5.98	-0.380
3	3.75	5.65	0.0169	92.70	59.09	0.2314	5.824	-0.174
4	4.2	6.4	0.0100	96.13	83.33	0.2591	6.523	-0.073
5	4.175	6.4	0.0122	95.28	50	0.2576	6.484	-0.084
6	4.2	6.55	0.0080	96.92	25.97	0.2591	6.523	0.027
7	4.2	6.65	0.0035	98.65	25.64	0.2591	6.523	0.127
8	4.225	6.8	0.0047	98.19	28.81	0.2607	6.56	0.240
9	4.225	6.9	-	-	-	0.2607	6.56	0.340
10	4.25	7.05	0.0189	92.81	55.56	0.2607	6.60	0.450

The value $L_t - L_{exact}$ for the 98.65% compensated sensor (Figure 57), is actually 0.12cm though it is intended to be 0.2 cm. It is extremely difficult to control this length exactly due to the spreading of the epoxy and inaccurate cutting of the tube. The spreading of the epoxy was observed to be 1~1.5 mm from the end of the tube. This value was empirically used in all the subsequent sensor designs.

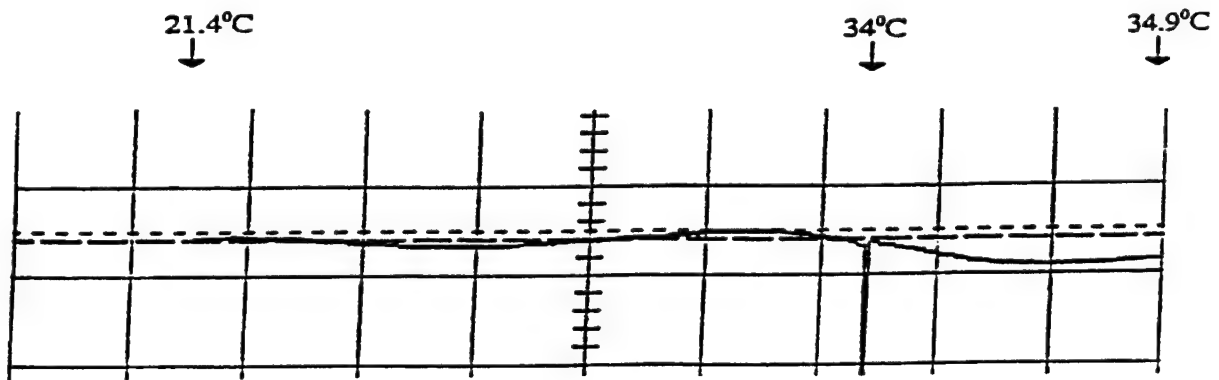


Figure 57 Temperature compensated sensor output (98%).

The temperature evaluation of all the sensors was done in a thermal chamber to ensure a slow rate of rise in temperature so that the gage and compensator remain at the same temperature during the experiment. Long-term variation shows the actual performance of the sensors when placed in ambient conditions. This was usually done over 13 hrs. The sensors evaluated over long periods were subjected to the thermal variations due to the lab air conditioning. A change in the output of one half a fringe was considered as 100% fluctuation. As can be seen from the table, the sensor showing 98% temp. Compensation in the chamber showed a 20% variation over a long period. This discrepancy is mainly due to the heat capacity difference between the sensor gage and Borosilicate tube, and the geometry of the sensor in which the gage is enclosed inside the tube that is sealed at both ends. Hence, the Borosilicate tube absorbs heat first and expands. It then radiates heat to the gage that expands later. Thus, there is always a heat transfer lag between the compensator and the sensor gage. Once the heat capacity of the compensator is filled, it does not absorb any more heat and thus ambient temperature changes are directly transmitted to the gage. Once the gage heat capacity is filled, the temperature compensation scheme works. This effect is clearly visible in Figure 58.

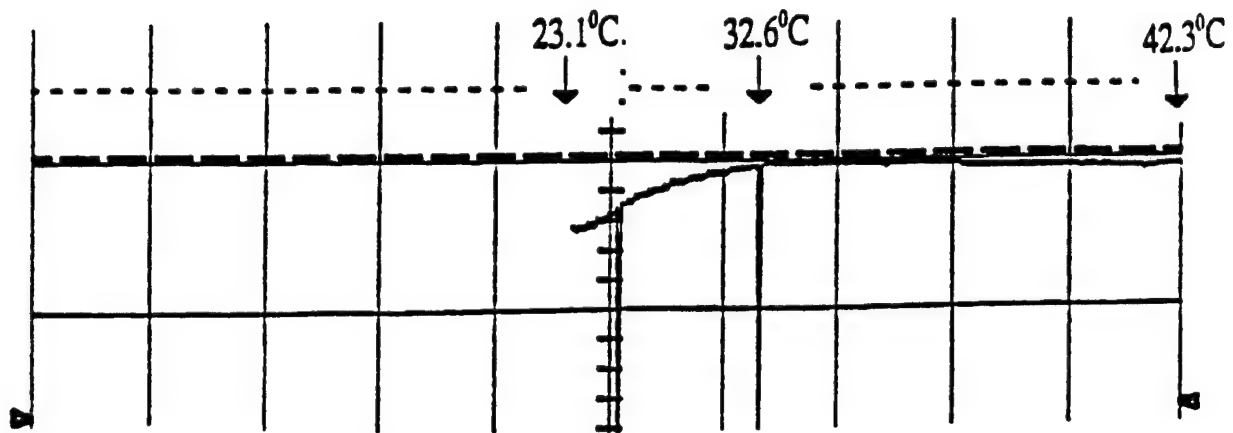


Figure 58 Effect of heat capacity on sensor operation.

Hence, exact CTE values cannot be found. Even if the temperature is raised very slowly during the experiment (e.g. $1^{\circ}\text{C}/1\text{Hr}$), the actual compensation is limited by heat capacity and heat transfer ratio of each material. Hence, in order to reduce the asynchronous expansion of Metglas wire and compensator tube, the heat capacity of the tube should be reduced as much as possible. One way to reduce this effect is to reduce the mass of the compensator. Another is to select a material with low specific heat. At the same time, the CTE of the material has to be between that of Metglas and silica fiber. This is done by drawing borosilicate glass hollow core tubes with lower wall thickness as well as smaller inner diameters such that the heat transfer between the tube and Metglas wire is enhanced. Packaging the sensors such that ambient temperature change is delayed before reaching the actual sensor itself, over the operating temperature range, is another possible solution.

3.4 Improvement of Fringe Visibility

The polished Metglas endface is extremely bright, with a reflectance of more than 0.5. The air-fiber interface reflectance is 0.04. Hence, the intensity of the second reflection is nearly 11 times that of first reflections. The fringe visibility, as a result, is as low as 20%. The system sensitivity is affected by this low fringe visibility as small fluctuations in the laser output mask the effect of low magnetic fields. The fringe visibility can be controlled by reducing the reflectance of Metglas wire and increasing the air gap between the Metglas wire and the reference fiber. Making the air gap large causes misalignment between the arms and makes it more susceptible to vibrations. Another way to increase the fringe visibility is to polish the end face of the Metglas fiber at an angle. The output of the laser used in the system is single mode. This mode, HE_{11} has a Gaussian field profile inside the core of the reference arm and a slightly distorted field outside the core at interface II. For exact analysis of the slant angle, we need to solve Maxwell's equation at the interface but for a rough idea about the angle, simple ray optics can be used. The geometry is shown in Figure 59.

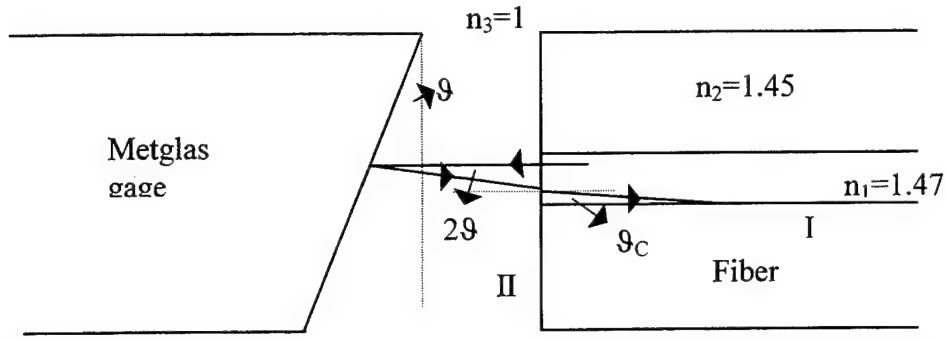


Figure 59 Modified sensor gage endface.

The tangential component of the electric field is continuous at the core-cladding boundary (I) and air core interface (II). At the interface I, the critical angle is given as

$$\theta_c = \cos^{-1}\left(\frac{n_2}{n_1}\right) = \cos^{-1}\left(\frac{1.45}{1.47}\right) = 9.46^\circ \quad (3.15)$$

At interface II, the tangential component is continuous as

$$n_3 \sin 2\theta = n_1 \sin \theta_c \quad (3.16)$$

From Eq. (3.16), the angle θ is obtained as

$$\theta = \frac{1}{2} \sin^{-1}\left(\frac{n_1 \sin \theta_c}{n_3}\right) = 6.99^\circ \quad (3.17)$$

Thus, any value of θ , smaller than 6.99° satisfies the critical angle condition. The sensors currently fabricated, have a slant angle of 5° . As a result, fringe visibility of over 95% is obtained in most of the current sensors. Figure 60 shows the output of one of these sensors. The air gap is adjusted to be about $2.64 \mu\text{m}$. Thus, this method gives both high fringe visibility and lower vibration sensitivity due to smaller air gap.

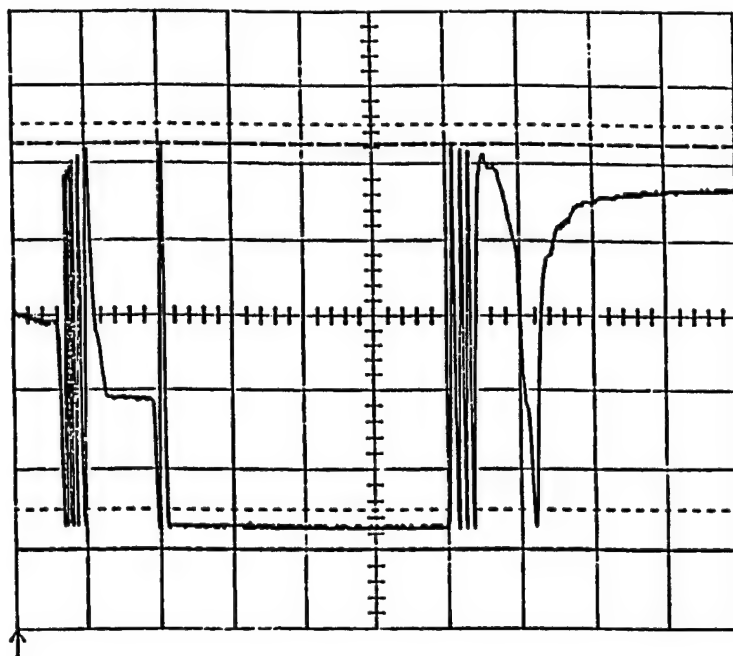


Figure 60 Improvement in the fringe visibility.

3.5 Optimal Biasing and Packaging Methods

3.5.1 Biasing the Sensor

Biasing the sensor in the region of maximum magnetostriction is one of the key issues in the working of the sensor. As can be seen from the magnetostriction curve (shown in Figure 53) of the new Metglas material, the curve has maximum slope and linearity in the region between 1 G and 10 G after transverse field annealing. The saturation magnetostriction is about 20 G. Thus, in order to get maximum sensitivity from the sensor, it is necessary to DC bias the sensor such that it operates in this linear region. Several biasing methods were considered and tried for this purpose. One way of biasing the sensor was to use a small coil wound over the sensor package. This could provide a steady, controllable and uniform DC magnetic field over the entire length of the sensor material. The operating point of the sensor could also be controlled in this case using feedback from the sensor output itself. But this would require the use of a current source and Hence, active circuitry in the system. This method, thus, being unfeasible for satellite

deployment was not investigated further. The DC field biasing method demonstrated in Chapter 2 was, as shown in Figure 61.

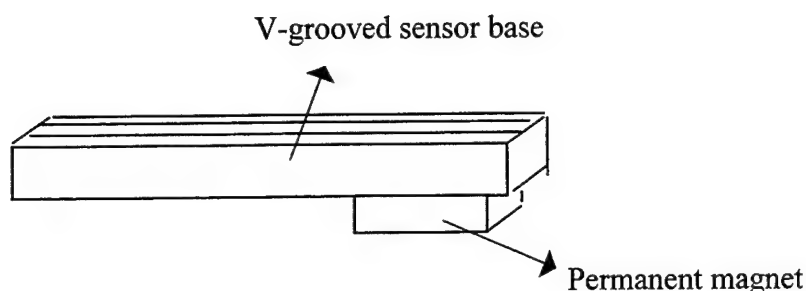


Figure 61 DC bias method using single permanent magnet.

In this method, a single permanent magnet was attached at one of the ends of the sensor at an appropriate distance such that the field over the sensor material was enough to keep it operating in the linear region. But the problem with this method was that the field was highly non-uniform due to the use of a single, strong magnet and the sensor, after packaging was quite bulky, even without thermal insulating material around it. During this reporting period, the DC biasing method that followed was on the same lines as the previous, but more refined. In the new method, two small pieces of a permanent magnet are attached to the ends of the sensor as shown in Figure 62.

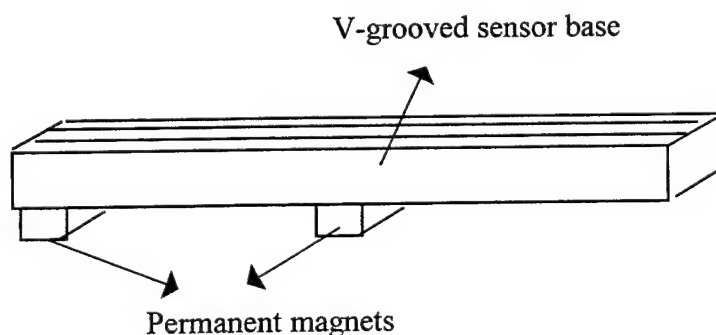


Figure 62 Using two, small permanent magnets for DC biasing the sensor.

In this case, the field over the sensor length is significantly less non-uniform as compared to the single magnet scheme, though it is still non-uniform. The magnets being small and compact, the sensor package is not very bulky and Hence, it can be packaged with a thermally insulating material around the actual sensor. This plays a significant role in enhancing the stability of the system. The magnets in this case being small, the field decays at a very fast rate as one moves away. Thus, the possibility of the DC bias affecting the external field to be measured is reduced. As two magnets are used instead of one, the magnetic field is much more uniform along the line joining the two magnetic poles. All the sensor pairs prepared during this reporting period have a DC bias provided by such small magnet-pairs.

3.5.2 Packaging the sensor

Sensor packaging is another important area in the development of the system. Not only does the package protect the sensors from external mechanical disturbances but it also helps reduce the effect of external parameters like temperature on the sensor. This is very significant as temperature fluctuations around the sensor result in a highly unstable sensor output. During the course of the project, various packaging schemes were developed to house the sensors. In one of the schemes, the sensor-pair was placed on a V-grooved aluminum base, filed down to much smaller dimensions. The DC bias was provided by a pair of small permanent magnets. Once the sensor pair and the magnets were ready, the entire assembly was wrapped in an aluminum foil, covered by thermally insulating ceramic putty and sealed in a cylindrical brass tube. The ceramic putty used for its thermal insulating property has a thermal conductivity of $0.65 \text{ BTU/Hr.}^{\circ}\text{F.ft}^2$ at 500°F . Figure 63 shows the packaging scheme using a V-grooved base.

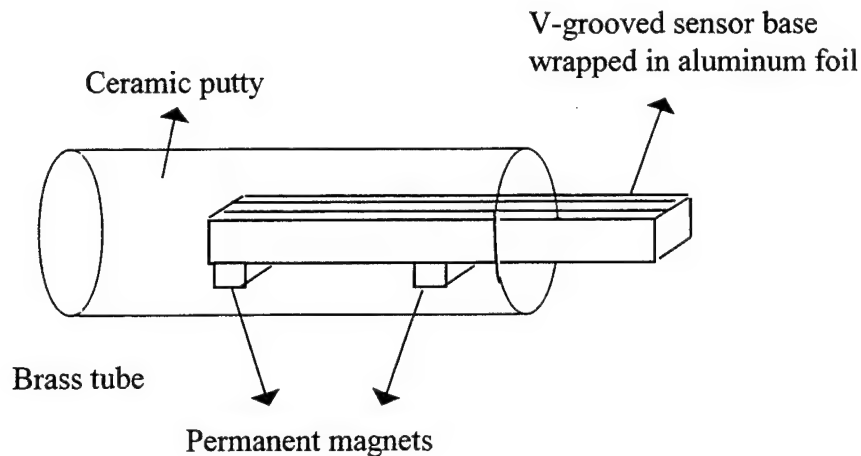


Figure 63 Packaging scheme using V-grooved base.

The principal advantages of the above scheme are sensitivity and stability. Since the sensors are held in place by the sides of the V-grooves, bending of the sensor is almost completely avoided. As a result, the movement of the sensor wire inside the tube is restricted to the longitudinal axis only. This enhances the sensitivity of the sensor. As the sensor is held in place by the V-grove, it is much less susceptible to vibration. Hence, it is more stable than a free-standing sensor. The disadvantage of this scheme is the bulky size of the whole package. The V-grove base, though smaller than the one previously used, is still quite bulky. This problem is eliminated in the other packaging scheme developed during this reporting period. However, there is a tradeoff between the package size and the sensitivity-stability of the sensors. Figure 64 shows another packaging scheme.

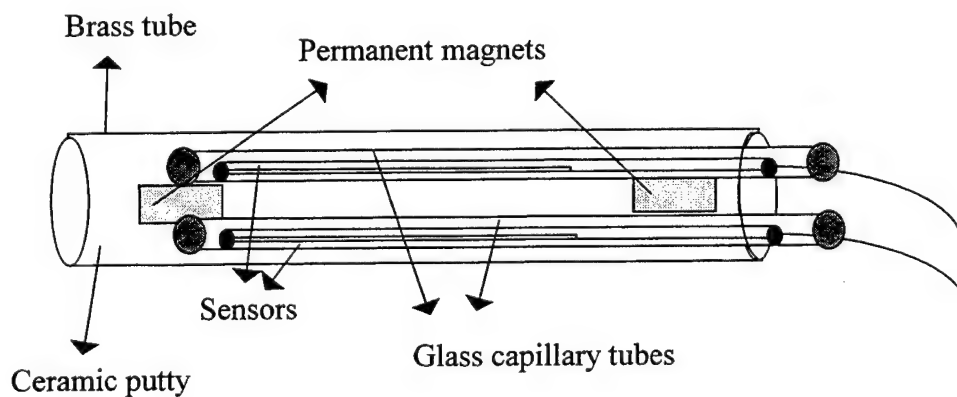


Figure 64 Packaging scheme using glass tubes.

In this scheme, each sensor is sealed inside a small, glass, capillary tube. The two glass tubes (one for each sensor) are attached to a single base material and two permanent magnets are attached to the two ends of the tubes. The entire assembly is then coated with a ceramic putty as in the previous case and sealed inside a brass cylinder. The sensor package, in this case, is significantly smaller than the previous scheme. One main advantage observed in both sensors due to the use of ceramic putty, was the stability of the output. The new sensor packages are significantly stable as compared to those fabricated for preliminary experiments. The cables, covering the optical fibers used in the sensor, are another cause of induced strain in the sensors.

3.6 Low Magnetic Field Detectability

The entire system, using new sensors, was evaluated for linear response to magnetic field. The DC bias to the sensor material was provided by two small magnets placed at the ends of the sensor. The two sensors in each pair were quadrature phase shifted to reduce signal fading common to interferometric measurement methods. System calibration curves for three sensors are shown in Figures. 65-67. The minimum detectable magnetic flux density for relatively short duration was as low as 50 nT (sensor package Tube 3). The output variation for each sensor depends on the gage length and the physical stress imposed during the packaging of the sensors. All sensors using new material, new bias method with two small magnets and new packaging method, showed good responsivity to 100 nT flux density over a fair amount of time.

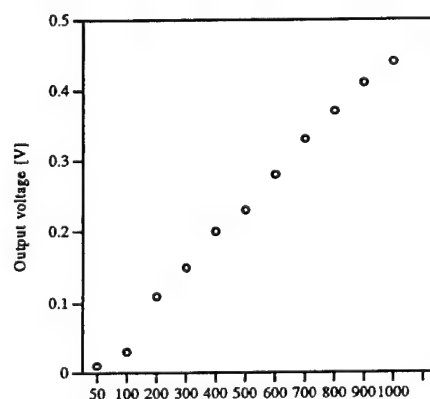


Figure 65 Output of sensor (Tube 3).

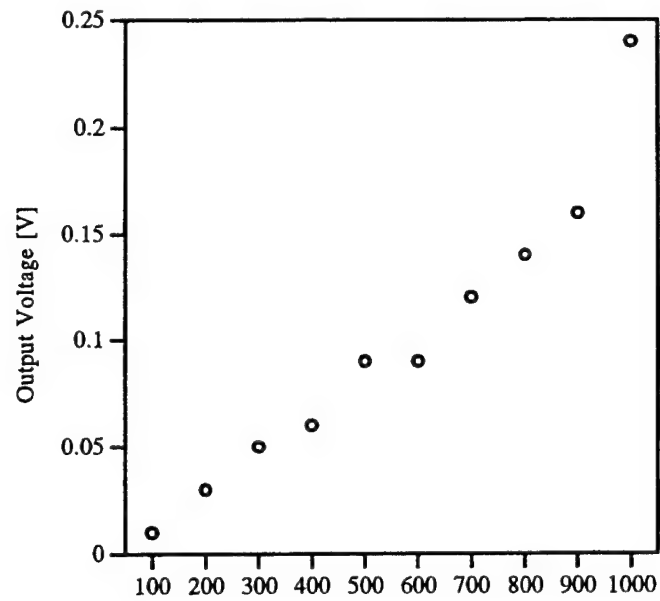


Figure 66 Output of Sensor (Tube4).

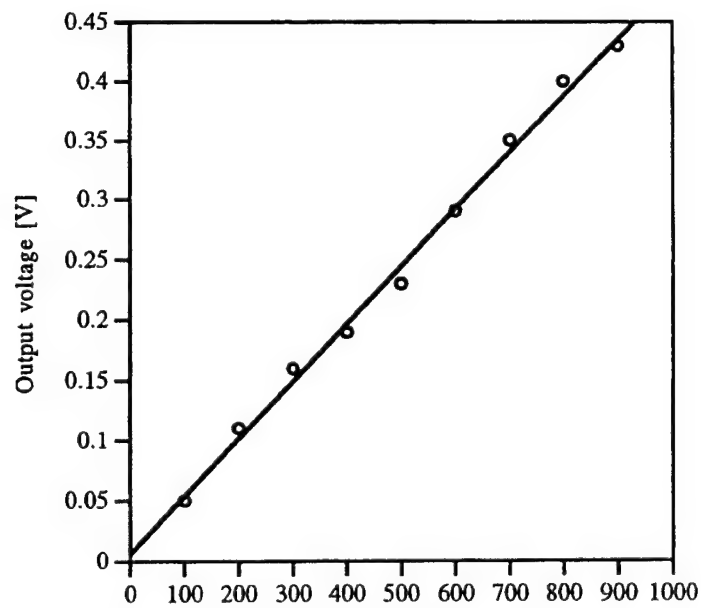


Figure 67 System calibration curve (without ceramic insulator).

Chapter 4: Design of Three Dimensional Vector Field Measuring System

4.1 Three Dimensional Vector Field Representation

The vector magnetic field is represented as a combination of three components along the Cartesian coordinate axes. The field along each of the three axes can be individually measured by sensors placed in the direction of the corresponding component. A single sensor can be easily used to measure the amplitude and direction of the magnetic field in that direction. The amplitude of the component is directly represented by change in the sensor output voltage and the direction can be obtained by comparing the output voltage with the reference voltage (output at the initial operating point). Thus, the change in voltage is positive or negative depending on the direction of the applied magnetic field.

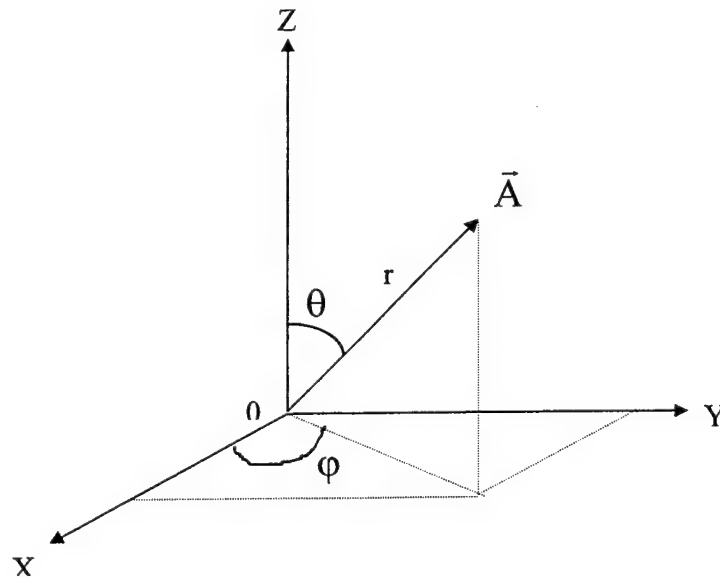


Figure 68 Vector representation of magnetic field.

The vector field can also be represented in spherical coordinates as shown in Figure 68 by using Eqs (4.2), (4.3) and (4.4). The vector \vec{A} can be expressed as

$$\vec{A} = A_x \hat{x} + A_y \hat{y} + A_z \hat{z} \quad (\text{Cartesian coordinates}) \quad (4.1)$$

where $A_x = r \sin \theta \cos \varphi$, $A_y = r \sin \theta \sin \varphi$, $A_z = r \cos \theta$.

Hence, in spherical coordinates

$$r = \sqrt{A_x^2 + A_y^2 + A_z^2}, \quad (4.2)$$

$$\theta = \tan^{-1} \left(\sqrt{\frac{A_x^2 + A_y^2}{A_z^2}} \right), \quad (4.3)$$

$$\varphi = \tan^{-1} \left(\frac{A_y}{A_x} \right). \quad (4.4)$$

Thus, the amplitude and direction of the vector magnetic field can be calculated if the three Cartesian components of the field are known. The arrangement of the sensors for measuring these three components is as shown in Figure 69. Figure 70 shows the initial operating point of each of the sensors. As can be seen from the figure, the movement of the operating point along the slope depends on the overall applied magnetic field and can thus be used to measure the direction of the applied field.

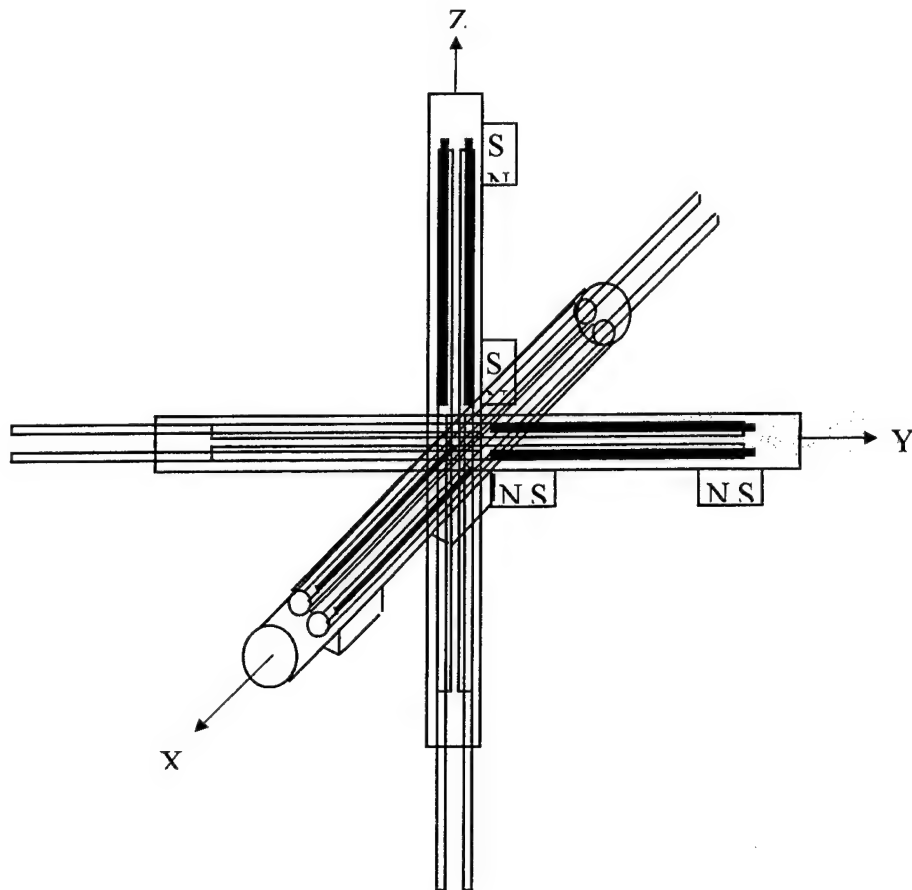


Figure 69 Sensor arrangement.

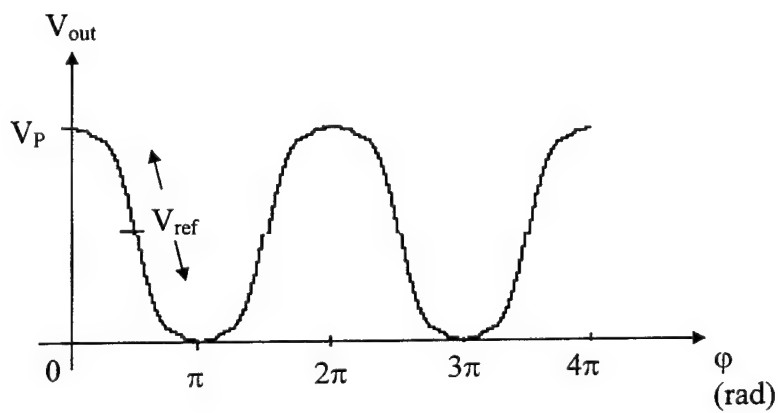


Figure 70 Initial operating point of the sensors.

If the direction of the external applied magnetic field is opposite to that of the biasing field, the overall magnetic field applied to the sensor decreases and so does the length of the metglas wire. Thus, the phase difference between the first and second reflection increases. If the sensor operates at the point shown in Figure 70, the output voltage falls below the reference voltage. In case the direction is the same as that of the biasing field, the output voltage goes above the reference voltage. Thus, the direction of the applied magnetic field can be easily determined.

4.2 Design of Vector Field Measurement System

4.2.1 Sensor Head Design

In order to avoid magnetic induction in the sensor head itself, the material chosen is ferrimagnetic. Aluminum is one likely candidate. It also has the advantage of light weight and large heat capacity. Figure 71 shows a schematic view of the sensor head. The circular hole, bored in each of the rectangular projections of the sensor head, houses the two quadrature phase shifted sensors used to measure the field in that particular direction. The small biasing magnets are also housed in the holes along with the sensors.

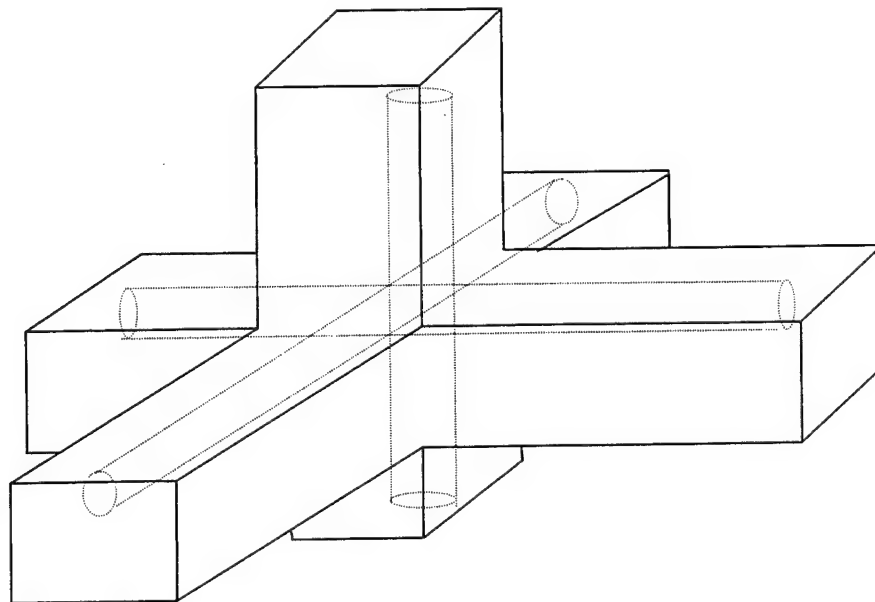


Figure 71 Sensor head for vector magnetic field measurement.

4.2.2 System Design with three Separate Laser Sources

In this design, each sensor pair has its own laser diode source. Figure 72 shows the schematic for this particular design.

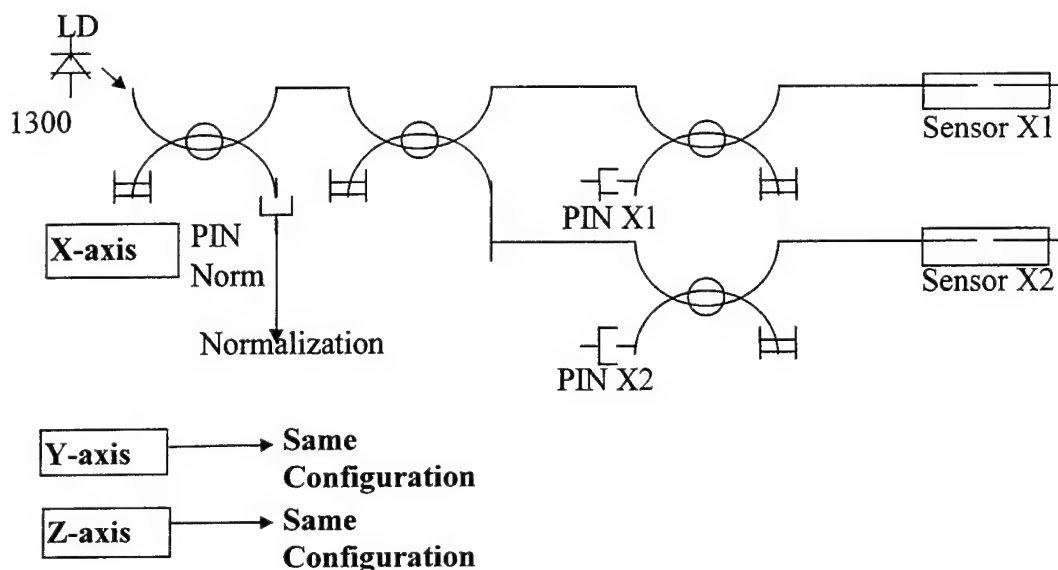


Figure 72 Design using three separate laser diodes.

Each laser diode has to drive at least three channels: two for the quadrature phase shifted sensors themselves and one for the normalizing input. Thus, the design consists of three stages of 3-dB couplers. The optical power at the input of the PIN diodes is Thus, 12 dB below the output of the laser diode. The advantage of using this design is the possibility of using low-power laser diodes for each axis and enhanced total system reliability. The disadvantage is the higher cost.

4.2.3 System Design with Single Laser Source

For this particular design, only a single channel is needed for the normalization input. Thus, the total minimum number of channels required is seven. The design has four stages of 3-dB couplers providing an attenuation of 15 dB at the input of the PIN diode. Thus, in this case, higher power laser diode is certainly required. Figure 73 shows the schematic for this design.

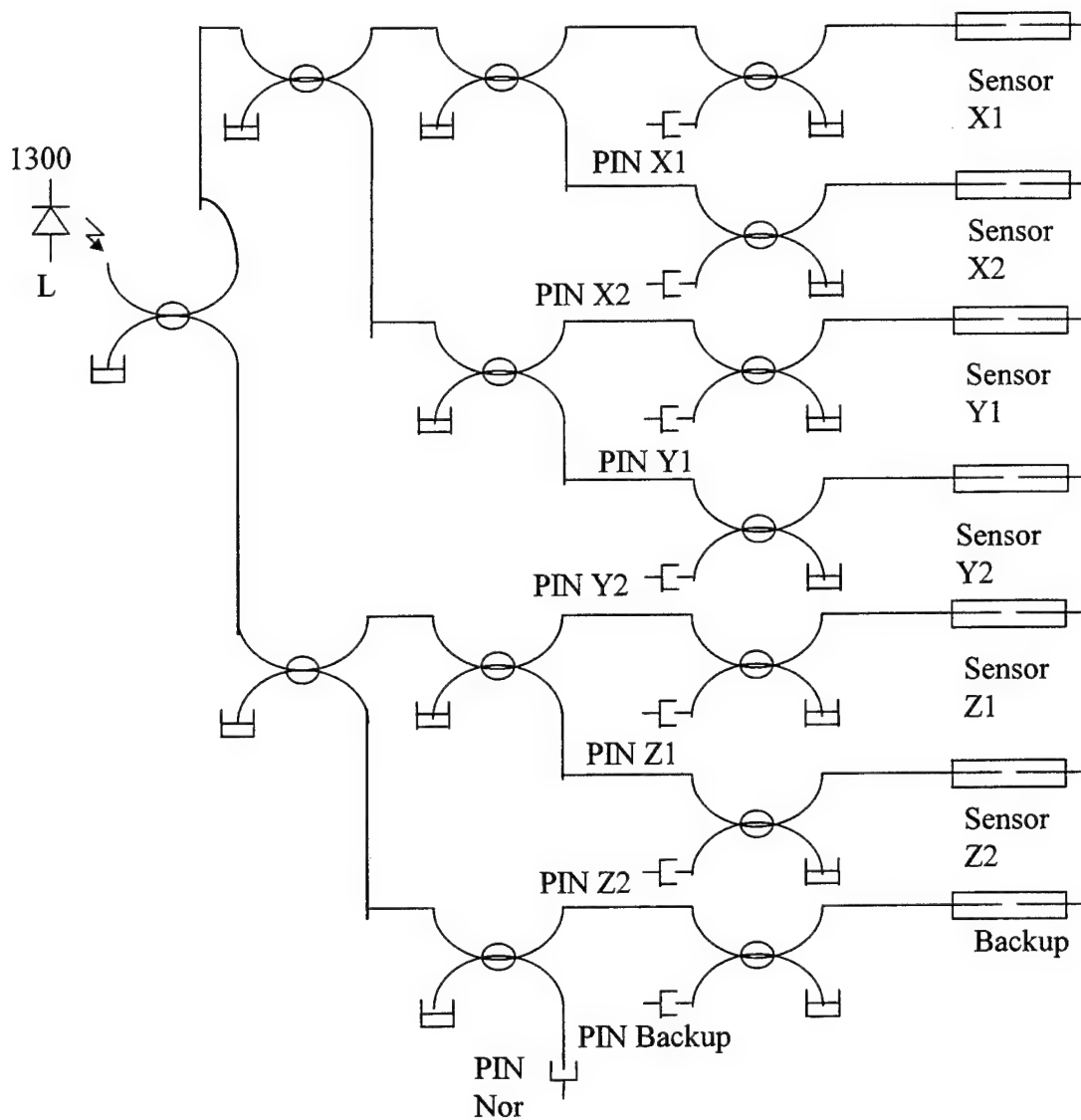


Figure 73 Design using single laser diode.

Table 9, shown below, compares the resource requirements and advantages/disadvantages of the two designs.

Table 9 Resource comparison for three-diode and single-diode designs.

	<u>Three-diode design</u>	<u>Single-diode design</u>
Total channels	9(6+3)	8(7+1)
PIN Diodes	9	8
3-dB couplers	12	14
Temperature controllers	3	1
Current drivers	3	1
Remarks	Lower laser-diode power, large number of supporting components, three normalizations, costly.	Less components, slightly higher laser-diode power, less number of supporting components, single normalization, reliable, less costly.

4.3 Electronic Signal Processing

The electronic signal processing system in the optical fiber based magnetometer essentially consists of the opto-electronic conversion circuitry, the signal demodulation scheme and the display. The opto-electronic interface converts the optical signal output from the sensors into electrical form and the quadrature phase shift (QPS) signal demodulation scheme obtains phase information from it. After appropriate scaling and calibration the output is displayed in terms of external magnetic flux density. Figure 74 shows the various components of the electronic signal processing involved in the magnetometer system.

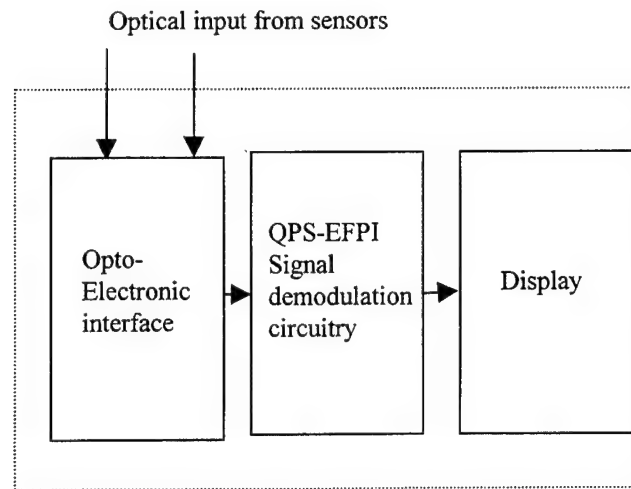


Figure 74 Components of the electronic signal processing system.

4.3.1 Opto-electronic Interface

As can be seen from the above figure, the opto-electronic interface is responsible for the faithful conversion of the optical signal into electrical form. Electronic signal processing offers various critical advantages particularly in the ease of implementation. Once the signal is in the electrical domain, techniques like amplification and filtering can be easily applied in order to enhance the signal-to-noise ratio (SNR) of the system. Not only is this important, particularly in high resolution systems, but necessary in the magnetometer system. Thus,, the most important requirement on the interface circuitry is the accurate reproduction of the optical signal in electrical form with the addition of minimal external noise. Figure 75 shows the circuit diagram of the pre-amplifier circuitry.

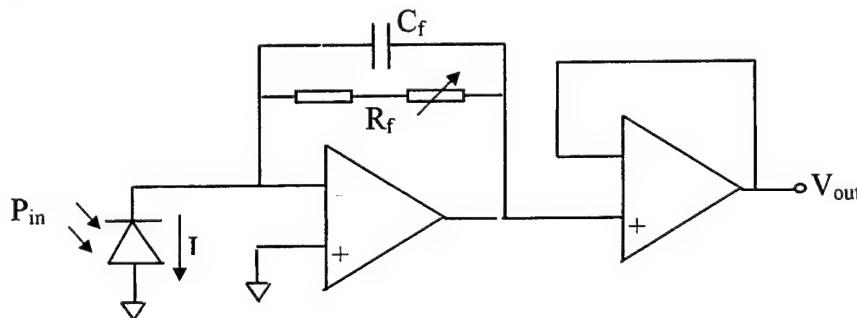


Figure 75 Schematic of a single-channel preamplifier circuit.

The optical signal returning from the sensor is incident on the PIN diode. Thus, inducing a reverse photo current in it. This current flows through the feedback resistor causing a voltage drop across it. The current flowing through the diode is directly proportional to the intensity of the optical input. Low input current and offset voltage levels are the most important requirements on the operational amplifiers used in such sensitive photodiode applications. The first stage of the preamplifier circuit is thus a current to voltage converter or a trans-impedance amplifier. The second stage of the preamplifier circuit is a voltage follower with high input and low output impedance. This stage prevents subsequent stages from loading the preamplifier circuitry. In a typical preamplifier circuit shown in Figure 75 above, the output of the amplifier is given by Eq. (4.5).

$$V_{out} = P_{in} \cdot R \cdot R_f \quad (4.5)$$

where P_{in} is the incident optical power in watts, R_f is the value of the feedback resistor in ohms and R is the responsivity or sensitivity of the PIN photodiode (unit Amp/Watt). An equivalent model for a photodiode and its dc error sources is shown in Figure 76.

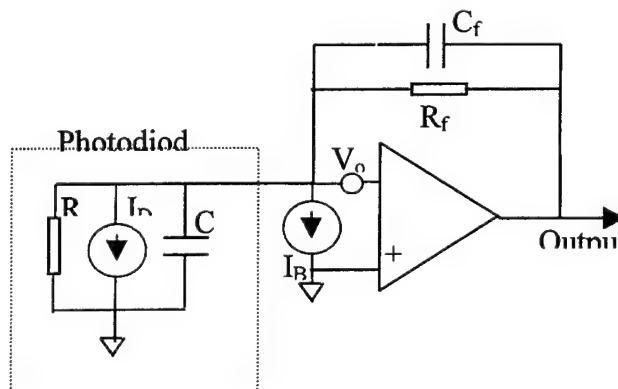


Figure 76 Equivalent photodiode model with dc error sources.

The amplifier's input current, I_B , contributes to an output voltage error which is proportional to the value of the feedback resistor. The offset voltage error, V_{OS} , causes a dark current error due

to the photodiode's finite shunt resistance, R_D . The resulting output voltage error, V_E , is given by Eq. (4.6) as,

$$V_E = (1 + R_f/R_D)V_{OS} + R_f I_B \quad (4.6)$$

In order to prevent the generation of unwanted noise signals in the preamplifier, the optoelectronic conversion circuitry is encased in an EMI resistant enclosure. In addition to shielding the circuit from EMI, the aluminum enclosure offers mechanical protection to internal components like photodiodes.

4.3.2 Quadrature Phase Shifted EFPI Signal Demodulation Scheme

Once the sensor output is converted into electrical form, Quadrature Phase Shift (QPS) signal demodulation scheme is employed in order to detect the phase signal. This technique ensures the signal phase detection regardless of the initial phase of the sensor. The technique uses two sensors which are 90° out of phase or "in quadrature". For these two sensors, the output voltage can be approximated by Eqs. (4.7) and (4.8).

$$V_{out1} = V_{dc1} + V_{max1}(1 + \cos(\varphi)), \quad (4.7)$$

$$\text{and} \quad V_{out2} = V_{dc2} + V_{max2}(1 + \sin(\varphi)), \quad (4.8)$$

where φ is the phase difference between the two reflected beams. When the change in the phase $\Delta\varphi$ is small, the following approximations hold.

$$\Delta V_{out1} = -V_{max1} \sin \varphi \Delta \varphi, \quad (4.9)$$

$$\text{and} \quad \Delta V_{out2} = V_{max2} \cos \varphi \Delta \varphi. \quad (4.10)$$

Defining a signal S in the following way,

$$S = \sqrt{(V_{out1})^2 + (V_{out2})^2}, \quad (4.11)$$

and adjusting V_{max1} equal to V_{max2} ,

$$S \propto \Delta \varphi. \quad (4.12)$$

Thus, the output signal S is linearly proportional to the change in phase signal and independent of its initial value for small phase changes. Each sensor can be brought to its initial operating point by adjusting the initial air gap. A block diagram of the signal demodulation system (for a single axis) is as shown in Figure 77.

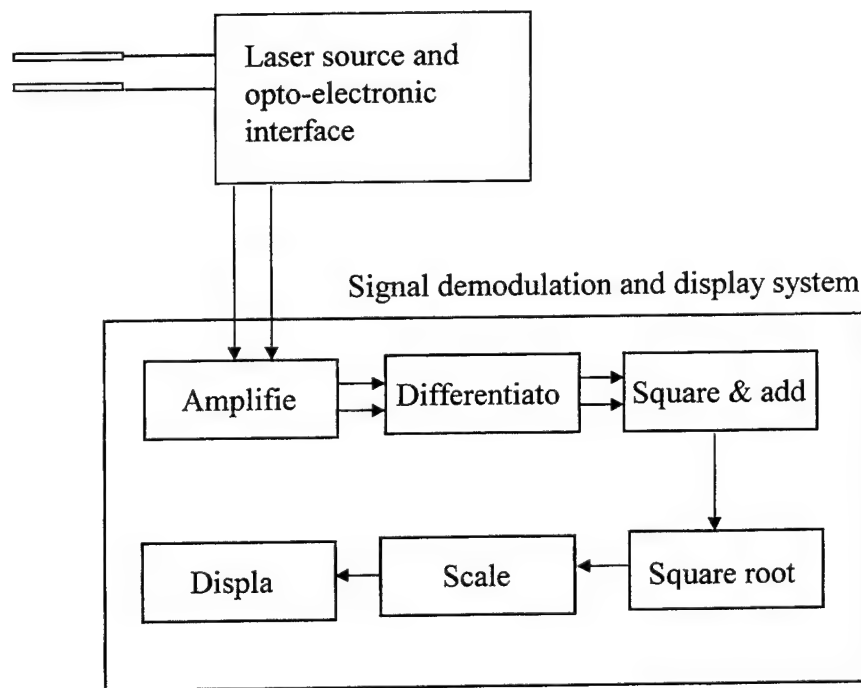


Figure 77 Block diagram of QPS signal demodulation scheme.

4.3.3 Analog Implementation

The signal demodulation scheme explained above can be electronically implemented in either analog or digital domain. This section details the analog implementation of the scheme.

Figures. 78a and 78b show the block and circuit schematic of this system.

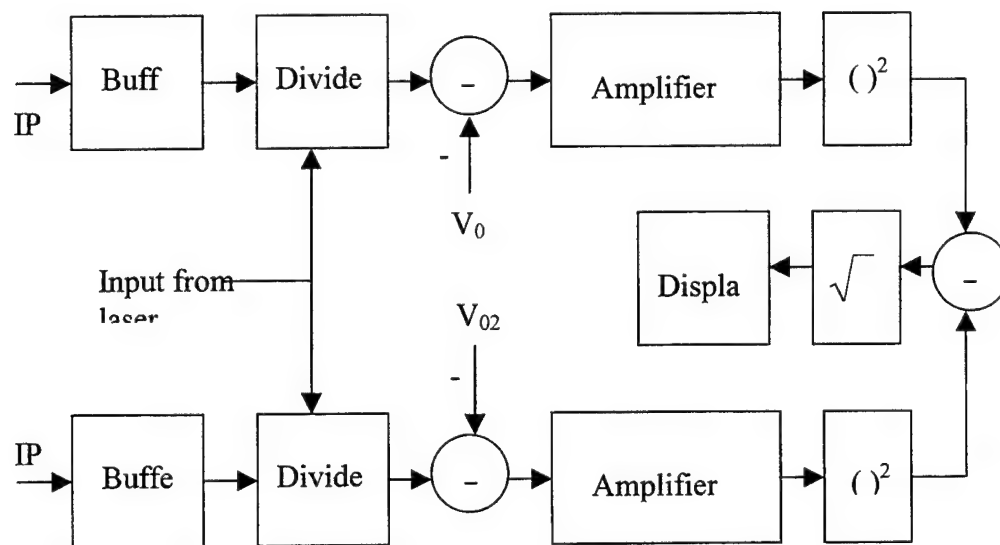


Figure 78a Analog implementation of QPS signal demodulation scheme.

As shown in the figure, the electrical sensor outputs from the interface circuit are first normalized to the laser diode output using linear divider integrated circuits (ICs). This eliminates the low frequency noise in the system arising due to variation in the laser output power. These normalized signals are then differentiated by subtracting their initial signal values from the current ones. The subtraction is carried out using operational amplifiers. These differentiated sensor outputs are then squared using linear multiplier ICs and added. The square root of this summed signal is then scaled, calibrated and displayed in terms of external magnetic flux density. Although an analog system implementation is simple in design and fabrication, it has several major disadvantages, some of which are given below.

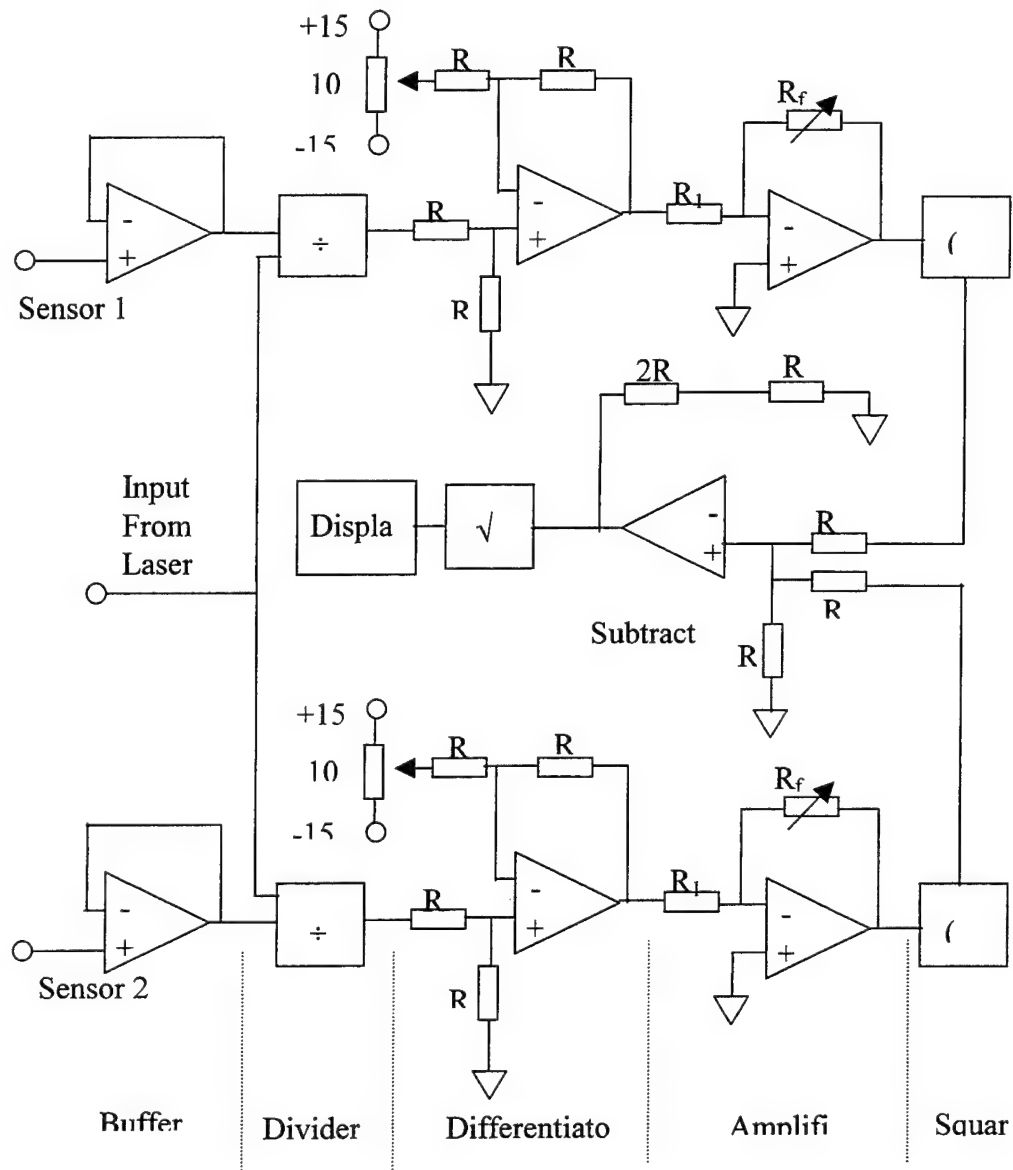


Figure 78b Circuit schematic of the demodulation system.

- Additional thermal noise generated in the circuit degrades the SNR of the overall system.
- Components like resistors and capacitors, with precise values, are generally not easily available.

- Linear integrated circuits like multipliers and dividers have inherent inaccuracy in the computed signal output.
- Fabrication of the circuit, although simple, is time consuming.
- The system implementation is not flexible as modification is difficult.

Since SNR, accuracy, flexibility and speed are critical in the ultra-high sensitivity magnetometer system, it is clear from the above discussion, that analog implementation of the signal demodulation scheme is not suitable for this particular application. Thus, a microprocessor-based, digital signal demodulation scheme is used in the final magnetic field measuring system. The next section describes the various advantages and implementation of this system.

4.3.4 Microprocessor-based Signal Demodulation

A microprocessor based signal demodulation scheme is used in the final magnetometer system. This increases the signal processing accuracy and eliminates manual calibration of the individual sensors as well as increases system reliability and flexibility. Figure 79 below shows the schematic of the digital implementation.

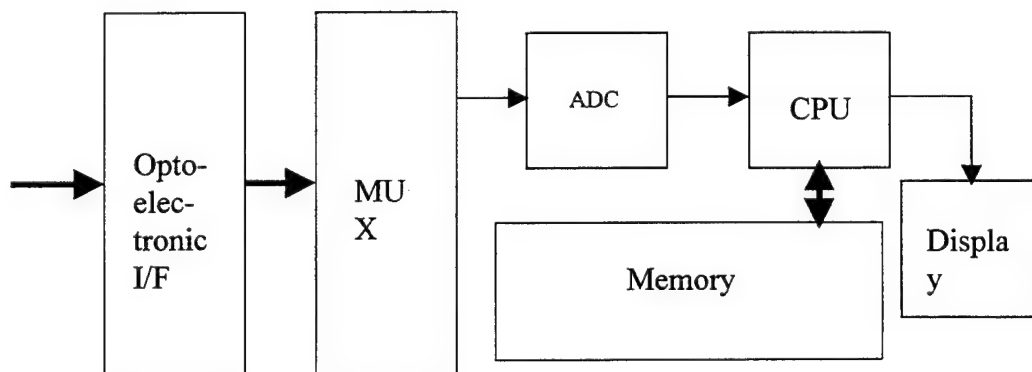


Figure 79 Schematic of microprocessor-based signal demodulation system.

The electrical signals from the sensors and the normalizing input from the laser source are all fed into the 16X1 multiplexer through the opto-electronic interface. The analog to digital converter (ADC) converts each signal into a 12 bit word. The central processing unit (CPU) performs all

the calculations like normalizing, differentiating, squaring and adding on this data and displays the results on a LCD panel. The software instructions for the signal processing are stored in the memory and can be directly accessed by the microprocessor.

The stand-alone, single board computer (SBC) chosen for this application is based on Intel's 386EX CPU with a clock speed of 25 MHz. The output from the three pairs of sensors (one pair for each Cartesian axis) and the normalizing input is fed to the computer through a 16 channel, 12-bit ADC with an input range of 0-10 V. The resolution of the ADC is Thus, around 2 mV. The overall sampling rate can be as high as 100 KHz. Once the input data is obtained in digital form, all the operations required for quadrature phase shift demodulation are performed on it. The output is displayed on a 4X20 character LCD panel. The SBC can be programmed for self-calibration or can be calibrated either on start-up or during operation. The operation of the SBC can be altered whenever required by downloading new executable files from a PC through a serial port and RS232 cable. Thus, the system offers much higher operational flexibility as compared to analog signal demodulation. Some of the significant advantages of the microprocessor-based system are as shown below.

- Significant reduction in thermal noise as output of preamplifier is directly converted to digital format without further analog processing.
- Increase in system reliability as commercially available single board computer is used for the signal demodulation scheme.
- Sufficient resolution for the required application.
- Flexible operation, since this simply involves modification of software.
- Faster implementation as this only requires downloading of modified executable file on to the single board computer.

4.4 Fabricated Magnetometer System

Figures 80-83 show the complete, fabricated optic-fiber based magnetometer system.

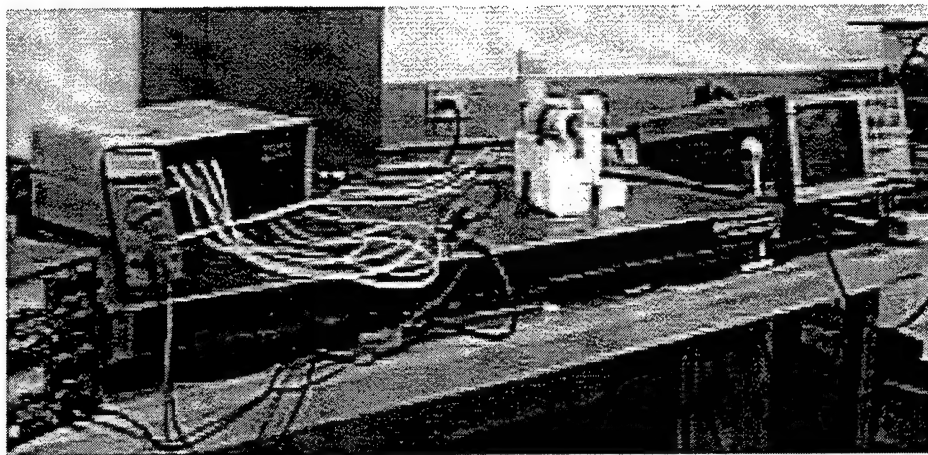


Figure 80 Experimental arrangement of magnetometer system.

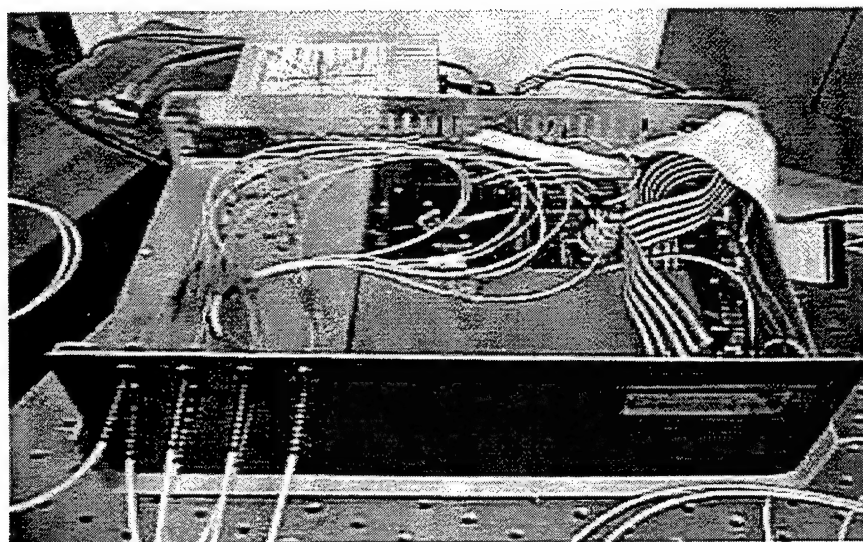


Figure 81 Electronic signal processing system box.

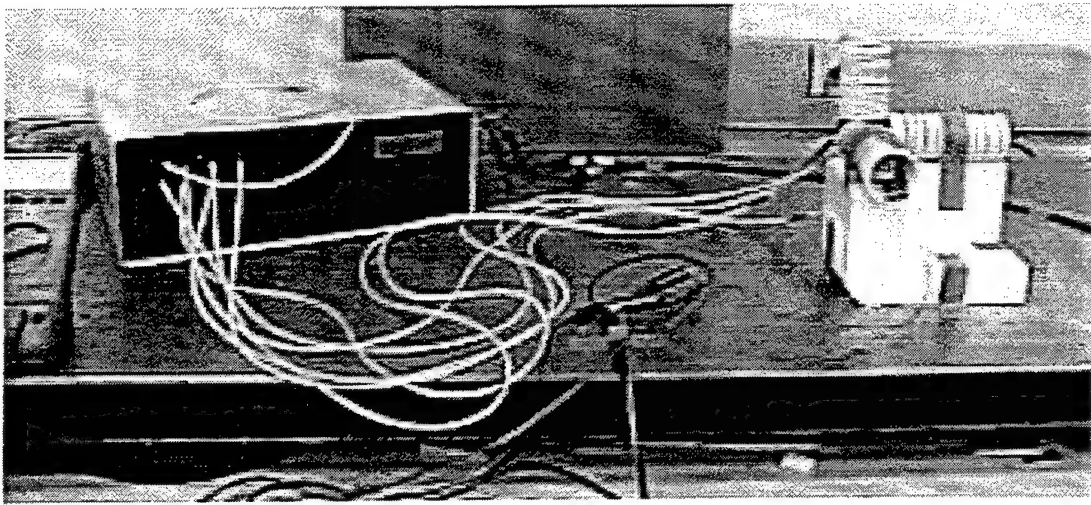


Figure 82 Calibration setup.

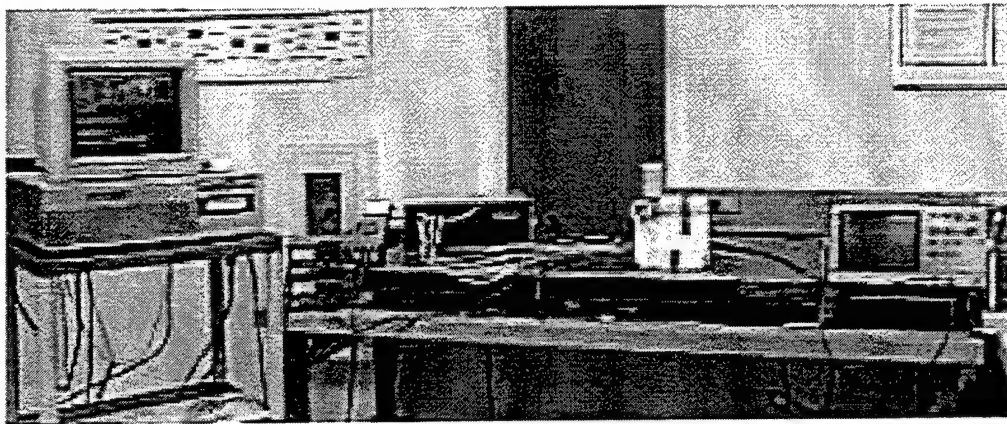


Figure 83 Complete experimental setup.

Chapter 5: System Calibration

5.1 Experimental Setup

Figure 84 shows the schematic of the sensors used in the testing and calibration of the magnetometer system. Since the phase variation of each sensor on application of external magnetic field depends on a variety of external factors, it is essential to calibrate each axis independently. The voltage output of each sensor primarily depends on its operating point, fringe visibility and the strain induced in it due to bending of the fiber.

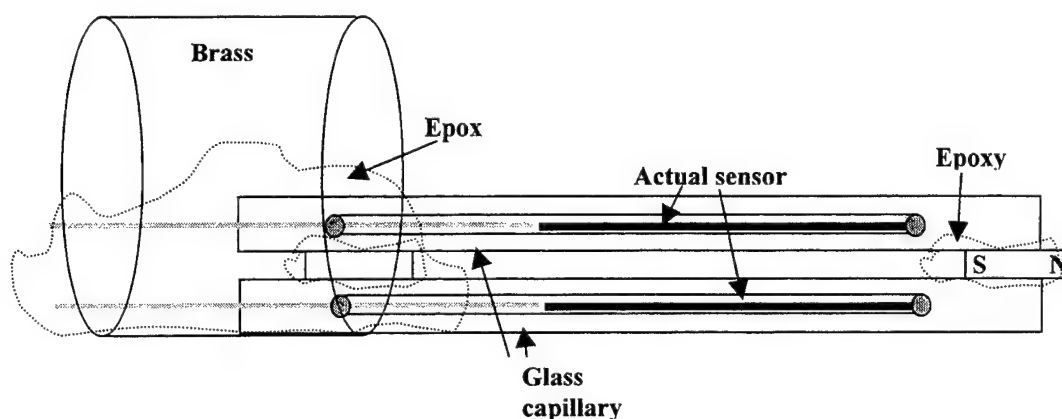


Figure 84 Schematic of a single axis sensor assembly.

As shown in the figure, each individual sensor consists of an EFPI with the sensing fiber replaced by a magnetostrictive wire about $125\text{ }\mu\text{m}$ in diameter. The wire is field-annealed and polished at an angle to increase the fringe visibility of the sensor output. Both the reference fiber and the sensing wire are enclosed in a boro-silicate glass tube with an ID of about $150\text{ }\mu\text{m}$. The tube is sealed at both ends using commercial grade epoxy. Each sensor is then sealed inside a glass capillary tube. Two such sensors, which are in quadrature, are then glued together along with a single permanent magnet for DC bias, using epoxy. The quadrature phase shifted sensor pair is then attached to the inner surface of a small length of brass tube. This reduces the bending-

induced strain on the sensors as well as facilitates the insertion of the assembly into the Aluminum sensor head.

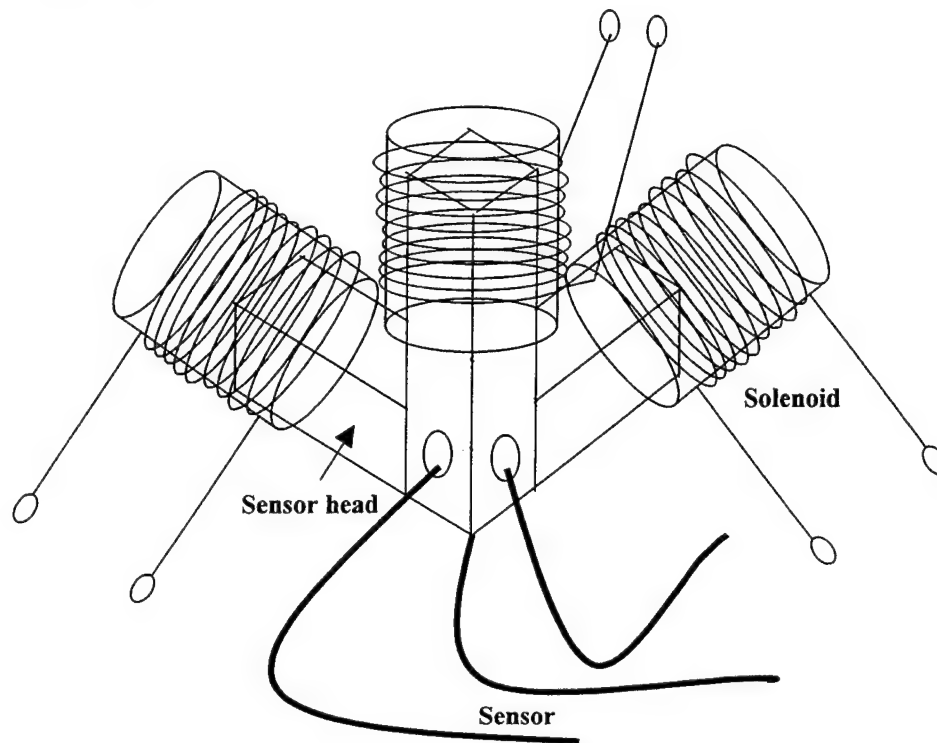


Figure 85 Experimental setup.

Figure 85 shows the overall experimental setup. The quadrature phase shifted, DC field biased sensor pairs are inserted along the three axes of the Aluminum sensor head with minimal strain. Each arm of the sensor head is placed in a solenoid capable of producing the necessary calibration flux density. Once the setup is complete, the assembly is allowed to stabilize for some time. The first part of the experimental procedure deals with determining the magnetic field response of each of the individual sensors. In the second part, the microprocessor-based signal demodulation system calculates the overall signal for each axis. This is essentially the calibration procedure where the relation between the calculated output and the applied external magnetic field is determined. The signal demodulation system samples each sensor output at a rate of 18 Hz. The digitized signal is then averaged over two seconds, normalized to the laser source variation and then used in further calculations. The following sections describe the calibration procedure and the obtained results in detail.

5.2 Calibration Procedure

In order to determine the magnetic field response of each sensor, the sensor pair under investigation was placed inside the calibration coil. The operating point of the sensor with respect to its peak-to-peak value was observed. This is one of the critical factors in obtaining the magnetic response as will be seen from the results. A DC magnetic field was then applied and varied in steps from $-40,000$ nT to $40,000$ nT. The voltage output of each sensor for the applied magnetic fields was observed and measured using an oscilloscope. The procedure was repeated one more time and similar readings were obtained. The magnetic field response (low and high field) for each sensor was plotted. These results are presented in the next section.

Figure 86 shows the typical variation in an EFPI sensor output due to change in phase between the reference and sensing reflections. V_{ref} in the figure denotes the initial operating point of the sensor. As can be seen from the figure, the movement of the operating point along the slope depends on the overall applied magnetic field and can thus, be used to measure the direction of the applied field.

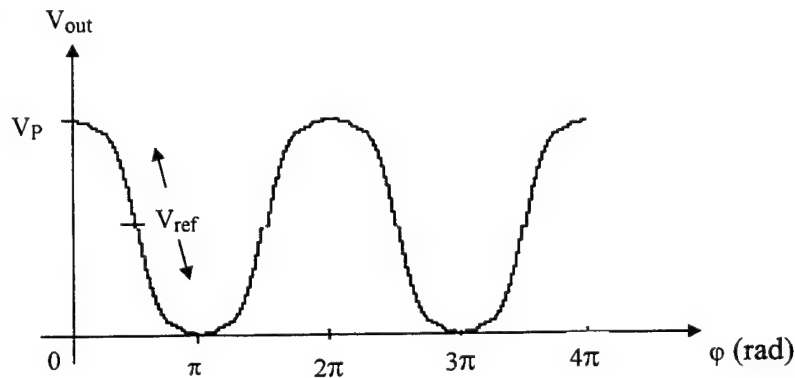


Figure 86 Initial operating point of the sensor.

If the direction of the external applied magnetic field is opposite to that of the biasing field, the overall magnetic field applied to the sensor decreases and so does the length of the metglas wire. Thus, the phase difference between the first and second reflection increases. If the sensor operates at the point shown in Figure 86, the output voltage falls below the reference voltage. In case the direction is the same as that of the biasing field, the output voltage goes above the reference voltage. Thus, the direction of the applied magnetic field can be easily determined.

From the results obtained in the first part of the experiment the sensors which show the above response are identified. These are generally the sensors operating around the middle of the fringe output. One sensor from each pair is Thus, used to determine the direction of the external applied magnetic field along that particular axis. This information was used to modify the application program driving the microprocessor-based signal demodulation system. In the second part of the experiment, the signal demodulation system displayed the overall output corresponding to each axis after performing various operations on individual sensor outputs in each pair. The magnetic field was again varied from $-40,000$ nT to $40,000$ nT in steps and the displayed output was recorded. The calibration curve (displayed output vs. external applied magnetic field) was plotted for each sensor pair. These results are also presented in the following section.

5.3 Experimental Results

The plots showing the results of the experiments described above are presented below. Figures. 87a and 87b show the low-field and high-field response of sensor 3 respectively. As can be seen from the figures, the low-field response is more linear than the high-field response. This is because although the sensor operates in the linear range of the fringe at lower field strengths, at higher fields the region of operation is no longer linear. This effect is more clearly visible in some of the plots presented later.

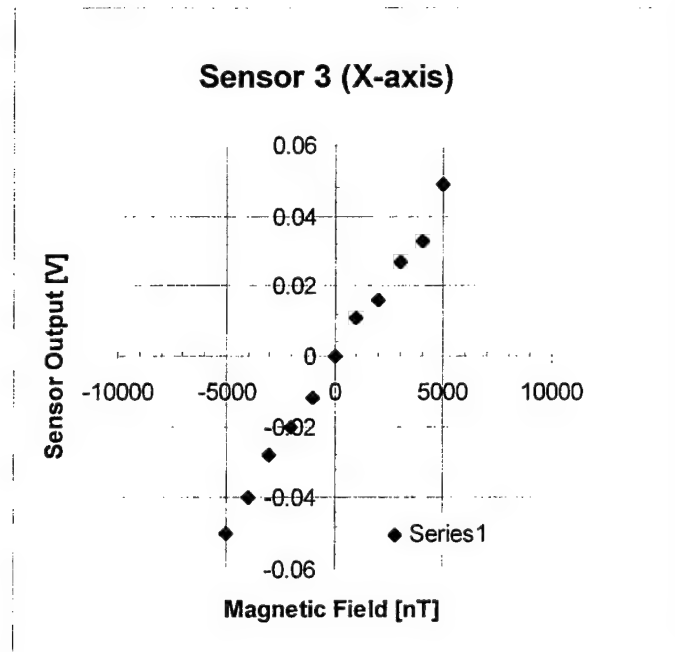


Figure 87a Low field response of sensor 3 (X-axis).

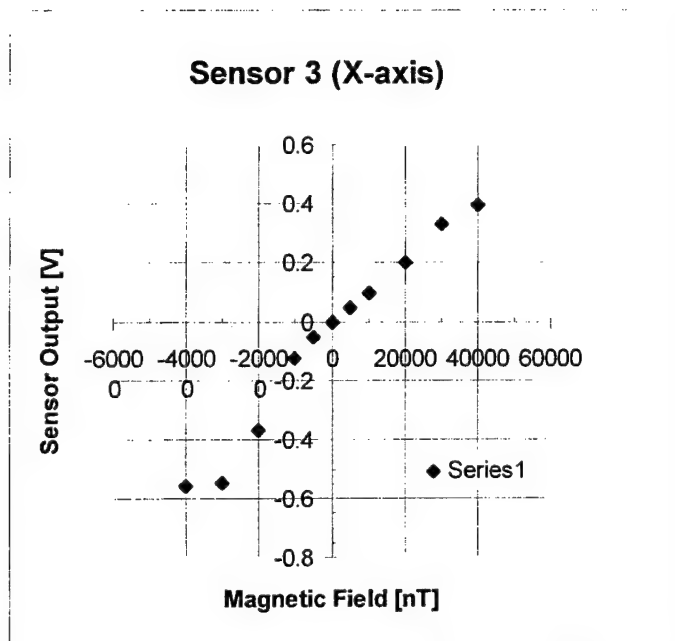


Figure 87b High field response of sensor 3 (X-axis).

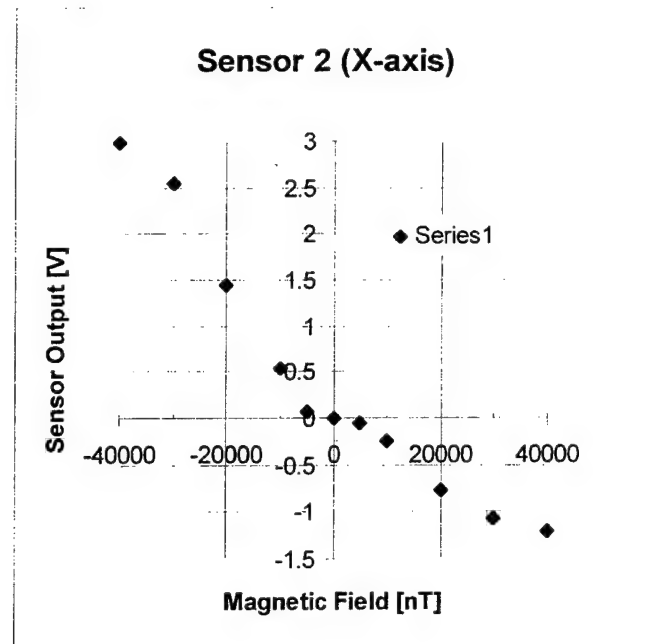


Figure 88 Field response of sensor 2 (X-axis).

As can be seen in Figure 88, sensor 2 does not show a good low field response. Since the initial operating point of this sensor is 90° out of phase with that of sensor 3, it operates either near the top or the bottom of the fringe and Hence, shows extremely low sensitivity. The plot also indicates that the operating point is not exactly at the bottom or top. If this were the case, the output voltage variation on application of positive and negative magnetic fields would be in the same direction.

Figures 89a and 89b show the magnetic field response of sensor 4. As can be seen from the figures, the response is exactly opposite to that shown by sensor 3. The direction of voltage variation depends not only on the operating point along the fringe but also on the slope of operation. Sensor 4, though operating near the center (as can be seen from the linear low-field response), operates on the other side of the fringe (similar to sensor 2) and Hence, shows an output variation exactly opposite of that shown by sensor 3.

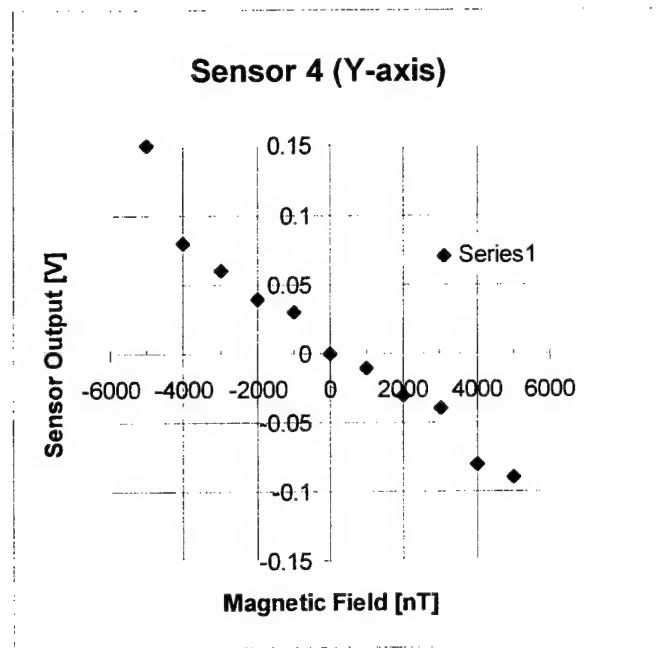


Figure 89a Low field response of sensor 4 (Y-axis).

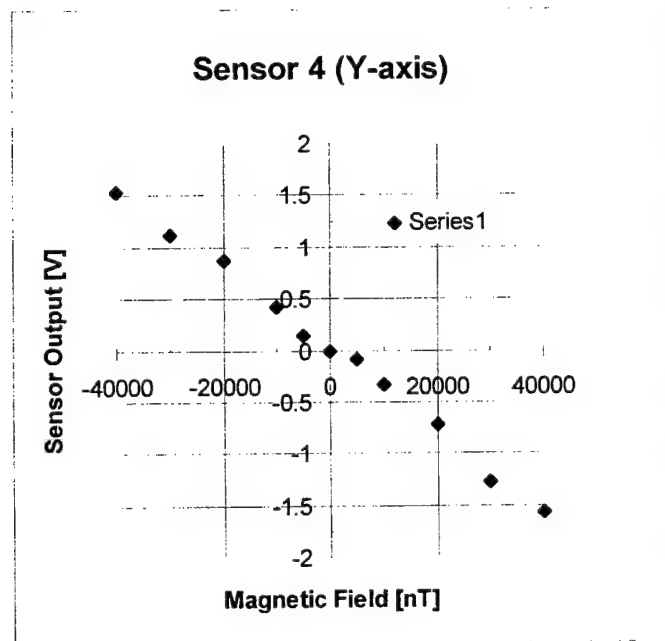


Figure 89b High field response of sensor 4 (Y-axis).

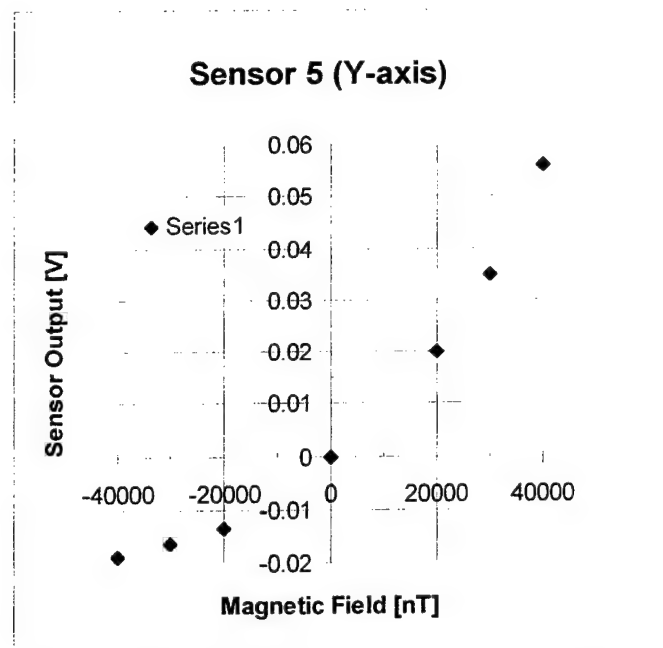


Figure 90 Field response of sensor 5 (Y-axis).

As can be seen in Figure 90, sensor 5 exhibits a response similar to that shown by sensor 2. It operates either near the bottom or the top of the fringe and Hence, shows extremely low sensitivity. Like sensor 2, the operating point is not exactly at the peak. However, the slope of operation is similar to that of sensor 3.

Figures. 91a and 91b, and Figures. 92a and 92b show the low-field and high-field response of sensors 6 and 7 respectively. As can be seen from the figures, both the sensors show visibly non-linear response even for low fields. The sensors, though in quadrature with each other, operate near the top and bottom of the fringe and Thus, in the non-linear region of operation. Hence, the non-linear response.

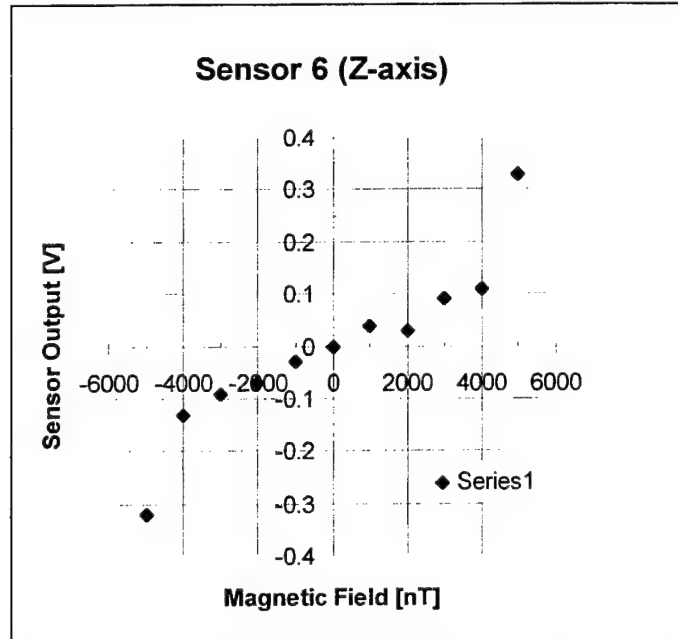


Figure 91a Low field response of sensor 6 (Z-axis).

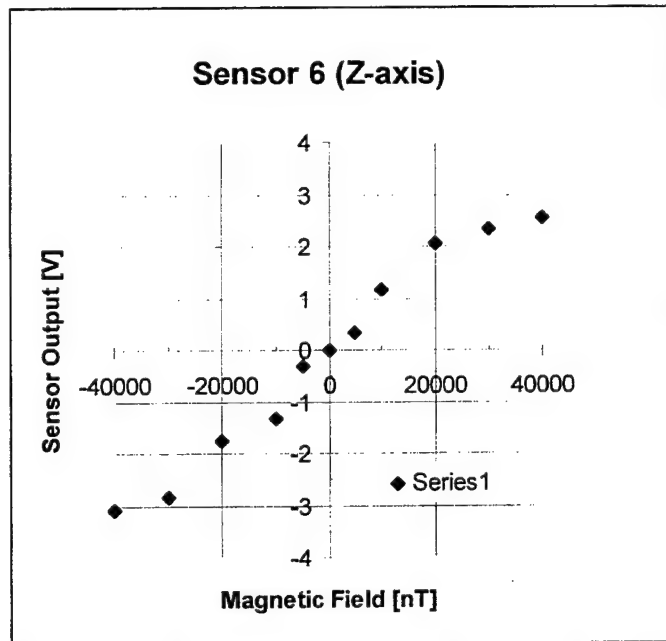


Figure 91b High field response of sensor 6 (Z-axis).

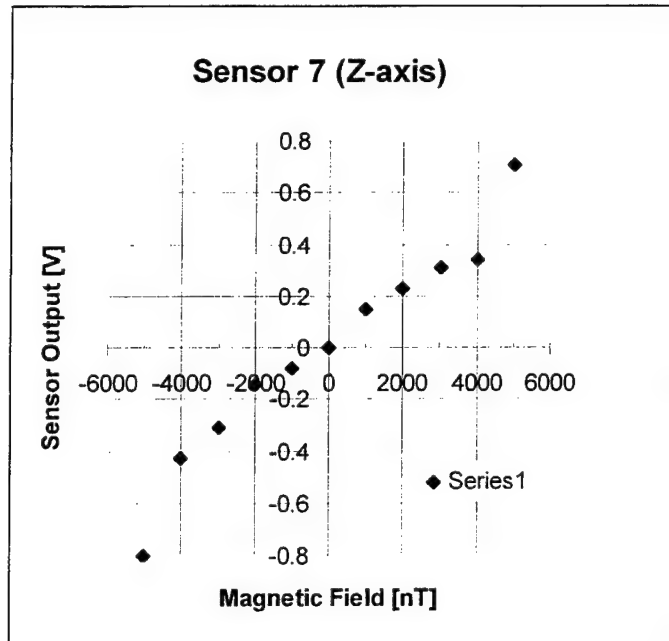


Figure 92a Low field response of sensor 7 (Z-axis).

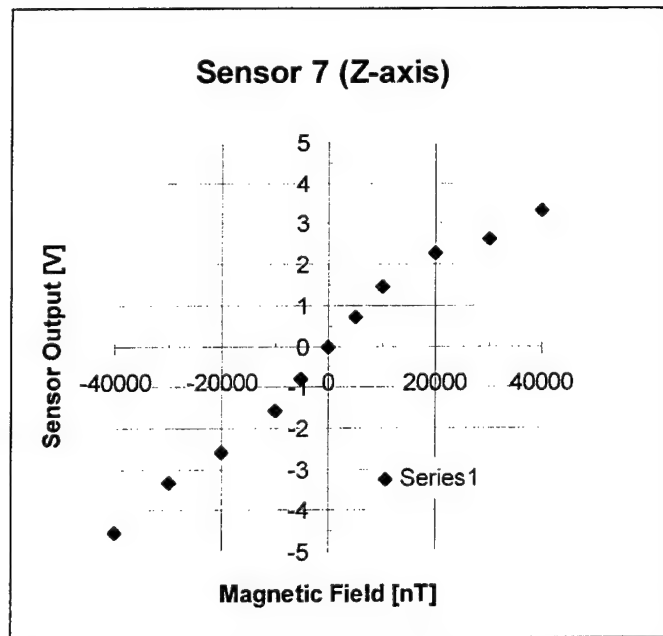


Figure 92b High field response of sensor 7 (Z-axis).

Figures 93-95 show the calibration curves for the X, Y and Z axes of the magnetometer system. The figures show the output calculated by the signal demodulation system, plotted against the applied external magnetic field. All the calibration curves exhibit a certain level of non-linearity

which can be attributed to the non-uniform response of the individual sensors to the same external applied field. That is, the quadrature phase relation between the two sensors of a pair is not maintained over the entire range of operation.

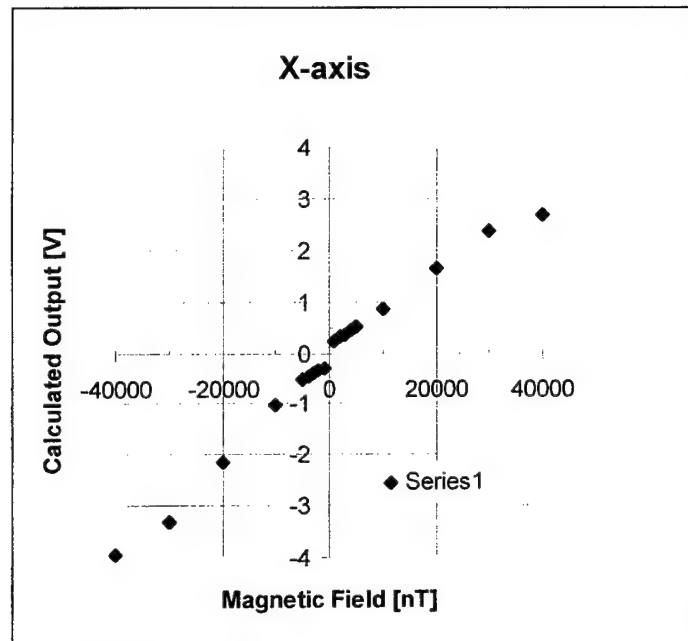


Figure 93 Calibration curve for X-axis.

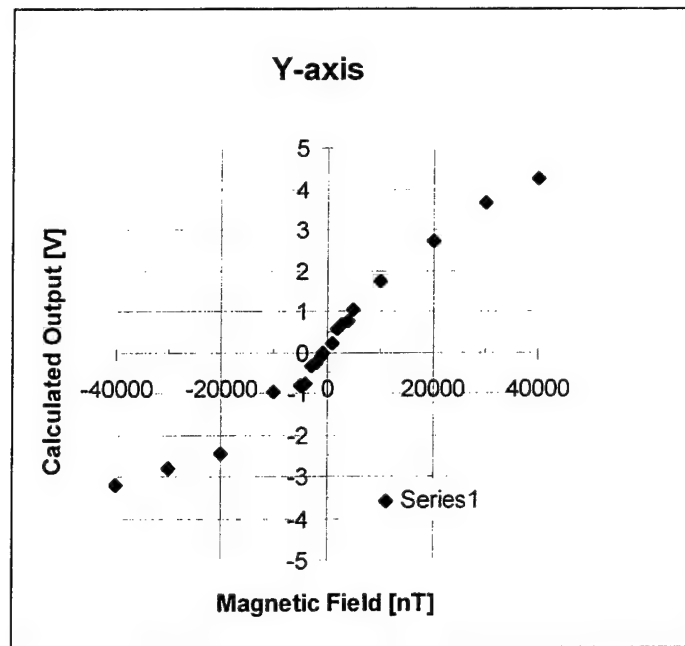


Figure 94 Calibration curve for Y-axis.

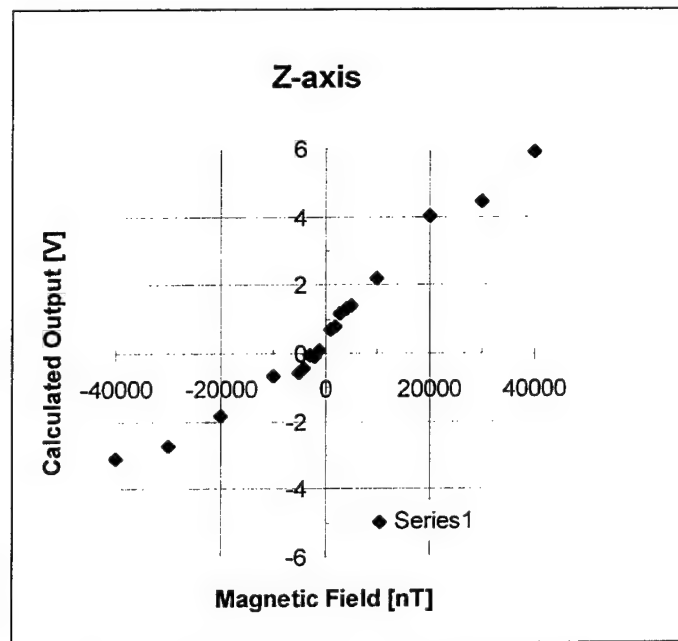


Figure 95 Calibration curve for Z-axis.

After finishing the first calibration which allows measuring sensor output voltages corresponding to applied magnetic field, a second stage calibration is performed to represent measured magnetic field on the display in the microprocessor based signal demodulation system. In the second stage calibration, the value of each axis for applied field and sensor output voltage is converted as an inverse function, i.e., in Figure 95, x-axis (magnetic flux applied) is set to y-axis and y-axis(sensor output voltage) is set to x-axis. After doing this, a 4th order polynomial curve fit is performed. By getting and applying mathematical expression for data points, the sensor response is directly represented as magnetic flux (nT) on the system display and system linear response is increased. The results with this curve fitting based calibration are shown in Figure 96-101. In these figures, the x-axes are applying magnetic fields and y-axes are actual system measurement output read on the system display. The mathematical expression for curve fitted calibration was programmed in C⁺⁺ program(system.cpp). This microprocessor based signal demodulation system enables utilizing curve fitting based calibration without using complex analog computing circuitry which uses many analog dividers and multipliers. Since the calculations for quadrature signal demodulation and output(magnetic flux) from 4th order fitted curve are done in digital domain, the accuracy of system output was increased.

In Figure 96, the first row of the figures is the sensor output voltage corresponding to applied calibration magnetic fields. The second row of the figure shows converting the axes, and '*' are converted data points and 'o' are 4th order curve fitted points. This is the first stage of calibration. At this stage, coefficients for mathematical expression are obtained with this method. Figure 97 shows the final system calibration curve based on the curve fitting method for x-axis. Even though the sensor output is not linear, the curve fitting based system calibration shows linear output in final representation. The other axes are calibrated by using the same method.

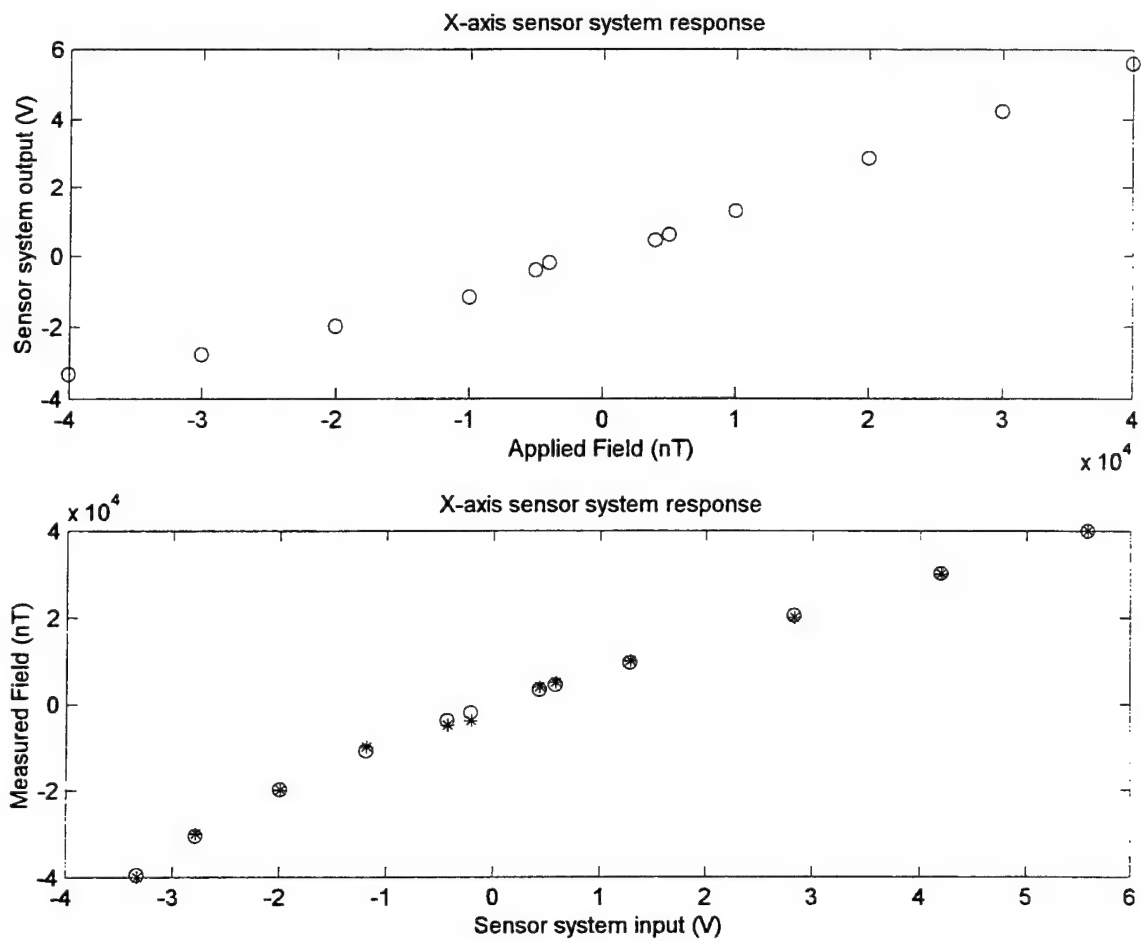


Figure 96 First stage of system calibration for X-axis.

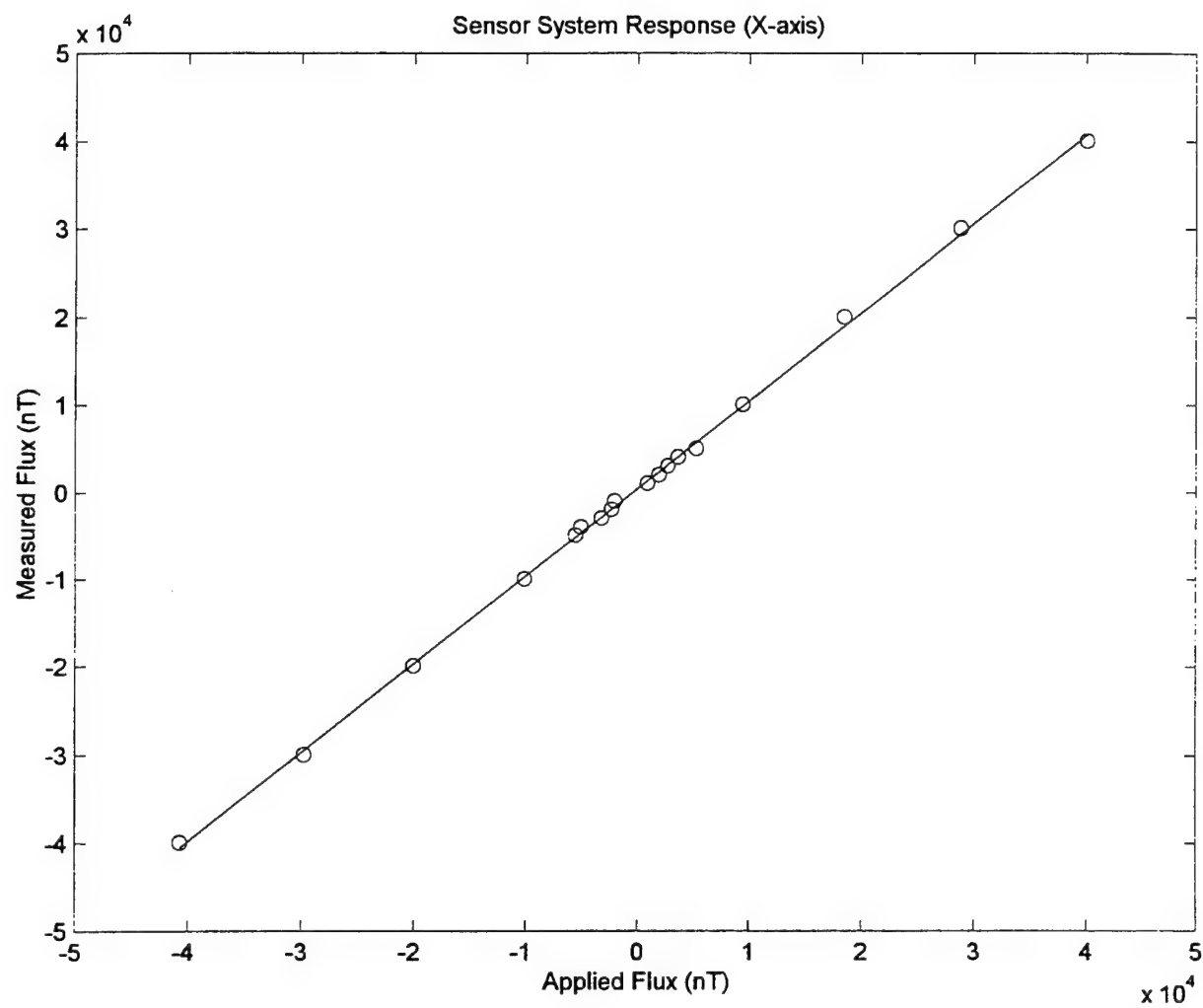


Figure 97 Second stage of system calibration for X-axis (Final system output representation).

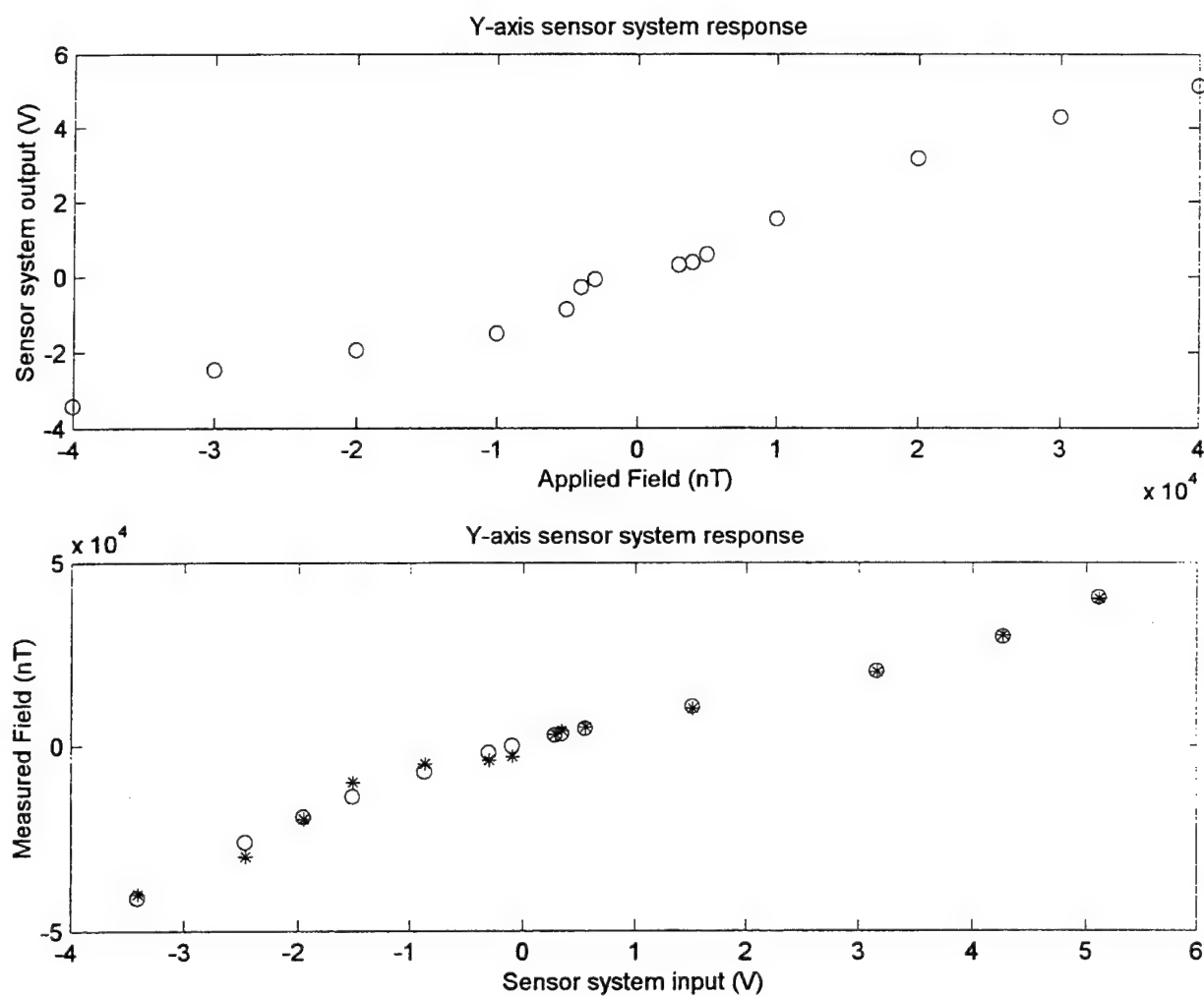


Figure 98 First stage of system calibration for Y-axis.

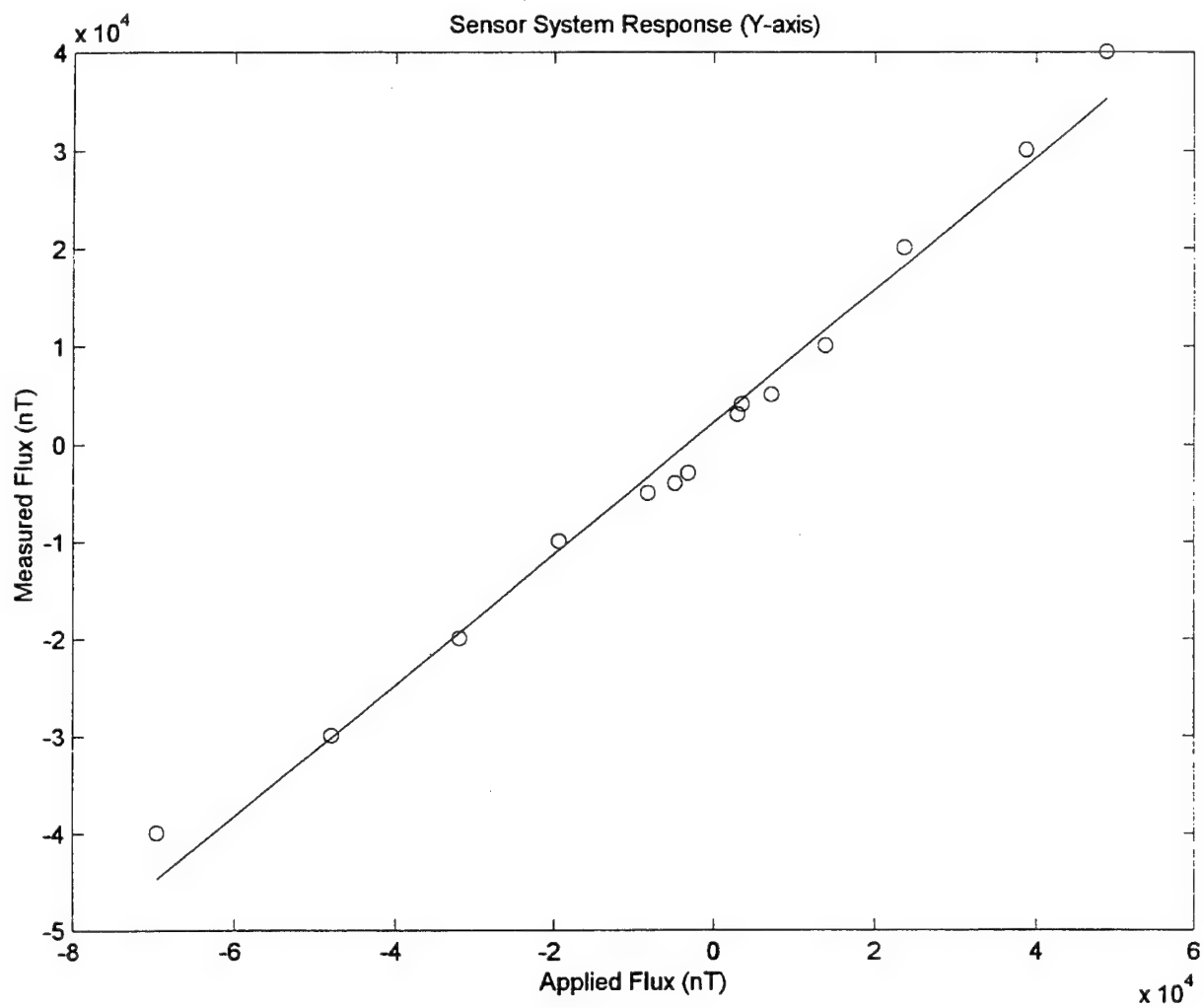


Figure 99 Second stage of system calibration for Y-axis (Final system output representation).

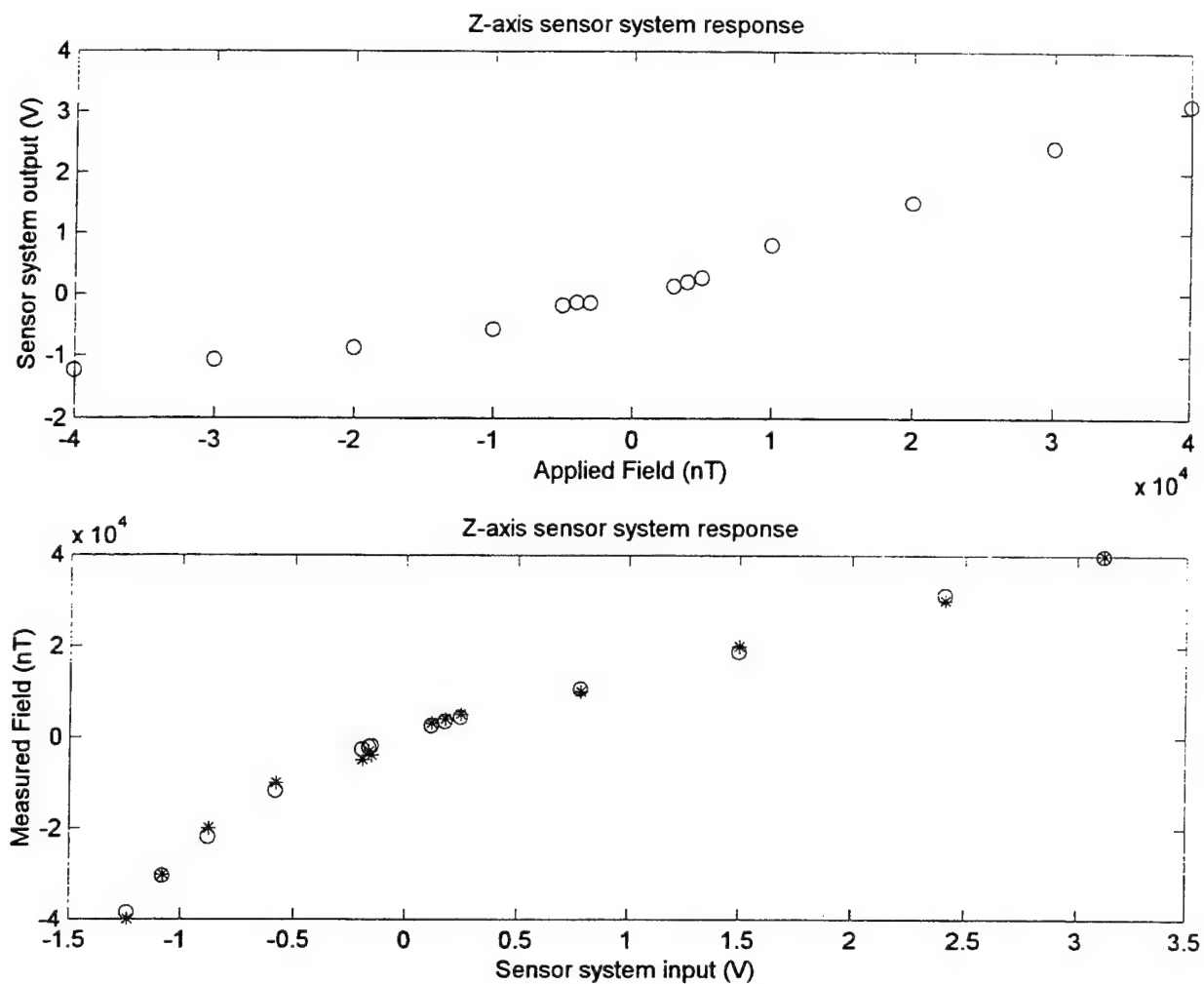


Figure 100 First stage of system calibration for Z-axis.

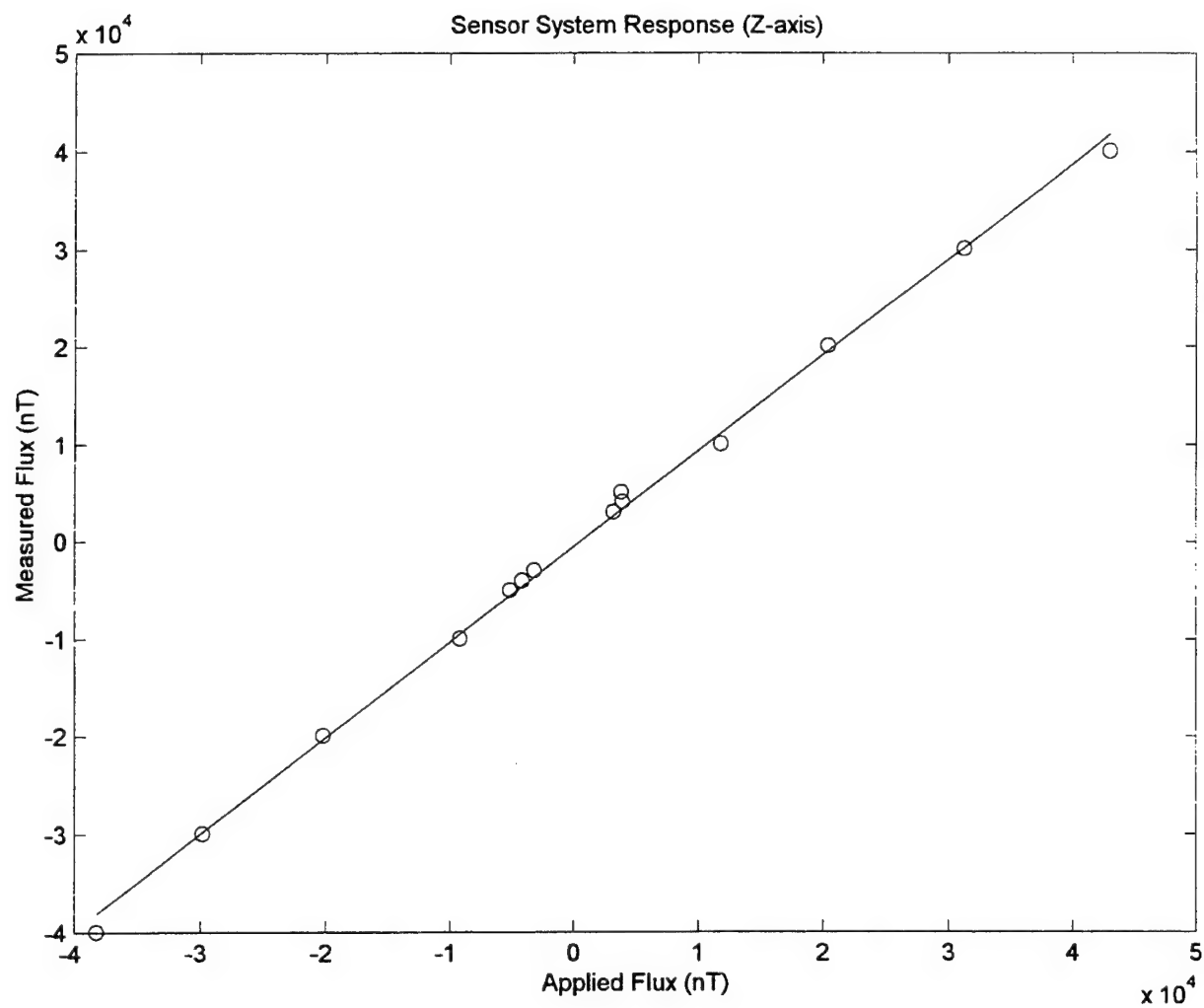


Figure 101 Second stage of system calibration for Z-axis (Final system output representation).

Chapter 6: Conclusion

A simple, compact, highly sensitive, and well temperature compensated EFPI magnetic field sensor system has been proposed, designed, fabricated and tested. The sensor incorporates magnetostrictive transducer materials on the sensor elements. The candidate magnetostrictive materials were evaluated by experimental and theoretical methods. The Metglas wire was found to be suitable for low magnetic field measurements because of its high sensitivity and geometrical advantage in fabricating temperature stabilized sensors. A modified EFPI-based configuration was designed and implemented using the magnetostrictive Metglas materials as the reflector/target fiber in the Fabry-Perot cavity. This new sensor design has shown high sensitivity, optimal quadrature point stabilization, and increased immunity to ambient vibrations.

A field annealing system was implemented for increasing the sensitivity of the magnetostrictive material and straightening the magnetostrictive sensor elements. An order of magnitude improvement was obtained after the transverse field annealing in the fiber magnetometer detection sensitivity. A robust temperature compensation method was realized by solving the simultaneous equations for CTEs of the sensor materials for the given geometry and further improvement was achieved by a mathematical approach to determine accurate compensator length. The temperature compensation was achieved up to 98 % by these methods. The fringe visibility of the sensor system was enhanced up to 92 % by modification of end face of the sensor gage. The Quadrature-Phase-Shift (QPS) signal demodulation system was implemented. This technique ensures the accurate detection of the phase of the demodulated signal, regardless of the initial phase of the EFPI sensor. Two sensor elements, operating in quadrature with respect to each other, yield unambiguous strain information that is correlated to the magnitude of the weak magnetic field through the magnetostriction coefficient. One-dimensional magnetometer was implemented and tested by utilizing the results of the methods. Based on the one-dimensional magnetic field sensor system, 3- dimensional vector field measuring system was proposed. In order to further enhance the system performance, a new temperature compensation/signal demodulation method was proposed. To maintain high sensitivity, the reduction of packaging-induced strain is essential for optimal sensor

operation. Most strain comes from bending of input fiber at the sensor end. Since the fiber is a solid glass rod in microscopic view and continuous body, even epoxying input fiber to compensator tube does not prevent slight moving of the input fiber in an EFPI. Hence, slight bending of input fiber end at the starting point of the sensor gage causes output instability. There are several methods to reduce the axial strain due to fiber bending. One of the ways is to arrange sensor gage pairs in larger orthogonal space. This prevents input fiber bending at the sensor gage starting point. The other way is using bare single mode fiber instead of using jacketed fiber. The strain after epoxying the protective inner jacket to bare fiber also causes small strain when the jacketed fiber side experiences bending. Since the sensor gage input fiber can be treated cautiously, the protective jacket may not be needed and the bare fiber itself has strong polymer coating on it. The extreme shearing or torsional forces may break the bare fiber. Hence, by using the bare fiber the overall strain in the sensor gage can be reduced. The other concern is system calibration. Since FEORC does not equip magnetic field shield rooms, it is difficult to calibrate the sensor system to the reference value, i.e., making each zero magnetic field response in x,y and z direction. Also the earth magnetic flux is varying from few nT to hundreds nT with time interval of seconds to hours in a day. Hence, a shielded condition is needed for accurate calibration. In addition to strain and ambient magnetic field fluctuation, temperature-induced length variation of Metglas wire also causes instability of sensor output.

One of the major difficulties in the fabrication of the passive temperature compensated sensors was the cutting of the compensator tube. The other source of the error is the spreading of epoxy in the sensor ends to fix the fiber and sensor gage to the compensator tube. The control of the epoxy spreading is limited to 0.5 mm. To overcome this problem, one end of final system sensors were fusion spliced but the accuracy there is still limited to 0.25 mm. Thus, the eventual accuracy is limited to 0.5 mm in compensator tube length. The other source of instability is temperature variation rate to the sensors. The time rate change of temperature should be slow to ensure that the body temperature each material in the sensor is the same. But this factor is hardly satisfied in uncontrolled situation. Although 98 % of temperature compensation has been achieved,

for 100 nT measurement, 99.9948 % of temperature compensation is needed. The sensor Q-point can hardly be kept in the middle point of fringe. Since the quarter fringe variation is equivalent to $0.1625\text{ }\mu\text{m}$ in air-gap change, small exterbance can disturb adjusted Q-point. Even though microprocessor based signal demodulation is applied, the trans-impedance amplifier for photodetector generates about 50 mV noise mainly due to power supply noise where regulation of the power source is 1 % for $\pm 15\text{ V}$.

If the laser source wavelength is $1.325\text{ }\mu\text{m}$, then applying 0.4 G produces $0.09\text{ }\mu\text{m}$ change in air-gap with magnetostrictive coefficient of 5 ppm/G and Meglas gage length of 4.5 cm. For 100 nT magnetic flux, the air-gap change is $0.000225\text{ }\mu\text{m}$. If the sensor system operates of $10\text{ }^{\circ}\text{C}$ temperature variation, the unit change of the air-gap should be smaller than $0.0000225\text{ }\mu\text{m}/^{\circ}\text{C}$, which is 0.00225 % in $10\text{ }^{\circ}\text{C}$ change while sensor fabricating accuracy is 0.5 mm for 70 mm long compensator tube, which is 0.71 %. The compensator tube length accuracy required including cutting and epoxy spreading for 100 nT measurement is 0.0057 %. Hence, the minimum detectable magnetic flux limited by fabricating accuracy is 0.12 G for $10\text{ }^{\circ}\text{C}$ temperature variation. In order to improve minimum detectable magnetic flux density, if the fabricating accuracy can be increased from 0.5 mm to 0.25 mm and sensor gage actual temperature variation can be maintained within $1\text{ }^{\circ}\text{C}$, the improving factor is 20. Hence, the minimum detectable magnetic flux is 600 nT. Since this value is ensured regardless of measurement time duration, the measurement of 100 nT for a short time duration is possible. A microprocessor based signal demodulation system is implemented and curve fitting based calibration method used to enhance system linear response. For future direction, we propose the other way to stabilize sensor, which was briefly discussed in the previous Quarterly report. The new method is utilizing a magnetic feedback to compensate the Q point change due by thermal fluctuation and external field to be measured. Since the same amount of feedback voltage induced by thermal or magnetic exterbances is generated, the effect of hysteresis on the sensor gage can be reduced. Overall sensor system output in conjunction with passive temperature compensation scheme implemented here can be well stabilized with simple supporting circuitry. This method ensures a compact, simple, yet reliable measurement of 3-dimensional vector magnetic field for space application.

In conclusion, we have demonstrated fiber optic sensors based on an extrinsic Fabry-Perot Interferometer to measure 3-dimensional DC vector magnetic field from 0 to 0.4 Oe with resolution of 100 nT by realizing temperature stabilization, reduction in vibration sensitivity, improving fringe visibility, enhancing magnetostriction using high field transverse field annealing and new material, and compact sensor packaging for space applications.

References

- [1.1] J. D. Livingstone, "Magnetomechanical properties of Amorphous Materials," *Phys. Status. Solidi*, vol. 70, pp. 591-596, 1982.
- [1.2] A.E. Clark, *AIP Conference Proc.*, no. 18, Part2, pp. 1015-1029, 1973.
- [1.3] T.R. Anantharman, *Metallic Glasses*, *Trans Tech Pub.* 1984.
- [1.4] F. Bucholtz et al, "Easy axis distribution in transversely annealed Metglas 2605 S2," *J. of Magnetism & Magnetic Mat.*, pp. 1607-1608, 1986.
- [2.1] D. Askeland , "The Science and Engineering of Materials," PWS-KENT, Ch.19, 2nd Ed., 1989.

Appendix

Trans-impedance Amplifier



Low Power, Low Noise
Precision FET Op Amp

AD795

FEATURES

Low Power Replacement for Burr-Brown
OPA-111, OPA-121 Op Amp and TI TLC 2201

Low Noise

2.5 $\mu\text{V p-p}$ max, 0.1 Hz to 10 Hz
10 nV/ $\sqrt{\text{Hz}}$ max at 10 kHz
0.6 fA/ $\sqrt{\text{Hz}}$ at 1 kHz

High DC Accuracy

250 μV max Offset Voltage
1 $\mu\text{V}/^\circ\text{C}$ max Drift
1 pA max Input Bias Current

114 dB Open-Loop Gain

Available in Plastic Mini-DIP, 8-Pin Header and Surface
Mount (SOIC) Packages

Dual Version AD796 also Available

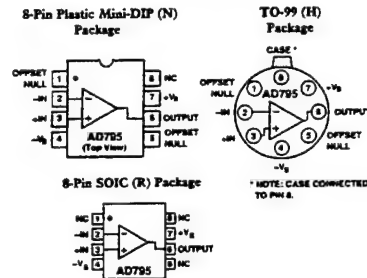
APPLICATIONS

Low Noise Photodiode Preamps

CT Scanners

Precision I-to-V Converters

CONNECTION DIAGRAMS



AD795—SPECIFICATIONS (@ +25°C and $\pm 15\text{ V dc}$, unless otherwise noted)

Parameter	Conditions	AD795J/A Min	AD795J/A Typ	AD795J/A Max	AD795K/B Min	AD795K/B Typ	AD795K/B Max	AD795S Min	AD795S Typ	AD795S Max	Units
INPUT OFFSET VOLTAGE¹											
Initial Offset	$T_{\text{MIN}}-T_{\text{MAX}}$	100		500	50		250	100		500	μV
Offset	$T_{\text{MIN}}-T_{\text{MAX}}$	300		1000	100		400	300		1500	μV
vs. Temperature		3		105	2		3/1	4		10	$\mu\text{V}/^\circ\text{C}$
vs. Supply		90		110	94		110	90		110	dB
vs. Supply (PSRR)	$T_{\text{MIN}}-T_{\text{MAX}}$	100			90		100	86		95	dB
INPUT BIAS CURRENT¹											
Either Input	$V_{\text{CM}} = 0\text{ V}$	1		2	1		1	1		4	pA
Either Input @ T_{MAX}	$V_{\text{CM}} = 0\text{ V}$	2364			2364			1000			pA
Either Input	$V_{\text{CM}} = +10\text{ V}$	1			1			1			pA
Offset Current	$V_{\text{CM}} = 0\text{ V}$	0.1		1.0	0.1		0.5	0.1		1.0	pA
Offset Current @ T_{MAX}	$V_{\text{CM}} = 0\text{ V}$	2/6			2/6			100			pA
INPUT VOLTAGE NOISE											
	0.1 Hz to 10 Hz	1.0		3.3	1.0		2.5	1.0		3.3	$\mu\text{V p-p}$
	$f = 10\text{ Hz}$	20		50	20		40	20		50	nV/ $\sqrt{\text{Hz}}$
	$f = 100\text{ Hz}$	10		30	10		20	10		30	nV/ $\sqrt{\text{Hz}}$
	$f = 1\text{ kHz}$	9		15	9		10	7		15	nV/ $\sqrt{\text{Hz}}$
	$f = 10\text{ kHz}$	8		10	8		10	8		10	nV/ $\sqrt{\text{Hz}}$
INPUT CURRENT NOISE											
	$f = 0.1\text{ Hz to }10\text{ Hz}$	13			13			13			fA p-p
	$f = 1\text{ kHz}$	0.6			0.6			0.6			fA/ $\sqrt{\text{Hz}}$
FREQUENCY RESPONSE											
Unity Gain, Small Signal	$G = -1$	1.6			1.6			1.6			MHz
Full Power Response	$V_O = 20\text{ V p-p}$	16			16			16			kHz
Slew Rate, Unity Gain	$R_{\text{LOAD}} = 20\text{ V p-p}$	1			1			1			V/ μs
	$R_{\text{LOAD}} = 2\text{ k}\Omega$										
SETTLING TIME²											
To 0.1%		6			6			6			μs
To 0.01%		8			8			8			μs
Overload Recovery ³	50% Overdrive	5			5			5			μs
Total Harmonic Distortion	$f = 1\text{ kHz}$										%
	$R_I \approx 2\text{ k}\Omega$										
	$V_O = 3\text{ V rms}$	0.0006			0.0006			0.0006			%
INPUT IMPEDANCE											
Differential	$V_{\text{DIFF}} = \pm 1\text{ V}$	$10^{11}\Omega$			$10^{11}\Omega$			$10^{11}\Omega$			Ω/pF
Common Mode		$10^{12.2}\Omega$			$10^{12.2}\Omega$			$10^{12.2}\Omega$			Ω/pF
INPUT VOLTAGE RANGE											
Differential ³		± 20			± 20			± 20			V
Common-Mode Voltage		± 10		± 11	± 10		± 11	± 10		± 11	V
Over Max Operating Range	$V_{\text{CM}} = \pm 10\text{ V}$	± 10			± 10			± 10			V
Common-Mode Rejection Ratio	$T_{\text{MIN}}-T_{\text{MAX}}$	90		110	94		110	86		110	dB
		100			100			100			dB
OPEN-LOOP GAIN											
	$V_O = \pm 10\text{ V}$	120			120			120			dB
	$R_{\text{LOAD}} \approx 10\text{ k}\Omega$	100		108	100		108	100		108	dB
	$R_{\text{LOAD}} \approx 2\text{ k}\Omega$										dB
	$T_{\text{MIN}}-T_{\text{MAX}}$										dB
OUTPUT CHARACTERISTICS											
Voltage	$R_{\text{LOAD}} \approx 2\text{ k}\Omega$	± 10		± 11	± 10		± 11	± 10		± 11	V
	$T_{\text{MIN}}-T_{\text{MAX}}$	± 10			± 10			± 10			V
Current	$V_{\text{OUT}} = \pm 10\text{ V}$	± 5		± 10	± 5		± 10	± 5		± 10	mA
	Short Circuit	± 15			± 15			± 15			mA
POWER SUPPLY											
Rated Performance		± 15			± 15			± 15			V
Operating Range		± 5		± 18	± 5		± 18	± 5		± 18	V
Quiescent Current		1.2		1.5	1.2		1.5	1.2		1.5	mA



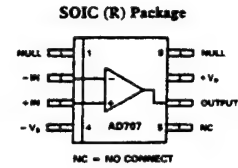
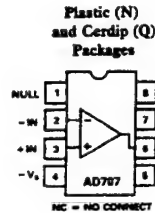
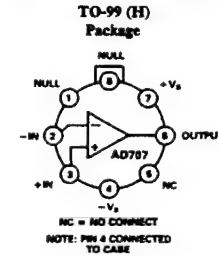
Ultralow Drift Op Amp

AD707

FEATURES

Very High DC Precision
 15 μV max Offset Voltage
 0.1 $\mu\text{V}/^\circ\text{C}$ max Offset Voltage Drift
 0.35 μV p-p max Voltage Noise (0.1 Hz to 10 Hz)
 8 $\text{V}/\mu\text{V}$ min Open-Loop Gain
 130 dB min CMRR
 120 dB min PSRR
 1 nA max Input Bias Current
 AC Performance
 0.3 $\text{V}/\mu\text{s}$ Slew Rate
 0.9 MHz Closed-Loop Bandwidth
 Dual Version: AD708
 Available in Tape and Reel in Accordance with
 EIA-481A Standard

CONNECTION DIAGRAMS



AD707—SPECIFICATIONS (@ +25°C and $\pm 15\text{ V}$ dc, unless otherwise noted)

Conditions	AD707J/A	AD707K/B/S	AD707C/T	Units
INPUT OFFSET VOLTAGE				
Initial	30	10	5	μV
vs. Temperature	0.3	0.1	0.03	$\mu\text{V}/^\circ\text{C}$
Long-Term Stability	50	15	7/8/5	μV
Adjustment Range	0.3	0.3	0.2	$\mu\text{V}/\text{month}$
	± 4	± 4	± 4	mV
INPUT BIAS CURRENT				
T_{min} to T_{max}	1.0	0.5	0.5	nA
	2.5	1.5	1.0	nA
Average Drift	4.0	3.8	2.8	nA
	15	15	10	pA/°C
OFFSET CURRENT				
$V_{\text{CM}} = 0\text{ V}$	0.5	0.3	0.1	nA
T_{min} to T_{max}	2.0	1.0	0.2	nA
Average Drift	4.0	2.8	1.5	nA
	2	1	1	pA/°C
INPUT VOLTAGE NOISE				
0.1 to 10 Hz	0.23	0.23	0.23	μV p-p
$f = 10\text{ Hz}$	10.3	10.3	10.3	nV/√Hz
$f = 100\text{ Hz}$	10.0	10.0	10.0	nV/√Hz
$f = 1\text{ kHz}$	9.6	9.6	9.6	nV/√Hz
INPUT CURRENT NOISE				
0.1 Hz to 10 Hz	14	14	14	pA p-p
$f = 10\text{ Hz}$	0.32	0.32	0.32	pA/√Hz
$f = 100\text{ Hz}$	0.14	0.14	0.14	pA/√Hz
$f = 1\text{ kHz}$	0.12	0.12	0.12	pA/√Hz
COMMON-MODE REJECTION RATIO				
$V_{\text{CM}} = \pm 15\text{ V}$	120	130	130	dB
T_{min} to T_{max}	140	140	140	dB
OPEN-LOOP GAIN				
$V_{\text{O}} = \pm 10\text{ V}$	3	5	8	$\text{V}/\mu\text{V}$
$R_{\text{LOAD}} = 2\text{ k}\Omega$	13	13	13	$\text{V}/\mu\text{V}$
T_{min} to T_{max}	13	13	13	$\text{V}/\mu\text{V}$
$R_{\text{LOAD}} = 1\text{ k}\Omega$	13	13	13	$\text{V}/\mu\text{V}$
POWER SUPPLY REJECTION RATIO				
$V_{\text{S}} = \pm 3\text{ V}$ to $\pm 18\text{ V}$	110	115	120	dB
T_{min} to T_{max}	130	130	130	dB
FREQUENCY RESPONSE				
Closed-Loop Bandwidth	0.5	0.5	0.5	MHz
Slew Rate	0.15	0.15	0.15	$\text{V}/\mu\text{s}$
INPUT RESISTANCE				
Differential	24	45	60	M Ω
Common Mode	100	200	200	G Ω
OUTPUT CHARACTERISTICS				
Voltage				
$R_{\text{LOAD}} = 10\text{ k}\Omega$	13.5	13.5	13.5	$\pm\text{V}$
$R_{\text{LOAD}} = 2\text{ k}\Omega$	12.5	12.5	12.5	$\pm\text{V}$
$R_{\text{LOAD}} = 1\text{ k}\Omega$	12.0	12.0	12.0	$\pm\text{V}$
$R_{\text{LOAD}} = 2\text{ k}\Omega$	12.0	12.0	12.0	$\pm\text{V}$
T_{min} to T_{max}	13.0	13.0	13.0	$\pm\text{V}$
OPEN-LOOP OUTPUT RESISTANCE	60	60	60	Ω
POWER SUPPLY				
Current, Quiescent	2.5	2.5	2.5	mA
Power Consumption, No Load	75	75	75	mW
$V_{\text{S}} = \pm 15\text{ V}$	9.0	9.0	9.0	mW
$V_{\text{S}} = \pm 3\text{ V}$	9.0	9.0	9.0	mW
TEMPERATURE RANGE				
Operating, Rated Performance				
Commercial	0 to +70°C	AD707JN, AD707JR	AD707KN, AD707KR ¹	AD707CQ, AD707CH
Industrial	-40°C to +85°C	AD707AQ, AD707AH	AD707BK, AD707BH	
Military	-55°C to +125°C	AD707AR	AD707SQ, AD707SH	AD707TQ, AD707TH

40-pin Connector for A/D Converter

SINGLE-ENDED CONFIGURATION

BOTTOM ROW TOP ROW

LEFT TO RIGHT

AGND	1	2	VREF
CHNL 0	3	4	CHNL 8
CHNL 1	5	6	CHNL 9
CHNL 2	7	8	CHNL 10
CHNL 3	9	10	CHNL 11
CHNL 4	11	12	CHNL 12
CHNL 5	13	14	CHNL 13
CHNL 6	15	16	CHNL 14
CHNL 7	17	18	CHNL 15
AGND	19	20	+15V
-15V	21	22	DGND
DOUT 0	23	24	DOUT 1
DOUT 2	25	26	DOUT 3
DOUT 4	27	28	DOUT 5
DOUT 6	29	30	DOUT 7
DOUT 8	31	32	DOUT 9
DOUT 10	33	34	DOUT 11
DOUT 12	35	36	DOUT 13
DOUT 14	37	38	DOUT 15
EXT TRG	39	40	DGND

20-pin Connector for LCD Controller

LCD Display

Connector J7 is the only connection needed between the MPC201 and an LCD display. This 20-pin header has the following pinout:

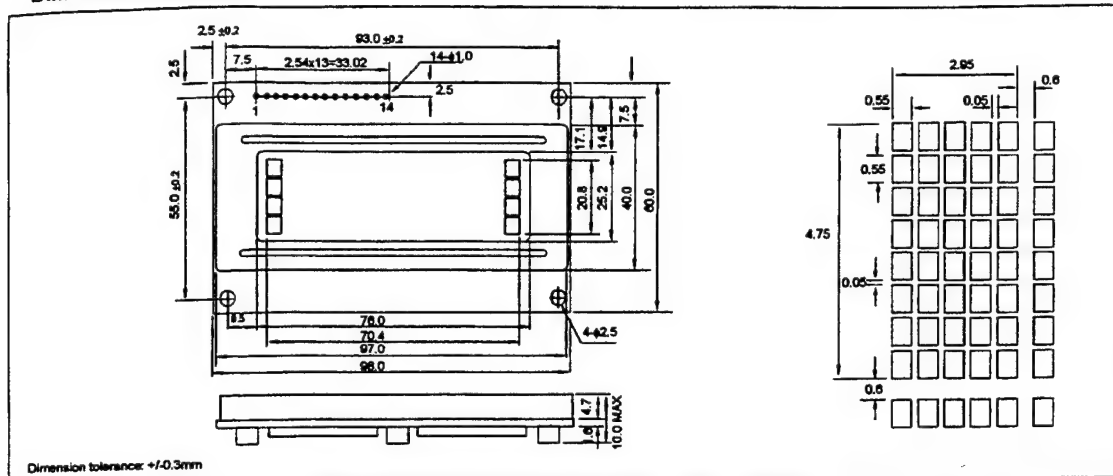
<u>Pin</u>	<u>Signal</u>
1	GND
2	E4
3	GND
4	VCC
5	CONTRAST
6	RS
7	R/W
8	E
9	D0
10	D1
11	D2
12	D3
13	D4
14	D5
15	D6
16	D7
17	E3
18	E2
19	GND
20	N/C

Specifications of LCD Display

HDM20416H

Dimensional Drawing

20 Character x 4 Lines



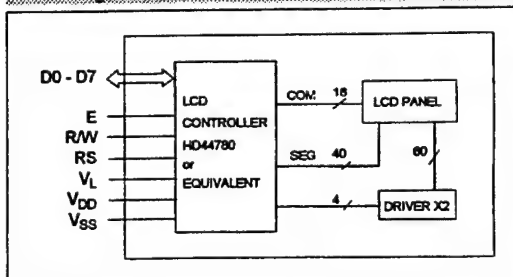
Features

Character Format5x7 Dots with Cursor
Backlight.....EL Optional
Options....TN/Gray STN/Yellow STN, 12 o'Clock/6 o'Clock View
Normal/Extended Temperature
Normal/Negative Displays

Physical Data

Module Size.....98.0W x 60.0H x 10.0T mm
Viewing Area Size.....76.0W x 25.2H mm
Weight.....54g

Block Diagram



Absolute Maximum Ratings

PARAMETER	SYMBOL	MIN	MAX	UNIT
SUPPLY VOLTAGE	$V_{DD}-V_{SS}$	0	7.0	V
SUPPLY VOLTAGE FOR LCD	$V_{DD}-V_L$	0	13.5	V
INPUT VOLTAGE	V_{IH}	V_{SS}	V_{DD}	V
OPERATING TEMPERATURE	T_{OP}	0	50	$^{\circ}\text{C}$
STORAGE TEMPERATURE	T_{STG}	-20	70	$^{\circ}\text{C}$

Electrical Characteristics ($V_{DD}=5.0\pm 0.25\text{V}$ 25 $^{\circ}\text{C}$)

PARAMETER	SYM	CONDITION	MIN	TYP	MAX	UNIT
INPUT HIGH VOLTAGE	V_{IH}	-	2.2	-	-	V
INPUT LOW VOLTAGE	V_L	-	-	-	.06	V
OUTPUT HIGH VOLTAGE	V_{OH}	$I_{OH}=0.2\text{mA}$	2.4	-	-	V
OUTPUT LOW VOLTAGE	V_{OL}	$I_{OL}=1.2\text{mA}$	-	-	0.4	V
POWER SUPPLY CURRENT	I_{DD}	$V_{DD}=5.0\text{V}$	-	1.0	2.2	mA
POWER SUPPLY FOR LCD	$V_{DD}-V_L$	$T_A=25^{\circ}\text{C}$	4.3	-	4.7	V
DRIVE METHOD	1/16 Duty					

Pin Connections

PIN NO.	SYMBOL	LEVEL	FUNCTION
1	V_{SS}	-	0V
2	V_{DD}	-	5V
3	V_L	-	-
4	RS	H/L	H: Data input L: Instruction data input
5	R/W	H/L	H: Data read L: Data write
6	E	H,H \rightarrow L	Enable signal
7	D0	H/L	Data bus
8	D1	H/L	
9	D2	H/L	
10	D3	H/L	
11	D4	H/L	
12	D5	H/L	
13	D6	H/L	
14	D7	H/L	

Specifications of Laser Diode

Serial No: 3090664
 Part No: 823101684 QLM3S823-100
 Date: 13-Oct-93

RAYNET
 86-0023-001-070

SUMMARY CHARACTERISTICS @ 25C

Rated CW output power, P_o (mW):	1.00
Threshold current, I_{th} (mA):	14.4
Modulation Current for rated power, I_m (mA):	19.8
Laser current at rated power, (mA):	34.2
Monitor photo current at rated power, (μ A):	237
Monitor dark current @ -5V (μ A):	0.009
Series Resistance at rated power, (Ohms):	6.4
Change in Power at $I_p = 300$ (μ A) during 20 cycles, -40 to 85 deg. C. (%):	0.0

Spectral Characteristics:

Power (mW)	Freq (MHz)	Wavelength (nm)		Width (nm)	
-----	-----	Peak	Mean	FWHM	RMS
-----	-----	-----	-----	-----	-----
.50	100	1307	1306	3.8	1.4

ELECTRICAL CHARACTERISTICS AT RATED POWER

Laser Temperature (C):	-40	25	85
Threshold current (mA):	7.1	14.4	39.2
Modulation current (mA):	20	20	29
Photo current (μ A):	246	237	232
Power at threshold (μ W):	3		
Voltage at rated power (V):		1.18	

FIBER: Siecor Single-Mode

clad/jacket diameter: 125/900 microns
 color code: solid continuous, yellow

PINOUT CONNECTIONS: 14-Pin DIL "Longhorn"

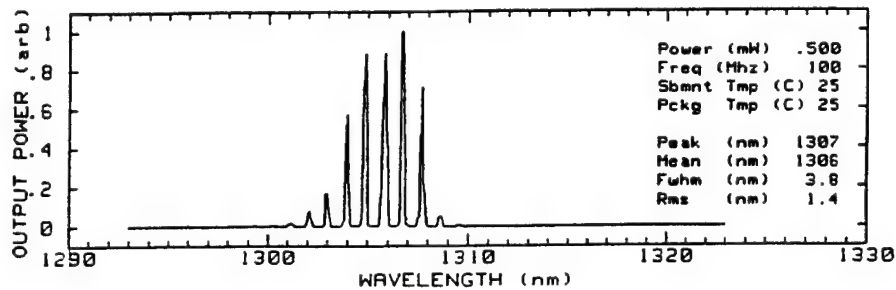
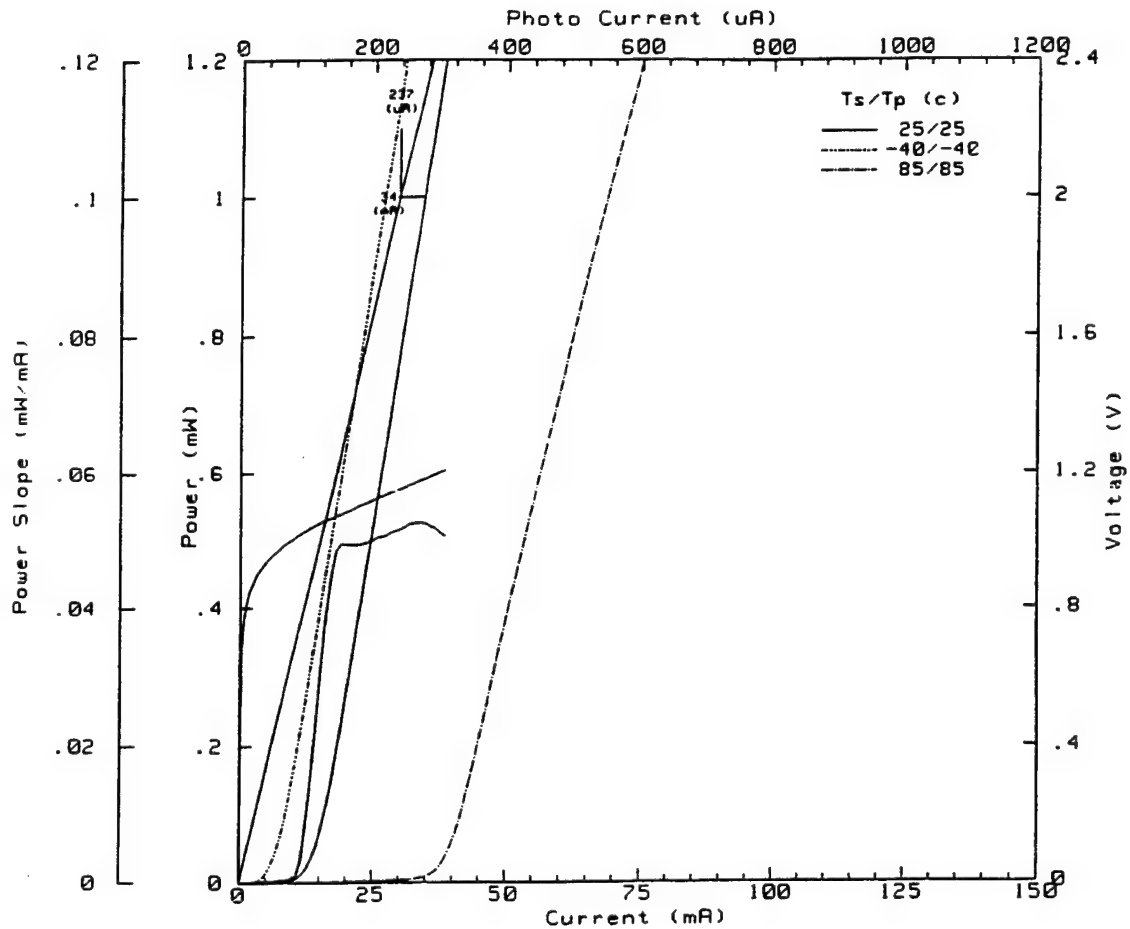
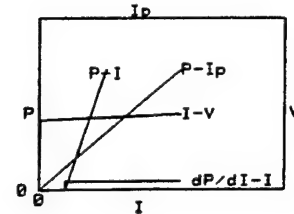
Pin	Connection	Pin	Connection
5	Laser (+), Case Ground	1	---
7	Detector (+), Cathode	2	---
8	Detector (-), Anode	3	---
9	Laser (-)	4	---
10	Laser (+), Case Ground	5	---
		6	---
		7	---

TOP

Note: Optical Power calibrated to Electrically Calibrated
 Pyroelectric Radiometer, traceable to NIST.

Laser Diode Characteristics

Serial # 3090664
 Part Number 823101684
 Model Number QLM3S823-100
 Test Date 13 Oct 1993
 Test Time 08:37:52
 Test Station E
 Test Operator RM



Laser Diode Driver Specifications

LDX-3100 OEM LASER DIODE CURRENT SOURCE

INPUTS

Power Supply: +12 to 18 volts @ 350 mA
-12 to 18 volts @ 50 mA

Control: Output On (Default) when power supplied. User can control output on/off with TTL line

Mode Select³

Jumper Selectable: Constant I / Constant I_{PD}

I Set:

- 1) External Voltage: (0-5V, 50 mA/V)
Bandwidth⁴: 2 kHz
- 2) Internal: 25-turn pot

I Limit Set:

1-turn pot adjustable,
0 to 250 mA (min.)

Photodiode Feedback Type:

Differential, zero-bias

PD Range:

20 μ A to 2 mA

Stability⁵:

$\pm 0.1\%$ (± 0.25 mA)

OUTPUTS

Laser Output

Current: 0 to 250 mA

Compliance Voltage: > 5.5 Volts

Temp. Coefficient: < 50 ppm/ $^{\circ}$ C

Short Term Stability (1 hr.): < 50 ppm

Long Term Stability (24 hr.): < 100 ppm

Control Transients⁶: < 100 μ A

Noise (rms): < 2 μ A

Laser Current Measurement:

0 to 5V

buffered output

Transfer Function:

50 mA/V

Accuracy:

$\pm 0.1\%$ of FS (± 0.25 mA)

Photodiode I Measurement:

0 to 5V

buffered output

Transfer Function:

0.4 mA/V

Accuracy:

$\pm 0.1\%$ of FS (± 2 μ A)

Limit Current Measurement:

0 to 5V buffered output

Transfer Function:

50 mA/V

Accuracy:

$\pm 1.5\%$ of FS (± 3.75 mA)

Laser Diode Protection

ESD: JFET (Normally closed) shorting output

Power: Current Supply regulated onboard, overvoltage protection, transient suppression.

Indicators

Power On: Green LED

Current On: Pads for ext. LED (10 mA)

Error (open circuit): Pads for ext. LED (10 mA)

GENERAL

Size:

Approximately 0.5"x 3.5"x 5.5"
(Printed Circuit Board — includes four 1.25" mounting standoffs)

Operating Temperature:

0 to 50 $^{\circ}$ C

Storage Temperature:

-40 to 70 $^{\circ}$ C

Recommended

Power Supplies:

Tektronix[®] PS280
ELPAC[®] WM113 or WM220-1

NOTES

1. All values measured after a one-hour warm-up period.
2. Isolated control is provided to turn output off and on depending on input (such as TEC error status from LDT-5100). No connection disables this control.
3. Mode may be changed only when output is off.
4. In constant power mode, The bandwidth is reduced to approximately 200 Hz, depending on the photodiode used.
5. Maximum monitor photodiode drift over 30 min. period, after warm up. Assumes zero drift in responsivity of photodiode
6. Maximum output current transient generated from normal operational (ON/OFF) situations

LDX-3100 CONNECTORS

LASER CURRENT,

PHOTODIODE,

I/O CONNECTOR:

9-pin, standard D-sub

1,2 Safety Interlock

3 N/C

4,5 Laser Diode Cathode (-)

6 Photodiode (cathode)

7 Photodiode (anode)

8,9 Laser Diode Anode (+)

POWER INPUT

CONNECTOR:

5-pin, Right-angle,
0.156" centers

1 N/C

2 Earth GND

3 -15 VDC

4 Analog GND

5 +15 VDC

MODULATION INPUT

CONNECTOR:

2-pin, 0.1" centers

ISOLATED CONTROL

CONNECTOR:

3-pin, 0.1" centers

1 ISO VCC

2 N/C

3 ISO CTRL

MEASUREMENT/

CONTROL

CONNECTOR:

10-pin, 0.1" centers,
IDC-compatible

1 Output on

2 Output status

3 +5 V

4 Open circuit error

5 Ground

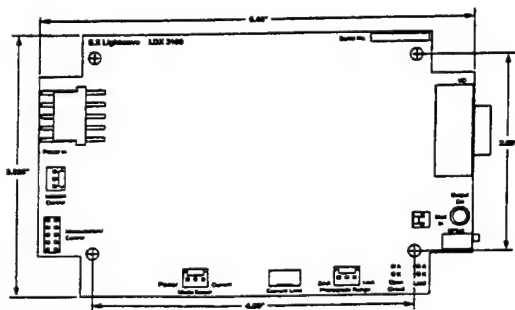
6 Photodiode current monitor

7 Limit sense

8 Limit current monitor

9 Ground

10 Laser current monitor



Single Mode 2x2 Coupler Data

Singlemode Standard Coupler Test Data

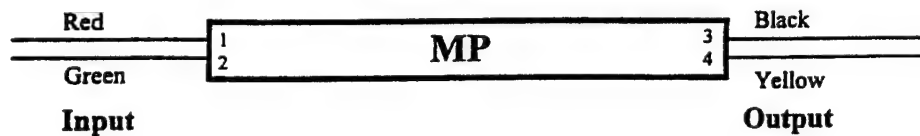
Parts No. : SA13500202BL0NE Ports: 2 x 2

Date: Feb. 24, 1997

TEST DATA:

Serial No.	In	C.R. (%)	I.L. (dB)	Uni. (dB)	E.L. (dB)	Wavelength (nm)	Dir. (dB)	P.D.L. (dB)	Grade
701096	1 2	50	3.0 / 3.2 3.0 / 3.2	0.2 0.2	≤0.15	1310	≥ 65	≤± 0.15	A
701026	1 2	50	3.0 / 3.2 3.0 / 3.2	0.2 0.2	≤0.15	1310	≥ 65	≤± 0.15	A
701094	1 2	50	3.1 / 3.2 3.1 / 3.2	0.1 0.1	≤0.15	1310	≥ 65	≤± 0.15	A
701358	1 2	50	3.0 / 3.3 3.0 / 3.3	0.3 0.3	≤0.15	1310	≥ 65	≤± 0.15	A

Operating Temperature: - 40 °C ~ + 85 °C
Fiber Type: Corning Singlemode Flexcore Fiber



Single Mode 2x2 Coupler Specifications

SINGLEMODE FIBER COUPLER

Applications:

- Long-haul Telecommunications
- Digital, Hybrid and AM-Video Systems
- Local Area Network
- Fiber Sensors
- CATV Systems

Features:

- Low Excess Loss
- Varied Coupling Ratio
- Compact Size
- Excellent Environmental & Mechanical Stability
- Bellcore Standard Compliance
- Top Quality-Price-Ratio

Specifications:

Coupling Ratio (%)	1 ~ 50
Directivity (dB)	≥ 55 dB (For 1x2), ≥ 65 dB (For 2x2)
Thermal Stability (Typ.)(dB)	≤ 0.1
Operating Temperature	-40 °C ~ 85 °C
Storage Temperature	-40 °C ~ 85 °C
Fiber Type	Corning Singlemode SMF-28
Fiber Pigtail Length (m)	0.75 or Custom on Request
Port Configuration	1x2 or 2x2
Package Dimension	Package A, B, C

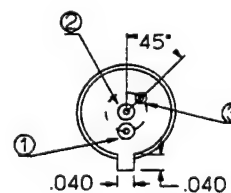
Coupling Ratio (%)	Singlemode Standard Coupler					
	50		30		10	
Grade	A	B	A	B	A	B
Excess Loss (Typical) (dB)	0.1	0.2	0.1	0.2	0.1	0.2
Max. Insertion Loss (dB)	3.4	3.6	1.8/5.6	1.9/5.9	0.7/10.7	0.9/11.5
Uniformity (Max.) (dB)	0.35	0.5				
Polarization Sensitivity (dB)	≤ ±0.1	≤ ±0.1	≤ ±0.15	≤ ±0.15	≤ ±0.15	≤ ±0.2
Operating Wavelength (nm)	850, 1310 and 1550					

InGaAs PIN Photodiode Evaluation Data

Date: 3/4/97

[illegible]

Technical drawing of a probe tip assembly. The drawing shows a cylindrical probe body with a conical tip. A label "strain relief" points to a feature on the body. Dimensions are indicated: a total length of 1.0, a section length of .220, a section length of .26, and a tip diameter of .05. A detail view of the tip shows a diameter of .017.



1	Anode
2	Cathode
3	Case

C++ Application Program: system.cpp

```

#include <dos.h>
#include <conio.h>
#include <bios.h>
#include <stdlib.h>
#include <string.h>
#include <math.h>

#define BASE 0x300
#define CSR BASE //control register
#define ASR BASE+2 //A/D setup register R/W
#define DTR BASE+4 //data transfer register R/W
#define TLR BASE+6 //triger count(0~15) R/W
#define TMR BASE+8 //triger count(16~23) R/W
#define GR1 BASE+10 //gain register1(1~8) R/W
#define GR2 BASE+12 //gain register2(9~16) R/W
#define DIOR BASE+14 //digital I/O register R/W
#define ADR BASE+16 //data register RO

#define LCDCTRL 0x260+3 // LCD control register
#define LPTDATA 0x260+2 // data register

#define INTR 0x1C /* The clock tick interrupt */

#ifdef __cplusplus
#define __CPPARGS ...
#else
#define __CPPARGS
#endif

void initad(void);
void initlcd(void);
void writelcd(unsigned char);
void writectl(unsigned char);
void gotolcd(void);
void putslcd(char *);
void clearlcd(void);
void interrupt (*oldhandler)(__CPPARGS);

unsigned char x,y;
unsigned int csr,asr,dtr,tlr,tmr,gr1,gr2,dior,adr;
float
ch[8],chref[8],c[8],chreff[8],initvals[8],delVx1,delVx2,delVy1,delVy2,delVz1,del
Vz2;
float Xden,Yden,Zden;
float Xfield,Yfield,Zfield,xt,yt,zt;
float Xoffset,Yoffset,Zoffset;
unsigned int count,flag,i,samplerate,firstval=0;
float ref2=3.91,ref3=.73,ref4=8.86,ref5=13.37,ref6=6.82,ref7=2.80;
float x0=0.0014,x1=0.1324,x2=-.4066,x3=8.3211,x4=1.4574;
float y0=.0157,y1=.1242,y2=-1.0474,y3=7.7864,y4=.4413;
float z0=-.0606,z1=.3748,z2=-.6920,z3=1.6046,z4=.0551;

char *string;

void interrupt handler(__CPPARGS)
{

```

```

        disable();

/* increase the global counter */
        count++;
// sampling=count%2; // 18 Hz clock
// sampling=count%36; // 9 Hz sampling rate
// count=count%36; // 0.5 Hz sampling rate
// samplerate=count%18; // 0.5 Hz display refresh rate
// flag=0;
if (samplerate==0)
{
    for(i=0;i<8;i++)
    {
        outpw(CSR,0x1);
        outpw(CSR,0x3);

        do{csr=inp(CSR);}
        while(~csr&(1<<7)); // wait for data ready

        c[i]=c[i]+(inp(ADR)>>4);
    }
}

if(count==0)
{
    /*
        for (i=0;i<8;i++) ch[i]=c[i]*10/0xffe/18; */
        for (i=0;i<8;i++) ch[i]=c[i]*10/0xfff/2;
        for (i=1;i<8;i++) chref[i]=ch[i];
        for (i=1;i<8;i++) ch[i]=ch[i]/ch[0];
        for (i=0;i<8;i++) c[i]=0;

        if (firstval==0)
        {
            for (i=1;i<8;i++) initvals[i]=ch[i];
            firstval=1;
            Xoffset=sqrt(pow((ref2-chref[2]),2)+pow((ref3-chref[3]),2));
            Yoffset=sqrt(pow((ref4-chref[4]),2)+pow((ref5-chref[5]),2));
            Zoffset=sqrt(pow((ref6-chref[6]),2)+pow((ref7-chref[7]),2));

            if (ch[2] < initvals[2])
            {
                Xoffset=-Xoffset;
            }
            if (ch[4] < initvals[4])
            {
                Yoffset=-Yoffset;
            }
            if (ch[7] < initvals[7])
            {
                Zoffset=-Zoffset;
            }
        }

        delVx1= ch[2]-initvals[2];
        delVx2= ch[3]-initvals[3];

```

```

        Xden=sqrt(delVx1*delVx1+delVx2*delVx2);

        if (ch[2] < initvals[2])
        {
            Xden=-Xden;
        }

        delVy1= ch[4]-initvals[4];
        delVy2= ch[5]-initvals[5];
        Yden= sqrt(delVy1*delVy1+delVy2*delVy2);

        if (ch[4] < initvals[4])
        {
            Yden=-Yden;
        }

        delVz1= ch[6]-initvals[6];
        delVz2= ch[7]-initvals[7];
        Zden=sqrt(delVz1*delVz1+delVz2*delVz2);

        if (ch[7] < initvals[7])
        {
            Zden=-Zden;
        }

        xt=Xden-Xoffset;
        yt=Yden-Yoffset;
        zt=Zden-Zoffset;

        Xfield=x0*pow(xt,4)+x1*pow(xt,3)+x2*pow(xt,2)+x3*xt+x4;
        Yfield=y0*pow(yt,4)+y1*pow(yt,3)+y2*pow(yt,2)+y3*yt+y4;
        Zfield=z0*pow(zt,4)+z1*pow(zt,3)+z2*pow(zt,2)+z3*zt+z4;
        Xfield=1000*Xfield;
        Yfield=1000*Yfield;
        if (Yfield < 0)
        {
            Yfield=.409*Yfield;
        }
        Zfield=10000*Zfield;

        //      r=sqrt(Xden*Xden+Yden*Yden+Zden*Zden);
        flag=1;

    }

    /* reenale interrupts at the end of the handler */
    enable();
    /* call the old routine */
    oldhandler();
}

void clearlcd(void)
{
    writectl(0x1);
    delay(5);
}

```

```

void initlcd(void)
{
    delay(500);

    //    outportb(LPTMODE,DIROUT); //set write to LCD

    writectrl(0x38);
    delay(7);
    writectrl(0x38);
    delay(1);
    writectrl(0x38);
    writectrl(0x38);
    writectrl(0x0c);
    writectrl(0x6);
    writectrl(0x1);
    delay(5);
}

void putslcd(char *str)
{
    int len;
    len=strlen(str);
    for(int i=0;i<len;i++)
    {
        writelcd(str[i]);
        x++;
    }
}

void gotolcd(void)
{
    unsigned char pos;
    if((x<1||x>20)|| (y<1||y>4)){x=1;y=1;}
    if(y==1){pos=x-1;}
    if(y==2){pos=(1<<6)+x-1;}
    if(y==3){pos=x+0x13;}
    if(y==4){pos=(1<<6)+x+0x13;}

    outportb(LPTDATA,pos|0x80);
    outportb(LCDCTRL,0x00);
    outportb(LCDCTRL,0x01);
    for(int i=0;i<10;i++);
    outportb(LCDCTRL,0x00);
    for(i=0;i<100;i++);
}

void writectrl(unsigned char c)
{
    outportb(LCDCTRL,0x00);
    outportb(LPTDATA,c);
    outportb(LCDCTRL,0x01);
    for(int i=0;i<10;i++);
    outportb(LCDCTRL,0x00);
    for(i=0;i<200;i++);
}

void writelcd(unsigned char ch)

```

```

    {
        gotolcd();
        outportb(LCDCTRL, 0x10);
        outportb(LPTDATA, ch);
        outportb(LCDCTRL, 0x11);
        for(int i=0; i<10; i++);
        outportb(LCDCTRL, 0x10);
        for(i=0; i<100; i++);
    }

void initad(void)
{
    outpw(CSR, 1<<6);
    delay(10);
    outpw(CSR, 0);          // reset board

    outpw(GR1, 0);
    outpw(GR2, 0);          // set gain

    outpw(TLR, 0xff9c);
    outpw(TMR, 0xff);

    outpw(DTR, 0);
    outpw(ASR, 0x70);
    delay(1);
}

//main function

int main(void)
{
    count=0;
    initad();
    initlcd();

    /* save the old interrupt vector */
    oldhandler = getvect(INTR);

    /* install the new interrupt handler */
    setvect(INTR, handler);

    for(;;)
        // for (int k=0; k<300; k++)
        {
            do{}while(flag==0);          //wait for flag to be set

            clearlcd();

            x=1; y=1;
            gotolcd();
            putslcd("X: ");
            gcvt(Xfield, 6, string);
            putslcd(string);

            x=1; y=2;
            gotolcd();
            putslcd("Y: ");

```

```

        gcvf(Yfield,6,string);
        putsld(string);

        x=1;y=3;
        gotoLCD();
        putsld("Z: ");
        gcvf(Zfield,6,string);
        putsld(string);
        flag=0;
    }

/* reset the old interrupt handler */
    setvect(INTR, oldhandler);

    return 0;
}

```